PCCP

ROYAL SOCIETY OF CHEMISTRY

REVIEW

Published on 07 September 2026
Licensed under CC-BY 4.0

Check for updates

Cite this: *Phys. Chem. Chem. Phys.*, 2026, **28**, 21808

Interfacial thermal transport spectroscopy: a review of theory and experiment

Yixin Xu,[a] Xing Xiang,[a] Wenxiang Liu,[a] Yue Zhu,[bc] Yinglong Hu,[bc] Man Li,[bc] Hao Ma,[bc] Bing-Yang Cao*[d] and Yanguang Zhou*[a]

Received 9th July 2026,
Accepted 25th August 2026

DOI: 10.1039/d6cp02619b

rsc.li/pccp

Thermal transport across interfaces is a critical bottleneck in the thermal management of modern microelectronics, particularly as devices scale toward the nanoscale with increasingly high-power densities. While bulk material properties are well understood, the physics governing heat transfer at interfaces, defined by carrier transmission and scattering, remains a complex challenge. Here, we review methods and studies on interfacial thermal transport spectroscopy, bridging fundamental theory with the state-of-the-art modelling and experiments. We first examine the fundamentals of the phonon gas model and carrier coupling, followed by a detailed discussion of computational approaches ranging from atomistic Green's functions (AGF) and molecular dynamics (MD) simulations at the nanoscale to the Boltzmann transport equation (BTE) at the microscale. Then, we evaluate popular experimental techniques, such as frequency-domain thermoreflectance (FDTR), time-domain thermoreflectance (TDTR) and electron energy loss spectroscopy (EELS), emphasizing their role in resolving spectral phonon contributions. We further highlight emerging data-driven methods and machine learning approaches that accelerate physical understanding and materials discovery. Finally, we outline open challenges in characterizing spectral interfacial thermal transport within computational and experimental frameworks, as well as the persistent gaps between them. This review aims to provide a unified perspective on understanding and optimizing interfacial heat dissipation for next-generation electronic and energy devices.

I. Introduction

The pursuit of miniaturization and performance enhancement in modern electronics has driven the industry into a thermal crisis.[1–3] As described by Moore's law,[4] the density of transistors on integrated circuits has doubled approximately every two years, leading to exponential increases in computational power. However, thermal management technologies have not scaled at the same rate. This disparity has made heat dissipation the governing limit for device performance, directly impacting the reliability and efficiency of future systems.[5] For example, in high-performance logic devices and power electronics, the heat flux generated in localized "hotspots" can now exceed 1 kW cm^{-2}, largely degrading performance and reliability.[6,7] Beyond logic and memory devices, thermal transport properties are equally critical in energy conversion and storage systems, such as batteries and thermoelectrics. For instance, efficient heat dissipation is required to maintain uniform temperature distributions in battery packs,[8,9] preventing localized degradation and ensuring safe operation. It is noted that traditional cooling solutions such as heat sinks and fans are becoming insufficient because they address heat removal at the macroscale, whereas the effective thermal resistance is usually dominated by nanoscale structures.[10–12] This is because the continuum laws of Fourier heat conduction break down[13,14] when device dimensions shrink to the mean free path of heat carriers (*i.e.*, phonons and electrons). In nanostructures with multilayered materials, the total thermal resistance is no longer dominated solely by bulk materials, but is increasingly governed by the thermal boundary resistance (TBR).[15–17]

Whether in a transistor gate stack,[18] a heterogeneous 3D-IC package,[19] or a composite thermal interface material (TIM),[20] heat must traverse multiple junctions between dissimilar

[a] *Department of Mechanical and Aerospace Engineering, The Hong Kong University of Science and Technology, Clear Water Bay, Kowloon, Hong Kong SAR. E-mail: maeygzhou@ust.hk*
[b] *Department of Thermal Science and Energy Engineering, School of Engineering Science, University of Science and Technology of China, Hefei, Anhui 230027, China*
[c] *Institute of Micro-nano Thermal Energy Transport and Conversion, School of Engineering Science, University of Science and Technology of China, Hefei, Anhui 230027, China*
[d] *Key Laboratory of Thermal Science and Power Engineering of Ministry of Education, Department of Engineering Mechanics, Tsinghua University, Beijing 100084, China. E-mail: caoby@mail.tsinghua.edu.cn*

This journal is © the Owner Societies 2026

materials across length scales ranging from the nanoscale to the macroscale. At these boundaries, mismatches in energy spectra such as the vibrational density of states (VDOS) induce significant carrier scattering and reflection.[21] Consequently, understanding and manipulating thermal energy transport across these interfaces is essential for unlocking the next generation of thermal management technologies.

For bulk materials, the thermal conductivity κ has provided a useful macroscopic metric. In semiconductors and dielectrics, heat conduction is carried by a broad spectrum of phonon modes, each characterized by a distinct frequency, mean free path, and group velocity. The contribution of these modes to the total κ is governed by their spectral nature, where the transport of a single phonon results from multiple scattering mechanisms, including boundary scattering and anharmonic phonon–phonon interactions. This spectral nature becomes even more critical when analyzing interfacial thermal transport. The mismatch in the VDOS between two materials acts as a frequency-dependent filter, selectively allowing certain phonon modes to propagate while reflecting others. For instance, high-frequency phonons are usually seen as diffusely scattered due to surface roughness or atomic mixing,[22] whereas low-frequency phonons may transmit quasi-ballistically.[21,23] Therefore, to engineer interfaces with ultra-low or ultra-high conductance, a ''spectroscopic'' perspective is needed. Precisely understanding which phonon modes contribute most to the thermal transport, and which are bottlenecked at the interface, is the prerequisite for rational material design, enabling the tailoring of phonon spectra to match specific thermal management needs.

In this review, we provide a comprehensive examination of thermal transport across material interfaces, bridging the gap between fundamental physics and practical applications. We note that several excellent reviews have summarized interfacial thermal transport from different perspectives, including the historical development of Kapitza resistance[17] and thermal boundary resistance,[16,21] theoretical and computational methods[24–27] and nanoscale thermal-transport experiments and metrology.[28–33] These reviews provide valuable foundations for understanding interfacial heat transfer. Distinct from these previous works, the present review focuses on interfacial thermal transport spectroscopy. Rather than treating interfacial thermal conductance only as an integrated scalar quantity, we emphasize how spectral information, including phonon frequency, phonon mode, mean free path, and spatial localization, can be resolved by modern computational and experimental approaches. The following discussion is organized into four primary sections: (i) the fundamentals of interfacial thermal transport, (ii) the existing computational modeling techniques, (iii) experimental spectroscopy methods, and (iv) emerging data-driven approaches in interfacial transport. Following this technical overview, we offer a forward-looking perspective on interfacial thermal transport from both simulation and experimental standpoints, as well as their synergistic integration.

II. Fundamentals of interfacial thermal transport

Heat transfer across interfaces has attracted the attention of scientists for centuries since the initial observation of intrinsic resistance of heat transfer from a solid body to the surrounding gas through the two-phase interface.[34] The interfacial heat transfer was then extended by Poisson in 1835,[35] in which the heat flux across the interface can be defined as

$$J = h\Delta T \tag{1}$$

where the heat flux J is defined as the energy transport per unit time across the interface per unit area. In eqn (1), ΔT denotes the temperature drop across the interface[15] and h is the phenomenological transport coefficient (*i.e.*, TBC). Correspondingly, the thermal boundary resistance (TBR) is defined as the inverse of TBC. Later in 1941, the thermal resistance at the interface was demonstrated by Kapitza through experimental observations, *i.e.*, a temperature drop at the interface of solid and liquid helium.[15] Since then, the thermal resistance is also termed the Kapitza resistance, which has been extended and broadened both experimentally and theoretically in the following decades. However, it is noted that the TBR becomes loosely defined when applied to a macroscale system, in which the temperature drop may not appear as sharp or abrupt as expected. Instead, there is a phenomenological length we can define for quantifying the temperature discontinuity. In this circumstance, the TBR at ideal interfaces with no thickness (*e.g.*, atomically sharp and abrupt temperature drop) becomes the TBR of the interfacial regions (*e.g.*, several atomic layers in the near interface region with a temperature gradient).

Considering phonons as the primary heat carriers, we first revisit the fundamentals of heat transfer across ideal interfaces to establish a clear understanding of the underlying physical mechanisms. When phonons encounter an interface, the incident and reflected modes on both sides contribute to the net heat flux.[16] As described in eqn (2), this heat flux is defined as contributions from each phonon modal energy, integrated over the entire frequency spectrum and accounting for the transmission probability across the interface[16]

$$J = \frac{1}{V}\sum_{\lambda} \hbar\omega_\lambda v_\lambda^{\perp} \zeta_\lambda^{\mathrm{A}\to\mathrm{B}} \left[\bar{f}(\omega_\lambda, T_\mathrm{A}) - \bar{f}(\omega_\lambda, T_\mathrm{B})\right] \tag{2}$$

where V is the volume, $\hbar$ is the reduced Planck constant, ω_λ is the phonon frequency specified by the phonon mode λ of two interfacial sides, $v_\lambda^{\perp}$ is the phonon group velocity normal to the interface, $\zeta_\lambda^{\mathrm{A}\to\mathrm{B}}$ is the phonon transmission coefficient, and $\bar{f}$ is the phonon distribution function on two sides A and B. The distribution function is usually treated as an equilibrium Bose–Einstein distribution $f(\omega,T) = (e^{\hbar\omega/k_\mathrm{B}T} - 1)^{-1}$ where k_B is the Boltzmann constant. Based on eqn (1) and (2), we can then express the interfacial thermal conductance (ITC) G as

$$G(T) = \frac{1}{V}\sum_{\lambda} \hbar\omega_\lambda v_\lambda^{\perp} \zeta_\lambda^{\mathrm{A}\to\mathrm{B}} \frac{\partial \bar{f}(\omega_\lambda, T)}{\partial T} \tag{3}$$

Therefore, the determination of the phonon transmission coefficient is central to solving the problem of interfacial thermal transport.

A. Acoustic mismatch model and diffuse mismatch model

There are two primary empirical models used to approximate the phonon transmission coefficient, *i.e.*, the acoustic mismatch model (AMM)[36] and the diffuse mismatch model (DMM).[21] The AMM treats phonons as waves traveling through a continuous medium and ignores inelastic scatterings. It assumes a perfect and geometrically smooth interface where phonons undergo specular reflection (mirror-like) or refraction following Snell's law. In the AMM, each material can be described by an acoustic impedance $Z = \rho c$, where ρ is mass density and c is sound velocity.[36] The angles of incident and transmitted phonons should follow $\sin\theta_A/c_A = \sin\theta_B/c_B$ where θ_A and θ_B denote the incident angle and refracted angle on each side, respectively. The corresponding phonon transmission is then given by

$$\zeta_{\mathrm{AMM}}^{\mathrm{A}\to\mathrm{B}} = \frac{4Z_{\mathrm{A}}Z_{\mathrm{B}}\cos\theta_{\mathrm{A}}\cos\theta_{\mathrm{B}}}{\left(Z_{\mathrm{A}}\cos\theta_{\mathrm{B}} + Z_{\mathrm{B}}\cos\theta_{\mathrm{A}}\right)^2} \tag{4}$$

By incorporating the Debye model for isotropic solids (*i.e.*, $\omega = ck$) and accounting for distinct longitudinal and transverse sound velocities, the ITC estimated by AMM is then given by

$$G_{\mathrm{AMM}} = \frac{1}{4\pi^2}\sum_{\lambda} I_{\lambda}\int_0^{\omega_{\mathrm{D}}} \frac{\hbar\omega_{\lambda}^3}{c_{\lambda}}\frac{\partial\bar{f}(\omega_{\lambda},T)}{\partial T}\mathrm{d}\omega \tag{5}$$

where I_λ is the accumulation of all the incident phonon modes satisfying the Snell's law, and is calculated as

$$I_{\lambda} = \int_0^{\pi/2} \zeta_{\mathrm{AMM}}^{\mathrm{A}\to\mathrm{B}}(\theta_{\mathrm{A}},\lambda)\cos\theta_{\mathrm{A}}\sin\theta_{\mathrm{A}}\mathrm{d}\theta_{\mathrm{A}} \tag{6}$$

AMM generally predicts the lower boundary of ITR (or the upper bound of ITC) for long-wavelength phonons, and therefore it can usually explain the thermal transport at very low temperatures, a regime where low-frequency and long-wavelength phonons dominate the total transmission function. Nevertheless, AMM overestimates thermal transport mainly because the ignored phonon scatterings at the interface.[37,38]

The need to account for the interfacial scattering and the contribution of high-frequency phonons necessitated the formulation of the DMM.[21] In contrast, DMM assumes that the interface is rough and disordered. When a phonon hits the interface, it ''forgets'' where it came from and scatters diffusely (randomly) into either material. The probability of a phonon transmitting to side B or reflecting to side A depends only on the phonon density of states (PDOS) of each side, no longer on the incident angle anymore, given by

$$\zeta_{\mathrm{DMM}}^{\mathrm{A}\to\mathrm{B}}(\omega) = \frac{\sum_{\lambda}\left[k_{\lambda,\mathrm{B}}(\omega)\right]^2}{\sum_{\lambda}\left[k_{\lambda,\mathrm{B}}(\omega)\right]^2 + \sum_{\lambda}\left[k_{\lambda,\mathrm{A}}(\omega)\right]^2} \tag{7}$$

in which k is the wave vector. Eqn (7) considers the exact phonon dispersion including the transmission contribution from both acoustic and optical phonon modes. The ITC then becomes[39]

$$G^{\mathrm{DMM}} = \frac{1}{8\pi^2}\sum_{\lambda}\int_{k_{\lambda,\mathrm{A}}>0}\hbar\omega_{\lambda,\mathrm{A}}\left(k_{\lambda,1}\right)k_{\lambda,\mathrm{A}}{}^2\zeta_{\mathrm{DMM}}^{\mathrm{A}\to\mathrm{B}}\left|v_{\lambda,\mathrm{A}}^{\perp}\left(k_{\lambda,\mathrm{A}}\right)\right|\frac{\partial f}{\partial T}\mathrm{d}k_{\lambda,\mathrm{A}} \tag{8}$$

where $v_{\lambda,\mathrm{A}}^{\perp}(k_{\lambda,\mathrm{A}})$ is the group velocity normal to the interface, and f is the equilibrium vibration distribution, *i.e.*, Bose–Einstein distribution.

The DMM is further extended to include inelastic scatterings to approximate the ITC.[40–42] However, we note that the wave nature of low-frequency phonons is ignored in DMM, which may lead to an underestimation of the transmission of low-frequency phonons.[43] Later on, a mixed mismatch model (MMM), incorporating the DMM- and AMM-based transmission through a specular parameter p, is proposed to estimate interfacial phonon transmission.[24,44] The specular parameter p depends on both the interfacial roughness η and the wavelength of phonons λ.[24,44] Meanwhile, the conventional AMM and DMM apply bulk phonon properties to calculate phonon transmission and ignore real interfacial physical properties, such as interfacial adhesion,[45–47] interfacial modes,[48–51] inelastic scatterings,[52–54] and nanostructures.[55–61] Even though these models ignore specific interfacial details, they demonstrate a strong and clear physical picture of interfacial phonon transmission. In the following, we will review recent progress in characterizing interfacial thermal transport, covering advances in both computational modeling (Section III) and experimental methodologies (Section IV) (Fig. 1).

III. Computational modeling

A. Atomic Green's function

The atomistic Green's function (AGF)[62–66] is derived based on the phonon–gas model (PGM)[67–70] and solves the phonon transport properties in the reciprocal space. In the harmonic AGF, we assume that there are no phonon–phonon interactions and the center of harmonic AGF becomes the calculation of the harmonic dynamic matrix, which is derived from the local potential energy surface when atoms are at their equilibrium positions.[66,71] To solve this problem efficiently, the harmonic matrix of the entire system is usually decomposed into five parts, including two semi-infinite leads, the interface region, and corresponding interactions between the leads and the interfaces.[66,71] Then, the phenomenological phonon energy transmission function Γ_{AGF} can be calculated by coupling the Green's function of these isolated parts. We note that Γ_{AGF} inherently includes both the transmission coefficient of each single phonon (*e.g.*, $\zeta_{\lambda}^{\mathrm{A}\to\mathrm{B}}$ in eqn (2)) and the phonon number flux (group velocities $v_{\lambda}^{\perp}$ times the PDOS),[62,63] rendering the ITC in the Landauer form[72]

$$G_{\mathrm{AGF}} = \frac{1}{2\pi S}\int_0^{\infty}\hbar\omega\frac{\partial f(\omega,T)}{\partial T}\Gamma_{\mathrm{AGF}}(\omega,T)\mathrm{d}\omega \tag{9}$$

This journal is © the Owner Societies 2026

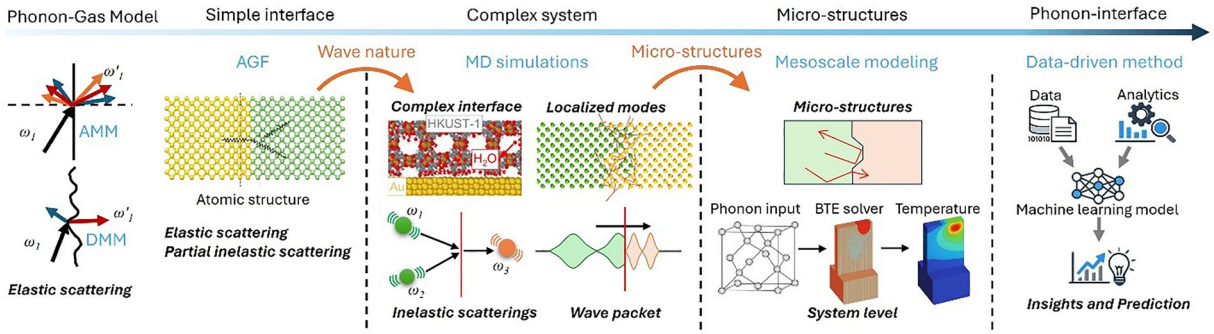


Fig. 1 Computational modeling methods of phonon-dominated thermal energy transport across interfaces. The AGF schematic is from Guo *et al.*[89] Copyright@2021 American Physical Society. The schematics of complex interface simulations are from Wang *et al.*[92] Copyright@2024 Springer Nature. Localized modes are from Cheng *et al.*[48] Copyright@2021 Springer Nature. The schematic of mesoscale modeling for BTE solver is from Hu *et al.*[211] Copyright@2024 Elsevier.

in which S is the cross-sectional area of the interface. With eqn (9), the AGF has been used to study the thermal transport across various interfaces, *e.g.*, Si/Ge,[23,73] h-BN/graphene,[74–76] $Si/CoSi_2$[77] and carbon nanotube (CNT) junctions.[78] By accurately calculating the interfacial force constant matrix, it is feasible to consider the effect of atomistic structures on interfacial thermal transport, such as roughness,[55,79] grain boundaries[55,80,81] and disordered layers.[82–84] This makes AGF an effective tool for designing interfacial structures with targeted interfacial thermal transport properties. For instance, Yang *et al.*[82–84] showed phonons above ~3 THz were reflected at a-Si/c-Si interfaces, which is consistent with experiments,[43] and that mass distribution at Si/Ge interfaces enhanced sub-4 THz transmission but hindered 5–8 THz phonons as shown in Fig. 2(a) and (b). Ju *et al.*[85] used AGF with Bayesian optimization to identify optimal interfacial structures at Si/Si and Si/Ge interfaces, showing high-frequency phonons (>3 THz) were most sensitive to structure. Ju and Liang[86] also found that phonon interference in Si/Ge nanocomposites could enhance the ITC by up to 19.1%.

However, these early AGF studies only considered elastic scattering and ignored inelastic phonon scatterings.[55,73–76,78–84] Most recently, the anharmonic phonon scatterings, *i.e.*, three-phonon scatterings, have been incorporated into the AGF framework by including anharmonic phonon–phonon self-energies in the non-equilibrium Green's function (NEGF).[87–89] The anharmonic self-energies can be derived from third-order or even higher-order interatomic force constants and incorporated into the Green's function of the device region. Using these NEGF calculations, Dai and Tian[87] found that anharmonicity facilitated the energy exchange among phonons and assisted those blocked phonons in the harmonic limit to propagate across the interface *via* inelastic scatterings, *e.g.*, these phonons with frequencies above 10 THz contributed to the interfacial heat current across the Si/Ge interface. Guo *et al.*[88,89] also reported that these high-frequency phonons ($\omega \geq \omega_{\text{cutoff}}$) at the Si/Ge interface can contribute to ITC at elevated temperatures [Fig. 2(c)]. By including the inelastic scatterings, they demonstrated that the ITC enhancement was about 10% at room temperature and reached about 20% at 600 K [Fig. 2(d)]. Nevertheless, considering higher-order anharmonicity in AGF, such as four-phonon scattering,[90,91] remains extremely difficult due to the high computational cost. Besides, it becomes challenging to quantify the phonon transport properties of complex systems, *e.g.*, metal–organic frameworks (MOF),[92–99] superionic crystals,[100–104] hybrid crystals[105–111] and heterostructures,[83,112–115] using the AGF method due to the unacceptable computational cost and memory requirement.

B. Molecular dynamics simulations

Meanwhile, molecular dynamics (MD) simulations directly trace atomic trajectories in real space, and have been used to quantify interfacial thermal transport.[116,117] Over the past decade, many methods have been proposed to characterize the spectrally-decomposed energy transmission across interfaces within the framework of MD simulations.[25] These include time domain normal mode analysis (TDNMA),[118,119] Green–Kubo modal analysis (GKMA),[120,121] time domain direct decomposed method (TDDDM),[122] frequency domain direct decomposed method (FDDDM)[123,124] and spectral heat current (SHC) method.[54,125] Furthermore, multi-carrier effects, such as the electron–phonon (EP) coupling, may be incorporated by introducing the multi-temperature model into MD simulations.[126–129]

There are two main ways to quantify interfacial thermal transport in MD simulations, including equilibrium MD (EMD) and nonequilibrium MD (NEMD). The EMD simulations utilize the system heat current fluctuations as the input to calculate transport coefficients based on the Green–Kubo formula,[130] and the ITC is given by

$$G_{\text{EMD}} = \frac{S}{k_{\text{B}}T^2}\int \langle Q_{\text{S}}(t)\cdot Q_{\text{S}}(0)\rangle \mathrm{d}t \tag{10}$$

in which k_{B} is the Boltzmann constant, T is the temperature, Q_{S} is the heat flux fluctuation across a cross-section with an area of S, and $\langle\,\rangle$ denotes the time autocorrelation. It is noted that one should perform a long enough time integral to obtain converged thermal transport properties. By integrating the phonon normal mode decomposition into the heat flux Q_{S},

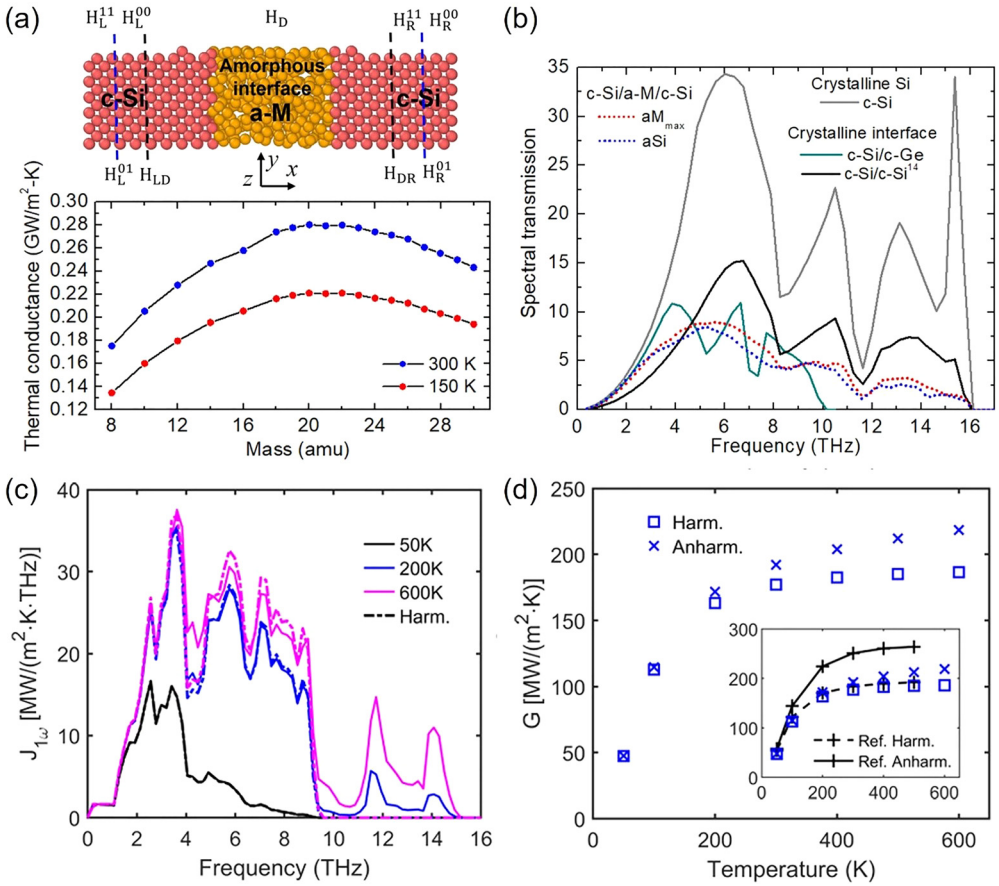


Fig. 2 Phonon transmission calculated using harmonic AGF: (a) thermal conductance at Si/amorphous Si interface with atomic mass in the amorphous interface changing from 8 to 30 amu, (b) the corresponding phonon spectral transmission for the amorphous interface in the Si/amorphous Si interface and that for Si/Ge interface. Phonon transmission calculated using anharmonic AGF: (c) spectral thermal conductance of Si/Ge interface considering the anharmonic phonon scatterings, where the solid lines and dash-dot lines denote the anharmonic and harmonic results, respectively. (d) Comparison between harmonic AGF and anharmonic AGF results for Si/Ge interface. Panels (a) and (b) are from Yang *et al.*[82] Copyright@2023 American Physical Society. Panels (c) and (d) are from Guo *et al.*[89] Copyright@2021 American Physical Society.

i.e., the Green–Kubo modal analysis (GKMA),[49,120,131–133] one can further calculate the modal ITC through auto- or cross-correlation of mode heat flux in the EMD simulations. EMD simulations inherently assume that the system is periodic, which are typically employed to determine the apparent thermal conductivity of bulk materials. Therefore, the ITC calculated based on EMD simulations includes the contribution from the two contacting bulk parts rather than the pure interfacial region. Meanwhile, resolving modal thermal transport using GKMA is particularly computationally demanding. This is because GKMA requires the phonon eigenvectors of the entire system as input, and the computational complexity of calculating the modal heat flux cross-correlation function increases significantly.[49,120,131–133]

In contrast, NEMD simulations provide a more efficient method to determine the interfacial phonon transmission. In NEMD simulations, an explicit heat flow is artificially generated under an imposed temperature gradient, allowing transport coefficients to be calculated *via* Fourier's law[34]

$$G_{\mathrm{NEMD}} = \frac{1}{S}\frac{Q_{\mathrm{NEMD}}}{\Delta T} \tag{11}$$

where Q_{NEMD} is the heat current across a cross-section with area of S and ΔT is the temperature difference at the interface.

Analyzing phonons in NEMD primarily involves calculating their contribution to Q_{NEMD} or ΔT, as shown in eqn (11). The modal heat current across an imaginary or real interface can be computed in the framework of NEMD simulations,[49,120,131,132,134–138] *i.e.*, the time domain direct decomposition method (TDDDM),[122]

$$Q_{\mathrm{S}}^{\mathrm{TDDDM}}(\lambda) = \sum_{i\in\mathrm{Left}}^{N_{\mathrm{Left}}}\sum_{j\in\mathrm{Right}}^{N_{\mathrm{Right}}}\left\langle \frac{\partial U_j(t)}{\partial \vec{r}_i(t)}\vec{v}_i(\lambda,t) - \frac{\partial U_i(t)}{\partial \vec{r}_j(t)}\vec{v}_j(\lambda,t)\right\rangle \tag{12}$$

in which $\vec{v}_i(\lambda,t)$ denotes the velocity of atom i under vibrational mode λ.[139] By assuming the same temperature gradient for all phonon modes, the modal interfacial thermal conductance is then given by

$$G_{\mathrm{TDDDM}}(\lambda) = \frac{1}{S}\frac{Q_{\mathrm{S}}^{\mathrm{TDDDM}}(\lambda)}{\Delta T} \tag{13}$$

 This journal is © the Owner Societies 2026

where S and ΔT are the cross-section area and interfacial temperature difference, respectively. Furthermore, the temperature difference can be decomposed into contributions at the modal level. For instance, Feng *et al.*[135,137] observed a nonequilibrium temperature distribution between acoustic and optical phonons near the two interfacial sides. This disparity results in distinct contributions from each mode to the overall temperature difference across the interface and the corresponding modal ITC.

At the same time, the spectral heat current (SHC) across an imaginary or real interface in NEMD simulations is given by[54,123–125,140]

$$Q_{\mathrm{S}}^{\mathrm{SHC}}(\omega)=2\sum_{i\in\mathrm{left}}\sum_{j\in\mathrm{right}}\mathrm{Re}\left[\int_{-\infty}^{+\infty}\left(\frac{\partial U_j}{\partial\vec{r}_i}\bigg|_{\tau}\vec{v}_i(0)-\frac{\partial U_i}{\partial\vec{r}_j}\bigg|_{\tau}\vec{v}_j(0)\right)\mathrm{e}^{-i\omega\tau}\mathrm{d}\tau\right] \tag{14}$$

and the spectral heat current across a control volume in NEMD simulations can be written in the form of (*i.e.*, frequency domain direct decomposition method, FDDDM[123])

$$Q_{\mathrm{V}}^{\mathrm{FDDDM}}(\omega)=\sum_{n}\sum_{s_1}\sum_{s_1<s_2}\cdots\sum_{s_{n-1}<s_n}\times\left[\sum_{\alpha=1}^{n-1}\sum_{\beta=\alpha+1}^{n}\frac{1}{n}\int_0^{+\infty}C_{ij}(\tau)\mathrm{e}^{i\omega\tau}\mathrm{d}\tau\cdot\left(r_{s_\alpha}^0-r_{s_\beta}^0\right)\right] \tag{15}$$

By assuming the same temperature gradient or temperature drop for all phonons, we also obtain the spectral ITC across a real interface

$$G_{\mathrm{NEMD}}(\omega)=\frac{1}{S}\frac{Q_{\mathrm{S}}^{\mathrm{SHC}}(\omega)}{\Delta T} \tag{16}$$

A detailed derivation of the modal and spectral decomposed ITC including eqn (12)–(16) can be found in our previous review.[25]

It is noted that TDDDM, FDDDM, and SHC methods are within the framework of NEMD simulations and therefore include the size effect in the calculated results.[122,123,141,142] The size effects should be tested in TDDDM, FDDDM, and SHC calculations to obtain converged results. Meanwhile, FDDDM and SHC can only calculate the frequency-dependent thermal transport properties and therefore the frequency-dependent ITC. TDDDM can compute mode-level thermal transport properties. However, the required input of vibrational eigenvectors in TDDDM strongly limits its application in complex systems with large unit cells.[122] It is worth noting that the calculated spectral thermal transport properties in NEMD simulations also depend on the choice of thermostats.[143] Li *et al.*[143] showed that the local temperature was controlled better using the Langevin thermostat compared to that with the Nosé–Hoover thermostat. Hu *et al.*[144] found that the Langevin thermostat behaved like a thermalizing boundary for phonons and provided mode-level thermal-equilibrium phonon outlets. However, the Nosé–Hoover chain thermostat and velocity rescaling method behaved like biased reservoirs and would provide spatially uniform heat generation and mode-level nonequilibrium phonon outlets. Therefore, the thermostat used to generate the heat flux in NEMD simulations should be chosen carefully.[142,145]

Recently, Fan *et al.*[146] extended the spectral heat current to the framework of homogeneous nonequilibrium molecular dynamics (HNEMD), in which the heat current time correlation function is defined as

$$\vec{K}(\tau)=\sum_i\sum_{j\neq i}\vec{r}_{ij}(0)\left\langle\frac{\partial U_j}{\partial\vec{r}_{ij}}\bigg|_0\cdot\vec{v}_i(\tau)\right\rangle_{\mathrm{ne}} \tag{17}$$

The spectral heat current in HNEMD simulations can then be expressed as

$$\vec{Q}_{\mathrm{HNEMD}}(\omega)=2\,\mathrm{Re}\left[\int_{-\infty}^{+\infty}\vec{K}(\tau)\mathrm{e}^{i\omega\tau}\mathrm{d}\tau\right] \tag{18}$$

Therefore, the spectral thermal conductivity along the interested direction in HNEMD simulations is

$$\vec{\kappa}_{\mathrm{HNEMD}}(\omega)=\frac{1}{VF_{\mathrm{e}}}\frac{\vec{Q}_{\mathrm{HNEMD}}(\omega)}{T} \tag{19}$$

where T is the temperature, V is the system volume and F_{e} is a vector that determines the driven force in HNEMD simulations.[146–148]

Once the frequency-dependent heat current is obtained, the phonon transmission function can be then estimated based on the Landauer theory.[149–151] In the Landauer theory, the heat current spectrum from the left lead to the right lead through a junction connecting two leads at two different equilibrium heat-bath temperatures (*i.e.*, T_{L} and T_{R}) is written in the form of

$$Q(\omega)=\hbar\omega[n_{\mathrm{L}}(\omega)-n_{\mathrm{R}}(\omega)]\Gamma(\omega) \tag{20}$$

where n is the equilibrium phonon distribution function at heat-bath temperatures and has the classical limit form of $n_{\mathrm{L\,or\,R}}(\omega)=k_{\mathrm{B}}T_{\mathrm{L\,or\,R}}/\hbar\omega$ in molecular dynamics simulations, in which $\Gamma(\omega)$ is the phonon transmission function. The spectral ITC $G(\omega)$ is then written as

$$\begin{aligned}G(\omega)&=\frac{\hbar\omega[n_{\mathrm{L}}(\omega)-n_{\mathrm{R}}(\omega)]\cdot\Gamma(\omega)}{S(T_{\mathrm{L}}-T_{\mathrm{R}})}\\&=\frac{\hbar\omega\Delta n(\omega)\cdot\Gamma(\omega)}{S\Delta T}\\&\approx\frac{\hbar\omega\partial n(\omega)\cdot\Gamma(\omega)}{S\partial T}\overset{\text{classical limit}}{\approx}\frac{k_{\mathrm{B}}\Gamma(\omega)}{S}\end{aligned} \tag{21}$$

It should be noted that eqn (21) is only valid when the temperature gradient is kept in the linear regime. The phonon transmission function in NEMD simulations can be calculated using

$$\Gamma(\omega)=\frac{Q(\omega)}{k_{\mathrm{B}}\Delta T} \tag{22}$$

However, MD follows the classical Boltzmann distribution[152] and inherently assumes all vibrations are occupied, which overestimates the calculated ITC at low temperatures

as shown in eqn (21). Quantum corrections combined with the SHC method[135,136,153] have been proposed to correct the ITC under physically realistic conditions. By incorporating the Bose–Einstein distribution into the Landauer formalism,[72,154] the quantum-corrected ITC can be calculated as

$$G_{\mathrm{QC}} = \frac{1}{2\pi S}\int_0^{+\infty} \hbar\omega \frac{\partial f_{\mathrm{Bose-Einstein}}(\omega, T)}{\partial T} \Gamma(\omega, T)\mathrm{d}\omega \qquad (23)$$

where S is the transverse area of the unit cell, $f_{\mathrm{Bose-Einstein}}(\omega,T)$ is the Bose–Einstein distribution, and $\Gamma(\omega,T)$ denotes the temperature-dependent spectral phonon transmission calculated *via* eqn (22).

It is worth noting that MD simulations inherently incorporate all orders of anharmonicity, and the spectral ITC [eqn (10)–(22)] computed within MD frameworks naturally includes all elastic and inelastic processes.[54,122,124,125,131,133,135] For instance, Sääskilahti *et al.*[54] separated elastic and first-order inelastic contributions at Ar/heavy-Ar interfaces [Fig. 3(a)–(c)], and they found the first-order inelastic scatterings can enhance phonon transmission across the entire frequency spectrum [Fig. 3(b)], thereby leading to an increase in ITC at elevated temperatures (*e.g.*, ∼40% at 30 K in [Fig. 3(c)]). This enhancement is further amplified when full-order inelastic scatterings are considered [Fig. 3(d) and (e)]. As reported by Xu *et al.*,[153] inelastic scatterings enhance phonon transmission across the full spectrum and contribute ∼80% to the corrected ITC [Fig. 3(f)]. Zhou and Hu[124] further resolved the full three-phonon scattering processes at the Ar/heavy Ar interface, and showed that third-order processes became significant above 30 K. They also identified that these emergent interfacial modes (∼12 THz) contributed ∼11% to the room-temperature ITC of Si/Ge interfaces, consistent with Gordiz and Henry[49] and experiments.[48] Feng *et al.*[135] also reported that interfacial modes boosted inelastic transport, contributing over 50% to ITC at room temperature, with optical modes contributing equally or more than acoustic modes, using modal heat current[122] and modal temperature.[137] These significant inelastic contributions to ITC are further reported in many other systems, such as Al/Si,[53,136,138,155] GaN/metal,[156] GaN/ZnO,[51] GaN/AlN,[157,158] and Au/graphene.[159] Recently, Xu and Zhou[160] suggested the significance of elastic and inelastic vibrational scatterings at the interfaces was determined by the competition between the similarity of vibrational density of states (VDOS) and the anharmonicity of the interface.[160] For contacts with similar VDOS such as SiC/Si interfaces,[161] they demonstrate a strong modal coupling across the interface leading to a high contribution to ITC (>80%) from the elastic scatterings. Instead, for these interfaces with dissimilar VDOS such as Ar/h-Ar and Si/Ge, the ratio of ITC contributed by inelastic vibrational scatterings can be quantitatively characterized by the interfacial anharmonic ratio (IAR).[160]

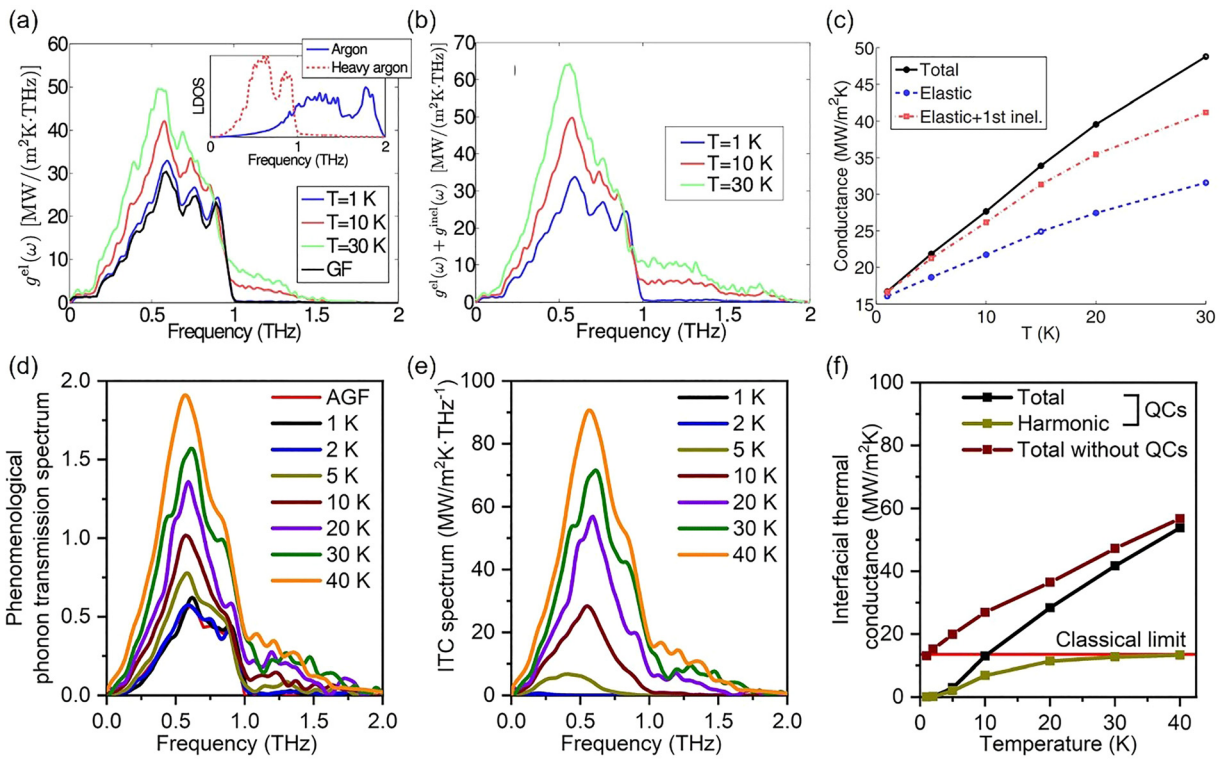


Fig. 3 Spectral phonon transmission across an Ar/heavy-Ar interface computed using SHC within NEMD simulations, illustrating the role of inelastic scatterings. Thermal conductance spectrum considering (a) elastic scatterings only and (b) first-order inelastic scatterings. (c) Corresponding thermal conductance as a function of temperature. (d) Phonon transmission considering full-order inelastic scatterings calculated using eqn (22) and (e) quantum-corrected thermal conductance spectrum by applying the Bose–Einstein distribution [eqn (23)]. (f) The total and harmonic thermal conductance at various temperatures with and without QCs. Panels (a)–(c) are reproduced from Sääskilahti *et al.*[54] Copyright@2014 American Physical Society. Panels (d)–(f) are reproduced from Xu *et al.*[153] Copyright@2022 The Royal Society of Chemistry.

 This journal is © the Owner Societies 2026

These spectrally resolved phonon transmissions accessible within MD frameworks enable the design of complex structures and even the inclusion of liquid phases, which lie beyond the capabilities of AGF or DMM methods. For example, Zhou *et al.*[113] showed ITC decreased with rough-interface thickness but increased for mass-graded interfaces, with FDDDM[123] spectral analysis confirming long-wavelength phonons passed through graded layers. Xu *et al.*[61] tuned Si/4H-SiC ITC from ~300 to ~1000 MW m^{-2} K^{-1} *via* nanopatterns, identifying competing phonon-boundary scattering and transport channel mechanisms. These MD results successfully explained the nonmonotonic nanostructure-mediated ITC tuning observed in experiments.[60,162]

Moreover, spectral analysis has been employed to probe solid/liquid interfacial thermal transport,[125,163–167] which is of growing importance for liquid cooling[168–171] and phase-change applications.[172–175] It is known that the ITC at solid–liquid interfaces can be tuned *via* surface structures,[176–181] bonding strength,[182,183] and adhesion energy.[184–189] However, owing to the development of spectral analysis methods, quantitative characterization of the ITC spectrum across solid/liquid interfaces has become possible only recently. The interfacial heat current across solid/liquid interfaces is statistically identical on both sides[125,190] as shown in eqn (14). Thus, the spectral heat flux across solid/liquid interfaces can be calculated using the solid side only. Based on this strategy, Sääskilahti *et al.*[125] found modes above 5 THz did not contribute at solid–Ar/liquid–Ar interfaces, with out-of-plane vibrations dominating for hydrophobic interfaces and transverse vibrations for hydrophilic interfaces. Li and Qiu[166] demonstrated a nonmonotonic pressure-dependent ITC at metal/water interfaces [Fig. 4(a)–(c)]. At the Cu/water interface, the ITC increased monotonically with pressure, driven by the gradual filling of the first adsorbed water layer, with enhanced transmission of almost all the vibrational modes [Fig. 4(a)]. In contrast, at the Pd/water interface, the ITC first increased due to the progressive filling of water molecules up to a critical pressure of 2.17 GPa and then decreased owing to the reduced vibrational overlap and the lower metal–water distance (than the equilibrium distance) at high pressures [Fig. 4(b) and (c)].

Furthermore, Xu *et al.*[163,164,167] using NEMD simulations, revealed the role of surface functionalization with self-assembled

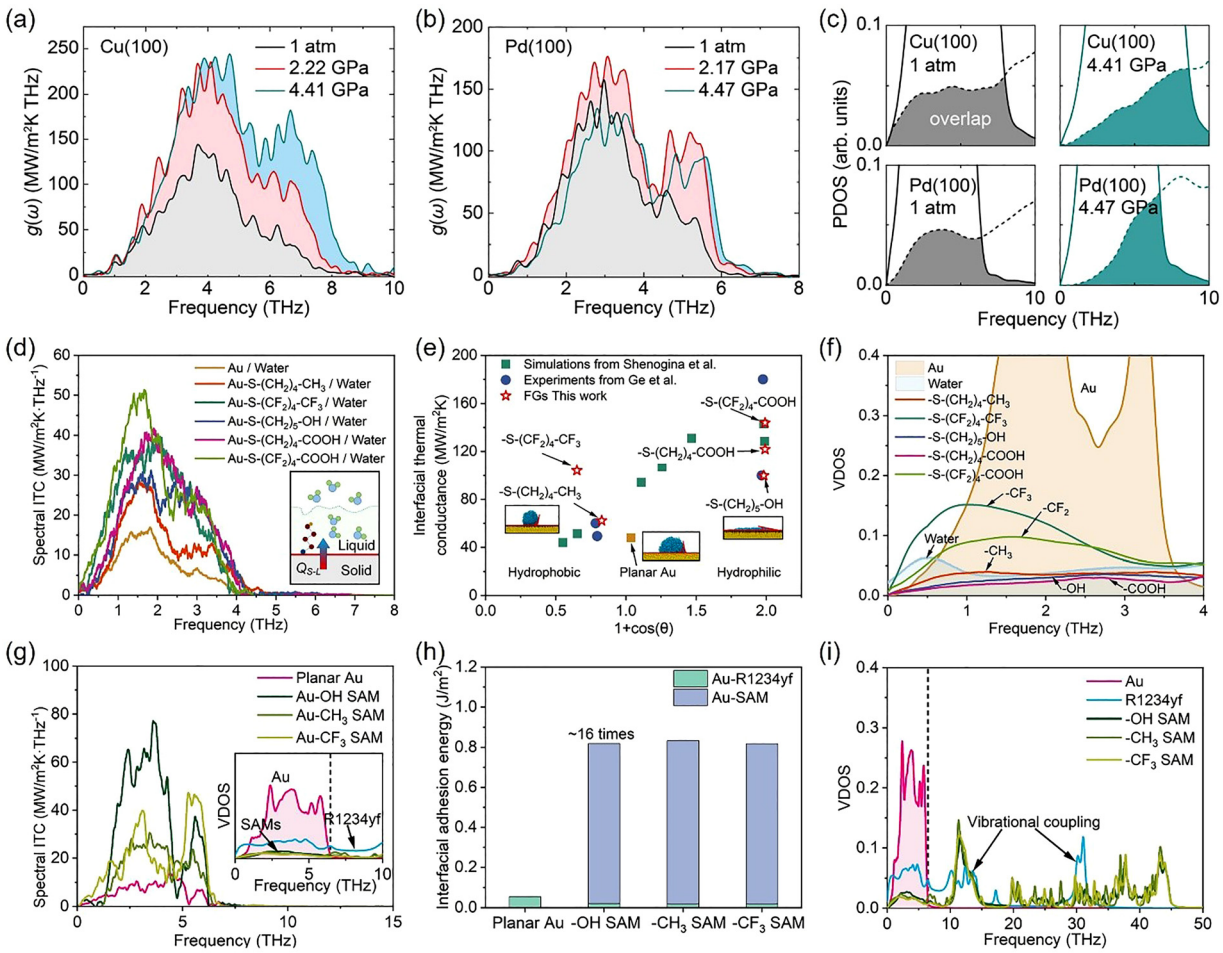


Fig. 4 Spectrally-resolved thermal transport across solid/liquid interfaces: (a)–(c) Cu/water and Pd/water interfaces under various pressures from Li and Qiu[166] Copyright@2026 Elsevier. (d)–(f) Au-SAM/water interfaces from Xu and Zhou[163] Copyright@2023 Elsevier, and (g)–(i) Au-SAM/R1234yf interfaces from Xu *et al.*[164] Copyright@2024 Elsevier.

monolayer (SAM)[191–193] in enhancing the ITC across solid/liquid interfaces [Fig. 4(d)–(i)]. They showed that SAMs can significantly enhance vibrational energy transmission across solid/liquid interfaces at low frequencies (*e.g.*, 0–4 THz for the Au/water interface [Fig. 4(d) and (g)]). This enhancement can be attributed to a collaborative effect including wettability control [Fig. 4(e)] and vibrational couplings [Fig. 4(f)]. This strategy can be further extended to other refrigerants, *e.g.*, R1234yf [Fig. 4(g)–(i)], and SAMs can improve the interfacial thermal conductance significantly ($\sim$7 times) between the liquid and substrate.[164]

While molecular dynamics (MD) simulations can yield detailed insights by resolving spectral interfacial thermal transport, they often lead to misleading comparisons with experiments due to inaccuracies introduced by the interatomic interactions. Meanwhile, MD simulations are inherently restricted to the nanoscale regime, which creates a gap between the fundamental physics they capture and their practical utilization. For instance, MD simulations lack predictive capability for thermal transport at the mesoscale, a length scale more relevant for many real-world applications.

C. Microscale and mesoscale modeling

The disconnect between scales is becoming particularly acute in modern microelectronics, *e.g.*, addressing heat dissipation has become increasingly urgent due to the rapid iteration of high-performance hardware serving artificial intelligence. MD and AGF calculations based on atomistic simulations remain constrained by the system size and therefore cannot be directly used to quantify transport across microscale architectures. Recently, these dynamics of phonons captured by atomistic simulations (*i.e.*, anharmonic lattice dynamics or AGF calculations with inputs from first-principles or MD simulations) have been transferred into mesoscale Boltzmann transport equation (BTE),[194–200] and subsequently used for predicting system-level thermal transport properties.[201] In these mesoscale simulations, the phonon transport is modeled by solving the multidimensional BTE using a solver such as Green's function,[202,203] lattice Boltzmann methods (LBM),[204–206] finite element method (FEM)[207,208] and discrete ordinates method (DOM).[209,210] Two comprehensive reviews have thoroughly examined the computation of submicron thermal transport using the mesoscale phonon BTE.[26,211]

However, it should be noted that interfacial thermal transport is usually simplified in these methodologies. Specifically, the ITR is treated as a boundary condition, often implemented using a simplified model with appropriate parameterization. For instance, the DMM [eqn (7)] is adopted to describe interfacial phonon scattering within mesoscale frameworks, which assumes phonons are either completely diffusely transmitted or reflected at the interface.[210] As a practical example, Hu *et al.* developed the GiftBTE solver, which employs an explicit DOM with second-order spatial accuracy.[197] This approach demonstrates excellent computational efficiency and enables realistic 3D simulations of real electronic devices [Fig. 5(a)]. Unlike large-scale simulations, where heat transport is treated as purely diffusive, phonon nonequilibrium at the microscale can be well characterized in the BTE solvers, *e.g.*, the localized hotspot with elevated temperatures in a FinFET, as illustrated in Fig. 5(a). This capability can be further extended to mimic Joule heating effects in complex microelectronic architectures, including silicon-based FinFETs[212] and gate-all-around field-effect transistors (GAAFETs)[199] [Fig. 5(b)]. Building on the GiftBTE, Shang *et al.* subsequently developed JAX-BTE[213] using a similar methodology, but with a GPU-accelerated implementation. This advancement significantly improves the computational efficiency of solving the mesoscale phonon BTE at submicron scales without sacrificing accuracy, as shown in Fig. 5(c) and (d). Moreover, JAX-BTE incorporates artificial intelligence acceleration techniques, such as the DeepONet model[214] (a neural network model) and physics-informed neural networks (PINNs).[215]

To date, a sophisticated treatment of interfacial conditions at the mesoscale remains an unresolved challenge. Current approaches rely on the parameters from analytical phonon transmission functions or a prescribed phonon transmission spectrum from atomistic simulations. Such strategies serve to reduce the complexity of solving multiscale phonon transport problems while maintaining a balance between computational efficiency and accuracy. For instance, the AMM is appropriate for smooth, well-bonded interfaces at low temperatures or in regimes dominated by long-wavelength phonons, where elastic and nearly specular transmission is expected. The DMM is suitable for rough, disordered, or high-temperature interfaces where phase memory is largely lost and diffuse scattering dominates. In mesoscale BTE or device-level simulations, simple interfacial boundary conditions can provide useful predictions when they are calibrated against experiments or atomistic calculations and when the detailed spectral distribution is not the main target. However, this simplification usually comes at a cost. For instance, interfacial microstructural details,[60,61] roughness,[55,58] and inelastic scattering processes[52,53] are neglected in the DMM. At the same time, the phonon wave-like effect in the near-interface region[216–218] and interfacial localized modes[50,51,219] are also disregarded during mesoscale simulations. These omissions may lead to significant deviations in predicting the thermal response of systems where the ITR constitutes the dominant bottleneck.

IV. Experimental spectroscopy techniques

Experimental spectroscopy techniques have been developed to probe thermal energy transport across both spatial and temporal scales, ranging from femtoseconds at the nanometer scale to microseconds at the micrometer scale. In general, these techniques can be classified into two categories based on their underlying principles, *i.e.*, steady-state and transient measurements. As the names imply, steady-state methods detect a constant signal response such as the spatial distribution of temperature to extract thermal transport coefficients. These methods include thermal bridge method,[220,221] electron beam

 This journal is © the Owner Societies 2026

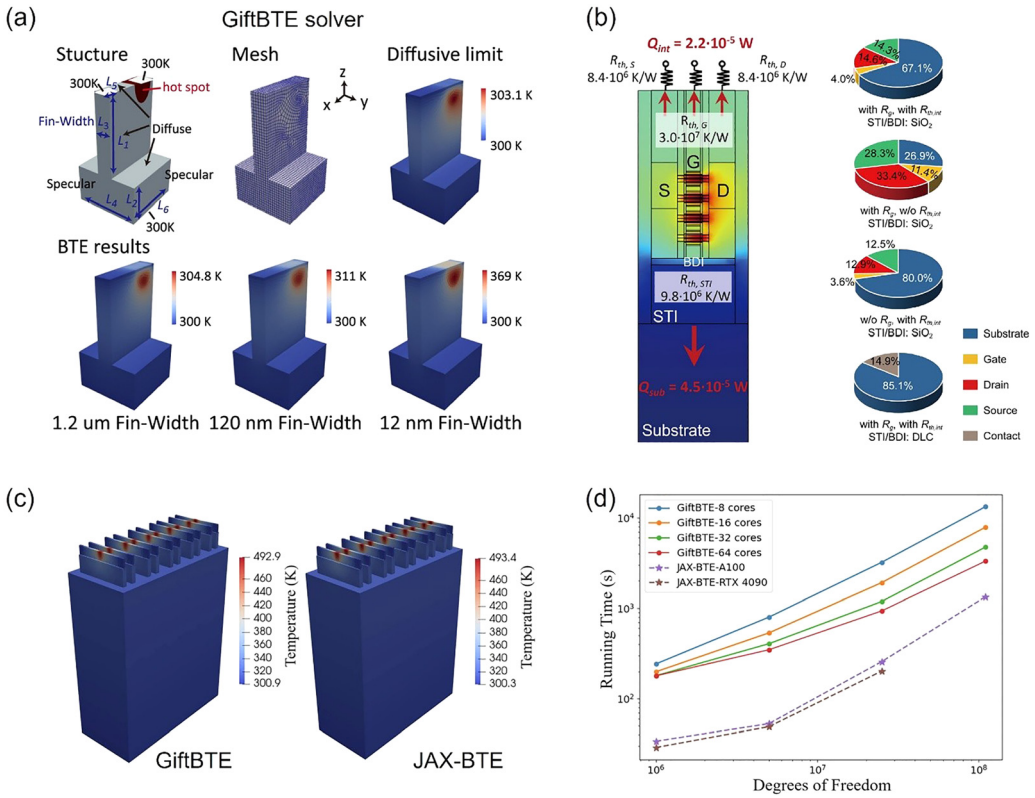


Fig. 5 Mesoscale modeling of phonon transport in integrated electronics. (a) Temperature field of FinFET with a hotspot calculated by GiftBTE, from Hu *et al.*[197] Copyright@2024 IOP Publishing. (b) Heat dissipation pathways in the stacked nanosheet GAAFET from Sheng *et al.*[199] Copyright@2025 IEEE Xplore. $R_{th,S}$, $R_{th,G}$, and $R_{th,D}$ represent the thermal resistances of the interconnections connected to the source, gate, and drain, respectively. (c) Temperature distribution for the linear transistor array simulated by GiftBTE and JAX-BTE, respectively. (d) Scalability comparison between JAX-BTE and GiftBTE across different problem sizes. Panels (c) and (d) are from Shang *et al.*[213] Copyright@2025 Springer Nature.

self-heating method,[222,223] photothermal Raman method[224–226] and recently developed steady-state scanning transmission electron microscopy coupled with electron energy-loss spectroscopy (STEM-EELS).[227] In contrast, transient methods collect time-dependent responses, such as the decay of temperature within a specific time window, which are then input into a thermal model to determine the transport properties. These methods include 3ω method,[228,229] frequency-domain thermoreflectance (FDTR),[230,231] time-domain thermoreflectance (TDTR),[232–234] laser flash Raman spectroscopy,[235,236] and electron beam thermal waves.[237] Given the need to resolve heat carrier dynamics directly at interfaces where fine temporal and spatial resolution is required, the following discussions will focus primarily on FDTR, TDTR and steady-state STEM-EELS methods.

A. Frequency-domain thermoreflectance

FDTR method has been widely used to characterize the interfacial thermal transport.[230,231,238–241] The schematic of FDTR is shown in Fig. 6(a).[242] In this approach, a pump–probe configuration is utilized to excite the sample and monitor the resulting changes in thermoreflectance signal. A pump laser (typically continuous wave), modulated at frequencies ranging from kHz to MHz, is focused onto the sample surface through a microscope objective, thereby generating a periodic heat source with a Gaussian spatial distribution. The probe beam is collinearly aligned with the pump beam to detect the corresponding small, periodic temperature oscillations *via* variations in reflectivity at the heated spot. Prior to FDTR measurements, a thin metal transducer film is typically deposited on the sample surface. The transducer is chosen to efficiently absorb the modulated pump beam, minimize unwanted probe beam heating, and provide a large thermoreflectance coefficient at the probe wavelength.[231,243] The amplitude and phase lag of the probe signal with respect to the pump modulation are measured using a lock-in amplifier as a function of modulation frequency, and the relevant thermal parameters are subsequently extracted by fitting the measured phase response to an appropriate heat conduction model. Briefly, the heat conduction equation of each layer is first given for a real multilayer system, given by

$$\frac{\kappa_r}{r}\frac{\partial}{\partial r}\left(r\frac{\partial T}{\partial r}\right)+\kappa_z\frac{\partial^2 T}{\partial r^2}=C_p\frac{\partial T}{\partial t} \tag{24}$$

in which κ_r and κ_z are the in-plane and out-plane thermal conductivity, respectively. T and C_p are the temperature and volumetric heat capacity, respectively. Taking the Fourier transform and Hankel transforms, eqn (24) can be rewritten as:

$$\kappa_z\frac{\partial^2\theta(\omega,k,z)}{\partial z^2}=\left(\kappa_r k^2+C_p i\omega\right)\theta(\omega,k,z) \tag{25}$$

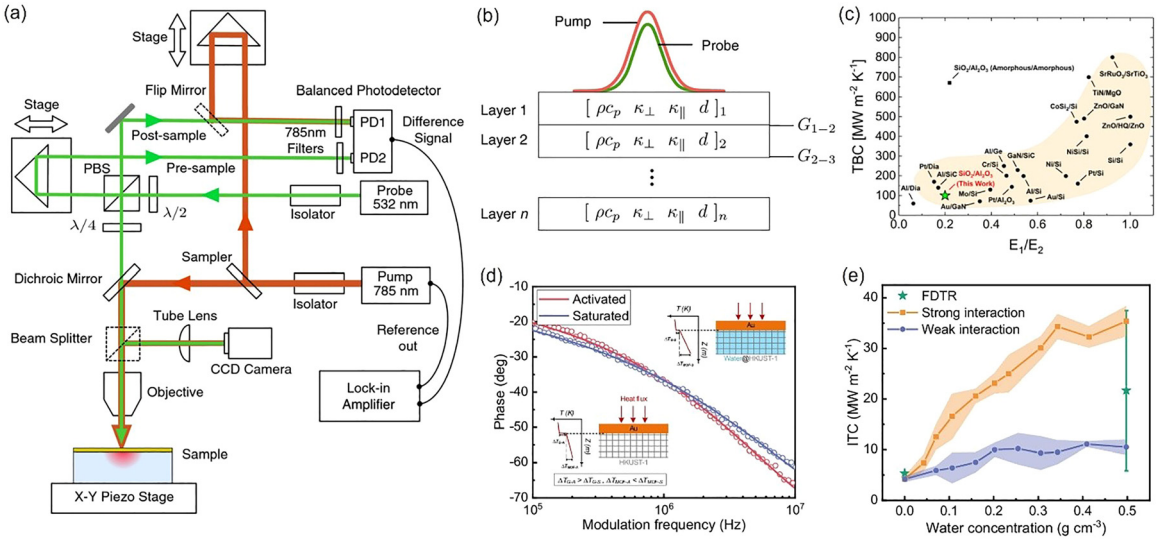


Fig. 6 (a) Schematic of FDTR microscope based on two cw diode lasers from Yang *et al.*[242] Copyright@2013 American Institute of Physics. (b) Model for fitting heat conduction in a multilayer sample with Gaussian pump and probe spots from Yang *et al.*[242] (c) Measured TBC of solid/solid interface as a function of the ratio between elastic moduli of adjacent materials from Warzoha *et al.*[244] Copyright@2024 American Chemical Society. (d) Typical FDTR phase response for the Au/HKUST-1 interface as a function of pump modulation frequency from Wang *et al.*[92] The corresponding (e) measured and calculated ITC of Au/HKUST-1 interfaces with adsorbed water molecules from Wang *et al.*[92] Copyright@2024 Springer Nature.

The solution to eqn (25) is given by:

$$\begin{pmatrix} \theta_{n,\mathrm{b}} \\ f_{n,\mathrm{b}} \end{pmatrix} = \begin{pmatrix} \cosh(qd) & -\dfrac{\sinh(qd)}{\kappa_z q} \\ -\kappa_z q \sinh(qd) & \cosh(qd) \end{pmatrix} \begin{pmatrix} \theta_{n,\mathrm{t}} \\ f_{n,\mathrm{t}} \end{pmatrix} \quad (26)$$

in which q^2 equals $(\kappa_r k^2 + C_p i\omega)/\kappa_z$ and d is the thickness of the layer. For a multilayer system [Fig. 6(b)], the solution becomes

$$\begin{pmatrix} \theta_{\mathrm{b}} \\ f_{\mathrm{b}} \end{pmatrix} = M_N M_{N-1} \cdots M_2 M_1 \begin{pmatrix} \theta_{\mathrm{t}} \\ f_{\mathrm{t}} \end{pmatrix} = \begin{pmatrix} A & B \\ C & D \end{pmatrix} \begin{pmatrix} \theta_{\mathrm{t}} \\ f_{\mathrm{t}} \end{pmatrix} \quad (27)$$

When the bottom layer can be treated as adiabatic or semi-infinite, the surface temperature is then given by $\theta_t = -D/Cf_t$, and the final measured phase signal is given by:

$$\phi = \tan^{-1} \frac{\Im(H(\omega))}{\Re(H(\omega))} + \phi_{\mathrm{system}} \quad (28)$$

in which $H(\omega)$ is the inverse Hankel transform of surface temperature, given by

$$H(\omega) = \frac{A_0}{2\pi} \int_0^\infty k \left(\frac{-D}{C}\right) \exp\left[\frac{-k^2(\omega_0^2 + \omega_1^2)}{8}\right] \mathrm{d}k \quad (29)$$

A typical phase fitting and its sensitivity are shown in Fig. 6(d). The desired thermal properties of materials can be acquired from the fitting.

Numerous studies have been conducted using the FDTR method to measure the thermal properties of materials.[108,109,242,244–247] However, typically, this technique only provides a general value of thermal properties but lacks the spectral information which requires further analysis by other methods.[231,248–251] For instance, Warzoha *et al.*[244] compared the thermal boundary conductance (TBC) at various solid–solid interfaces and found that the TBC can be effectively characterized by the ratio of the elastic moduli of the adjacent materials. This correlation can be rationalized by the closer vibrational density of states contributed by low-frequency modes, given that materials with similar elastic moduli typically exhibit comparable acoustic group velocities.[139] Furthermore, Wang *et al.*[92] used the FDTR method to investigate the thermal transport across interface with complex materials, *i.e.*, the gold/HKUST-1 interfaces [Fig. 6(d) and (e)]. A tuneable ITC was observed by changing the water adsorption of HKUST-1. The ITC of gold/HKUST-1 without adsorbed water molecules is 5.33 MW m^{-2} K^{-1}, which can be further largely increased to ~35 MW m^{-2} K^{-1} with the adsorbed water molecules [Fig. 6(e)]. Combined with MD simulations, further spectral analysis is provided. Adsorbed water molecules activate more high-frequency vibrations which can participate in the interfacial heat transfer, resulting in the high ITC [Fig. 6(e)]. Besides the MD simulations, the theoretical models including DMM and AMM are commonly used for the spectral understanding of interface thermal transport.[252–255] Freedman *et al.*[256] employed the FDTR method to measure the ITC between Au_xCu_{1-x} and Au_xPd_{1-x} alloy films and sapphire substrates. DMM is used to predict and explain the experimentally observed variation of ITC with alloy composition. Through the calculation of phonon dispersion and transmission coefficients, the variation of ITC with alloy composition is attributed to elastic scattering between high-frequency phonons from Pd and Cu and phonons in sapphire.

Besides solid/solid interface measurements, the thermal properties of solid/liquid interfaces can be measured using FDTR.[257–259] The FDTR is further used to detect the solid/liquid interfacial thermal transport.[186,260–263] For example, Meng *et al.*[259] established the continuous wave FDTR (CW-FDTR) and developed the two-way heat conduction model to characterize the

 This journal is © the Owner Societies 2026

solid–liquid interface thermal resistance. Both the thermal conductivities of water, ethanol, and hexadecane and the thermal resistance between them and the transducer can be well measured. In addition, based on the same pump–probe measurement principle, Jiang *et al.*[264–266] proposed a differential square-pulsed source (DSPS) method to investigate the interface thermal transport which can measure wider range of solid/liquid interfaces with high sensitivity compared with the FDTR method.

Beyond static material property correlations, advances in thermoreflectance techniques have enabled direct experimental access to the transition between ballistic and diffusive phonon transport. Regner *et al.*[267] demonstrated a breakdown in diffusive phonon transport by introducing high-frequency surface temperature modulation, an approach known as broadband frequency-domain thermoreflectance (BB-FDTR), as illustrated in Fig. 7(a). As shown in Fig. 7(b), the surface temperature oscillation can be correlated with the thermal penetration depth, which is tuned by the heating frequency, *i.e.*, a crossover between ballistic and diffusive phonon transport regimes can thus be clearly observed. Consequently, by systematically varying the heating frequency, one can identify the mean-free-path-dependent contributions of phonons to thermal transport,[267,268] as shown in Fig. 7(c). However, the implications of such ballistic transport effects on interfacial thermal transport remain experimentally unexplored. Similarly, the contribution of phonon mean free paths to interfacial thermal conductance has yet to be investigated using BB-FDTR.

B. Time-domain thermoreflectance

The TDTR and FDTR methods share a similar heat transport model and measurement configuration.[233,269,270] The key distinction lies in their respective measurement domains. In TDTR, the laser modulation frequency is held constant while the signal is recorded as a function of the delay time τ, whereas in FDTR, the delay time is fixed and the modulation frequency is swept over a broad range.[238] Hence, the fitting curves obtained from the two methods are markedly different.

In TDTR experiments, the pump and probe laser pulses arrive at the sample surface with an ultrashort pulse width, typically less than 300 fs. Under a small temperature excursion, the thermophysical properties of the sample can be assumed to remain constant, and the heat-transport system can be regarded as a linear time-invariant one. For such a system, the response to multiple inputs is the superposition of the responses to each individual input. To improve the signal-to-noise ratio, the pump pulse train is usually modulated by an electro-optic or acousto-optic modulator and the periodic surface-temperature response from the reflected probe signal is demodulated with a lock-in amplifier. The transfer function

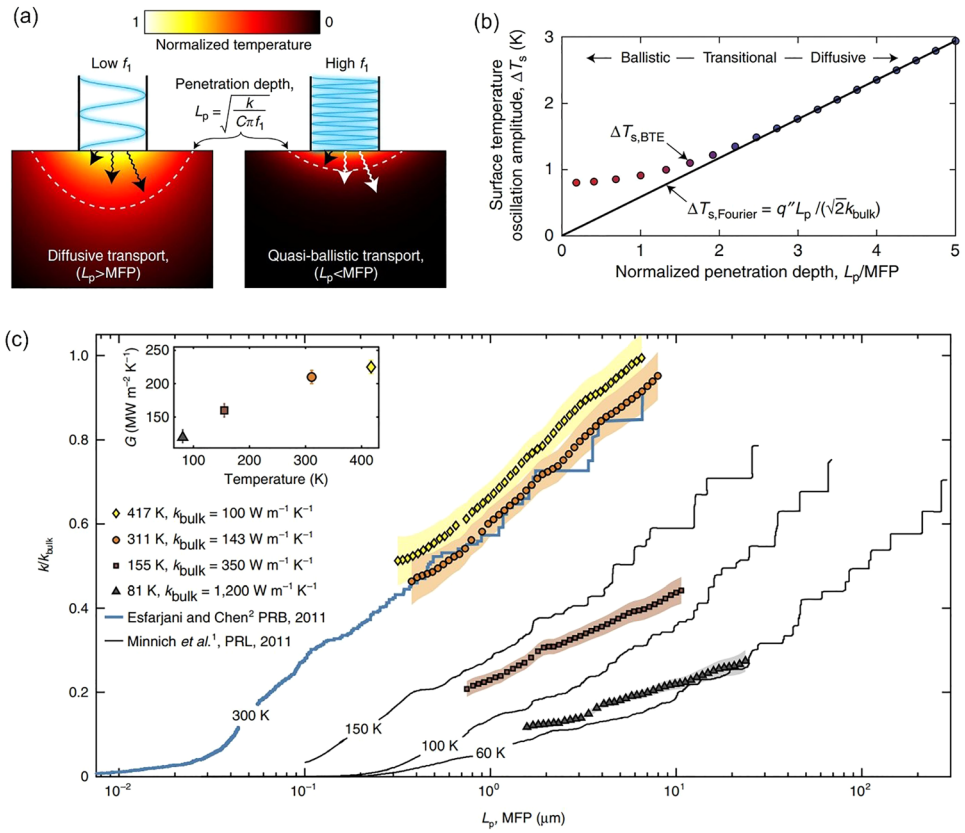


Fig. 7 (a) Schematic of BB-FDTR technique used to measure phonon MFP spectra. (b) Spatial variation of the temperature oscillation amplitude for various transport regimes (from the ballistic to diffusive). Amplitude of the surface temperature oscillation is shown here. (c) Measured mean free paths with their accumulative thermal conductivities and the thermal conductance. The panels are from Regner *et al.*[267] Copyright@2013 Springer Nature.

of the whole linear time-invariant system can be expressed as $Z(\omega_0)$, and the output of the lock-in amplifier can be written as:

$$Ae^{i(\omega_0 t+\phi)} = Z(\omega_0)e^{i\omega_0 t} \quad (30)$$

where $e^{i\omega_0 t}$ is the reference signal, ω_0 is the modulation frequency of the pump pulse, A is the signal amplitude, and the phase term is a function of the delay time between the pump and probe pulses, which contains information about the thermophysical properties of the sample.

The transfer function $Z(\omega_0)$ can also be represented by the frequency-domain response of the pulsed signal $H(\omega)$:[271]

$$Z(\omega_0) = \frac{\beta Q Q_{\text{probe}}}{T^2} \sum_{k=-\infty}^{\infty} H(\omega_0 + k\omega_s)e^{ik\omega_s \tau} \quad (31)$$

where Q is the power of each pump pulse, Q_{probe} is the power of each probe pulse, and the constant term β includes the thermoreflectance coefficient and the electronic gain of the detection system. ω_s is the sampling frequency, also known as the repetition rate of the laser pulses. τ is the delay time between the pump and probe pulses. The term $H(\omega)$ received by the lock-in amplifier corresponds to the surface thermal response generated under periodic thermal excitation at ω_0, which has the same form as eqn (29) introduced in the FDTR section.

Fig. 8a shows the TDTR-measured signal in the SAM-modified Cu/diamond system. In these measurements, it is found that a weak van der Waals interface can have a higher ITC than the strongly covalently bonded Cu/diamond interface (Fig. 8b), but this unique phenomenon was not observed in copper/silicon and copper/sapphire systems.[272] Similar to the FDTR measurements, with the help of molecular dynamics, this unique enhancement is ascribed to the strong bridging effect of a highly vibrationally mismatched interface. SAMs can also be used to modify solid–liquid interfaces, thereby altering surface wetting conditions[273–276] and consequently regulating interface heat transfer at the solid–liquid interface.[185,277] Ge *et al.*[186] employed TDTR method to measure the ITC of Au/water and Al/water interfaces by coating surfaces with different types of SAMs, ranging from hydrophobic to hydrophilic surfaces. Hydrophilic surfaces exhibit higher ITC than hydrophobic surfaces. Following this observation, Shenogina *et al.*[184] proposed a linear relationship between the ITC and adhesion energy by calculating surfaces modified with various SAMs exhibiting different contact angles. Although this trend has also been reported in other experiments and simulations[185,192,278,279] and is ascribed to the bonding effect, the important role of vibrational coupling at the interface is ignored.[163,164,167,191,280] Recently, Li *et al.*[281] used TDTR to measure the dynamical switching of ITC across molecular junctions under an electric field, revealing the modulation of interface bonding effects on ITC. In addition to measuring the cross-plane thermal conductivity κ_z and interfacial thermal conductance G by "standard" TDTR, several advanced TDTR configurations have been developed over the past decade to measure specific thermal properties. Early TDTR analyses generally assumed in-plane isotropic heat conduction, which is appropriate for extracting cross-plane thermal conductivity under axisymmetric heating conditions. Although the TDTR signal is intrinsically most sensitive to heat flow in the cross-plane direction, properly designed configurations can provide access to in-plane thermal transport. One representative example is the beam-offset TDTR configuration.[282] Unlike conventional concentric-beam TDTR, beam-offset TDTR intentionally breaks the in-plane symmetry by laterally displacing the pump and probe spots. As shown in Fig. 9(a), the pump beam is scanned across the probe beam, and the full width at half maximum (FWHM) of the out-of-phase signal V_{out} at a negative delay time is compared with thermal-model calculations to extract the in-plane thermal conductivity along the scanning direction. In such measurements, a NbV transducer with lower thermal conductivity than Al is often preferred, because it reduces lateral heat spreading within the transducer and increases the sensitivity of the measured FWHM to heat spreading in the substrate, thereby lowering the uncertainty in the extracted in-plane thermal conductivity.[283]

However, for fully three-dimensional anisotropic materials, beam-offset fitting can become computationally demanding because the loss of in-plane symmetry requires a fully anisotropic heat-transport model. To address this challenge, Li *et al.*[284] developed an asymmetric-beam time-domain thermoreflectance method (AB-TDTR). As shown in Fig. 9(b), this method introduces an elliptical laser spot to measure anisotropic heat transport along arbitrary cross-plane or in-plane directions. Instead of relying on a circular beam or scanning the pump beam across the probe beam, AB-TDTR introduces an elliptical laser spot to intentionally break the in-plane symmetry of the temperature field. The elliptical beam is positioned on the sample surface with a well-defined major axis y and minor axis x, and the sample is rotated so that the in-plane thermal-transport direction to be measured is aligned with the major axis. The resulting asymmetric temperature distribution enhances the directional sensitivity of the TDTR signal and provides a more efficient route for extracting anisotropic thermal conductivity than conventional beam-offset fitting in fully anisotropic systems.

Because the in-plane symmetry is absent in anisotropic materials, it is more convenient to rewrite eqn (24) in Cartesian coordinates rather than cylindrical coordinates. The heat diffusion equation in Cartesian coordinates can be written as:

$$\begin{aligned} C_p\frac{\partial T}{\partial t} &= K_x\frac{\partial^2 T}{\partial x^2} + K_y\frac{\partial^2 T}{\partial y^2} + K_z\frac{\partial^2 T}{\partial z^2} + 2K_{xy}\frac{\partial^2 T}{\partial x \partial y} \\ &\quad + 2K_{xz}\frac{\partial^2 T}{\partial x \partial z} + 2K_{yz}\frac{\partial^2 T}{\partial y \partial z} \end{aligned} \quad (32)$$

When the orthogonal Cartesian axes are selected along the principal thermal-transport directions of the material, the off-diagonal elements of the thermal-conductivity tensor vanish, namely $K_{xy} = K_{xz} = K_{yz} = 0$.

 This journal is © the Owner Societies 2026

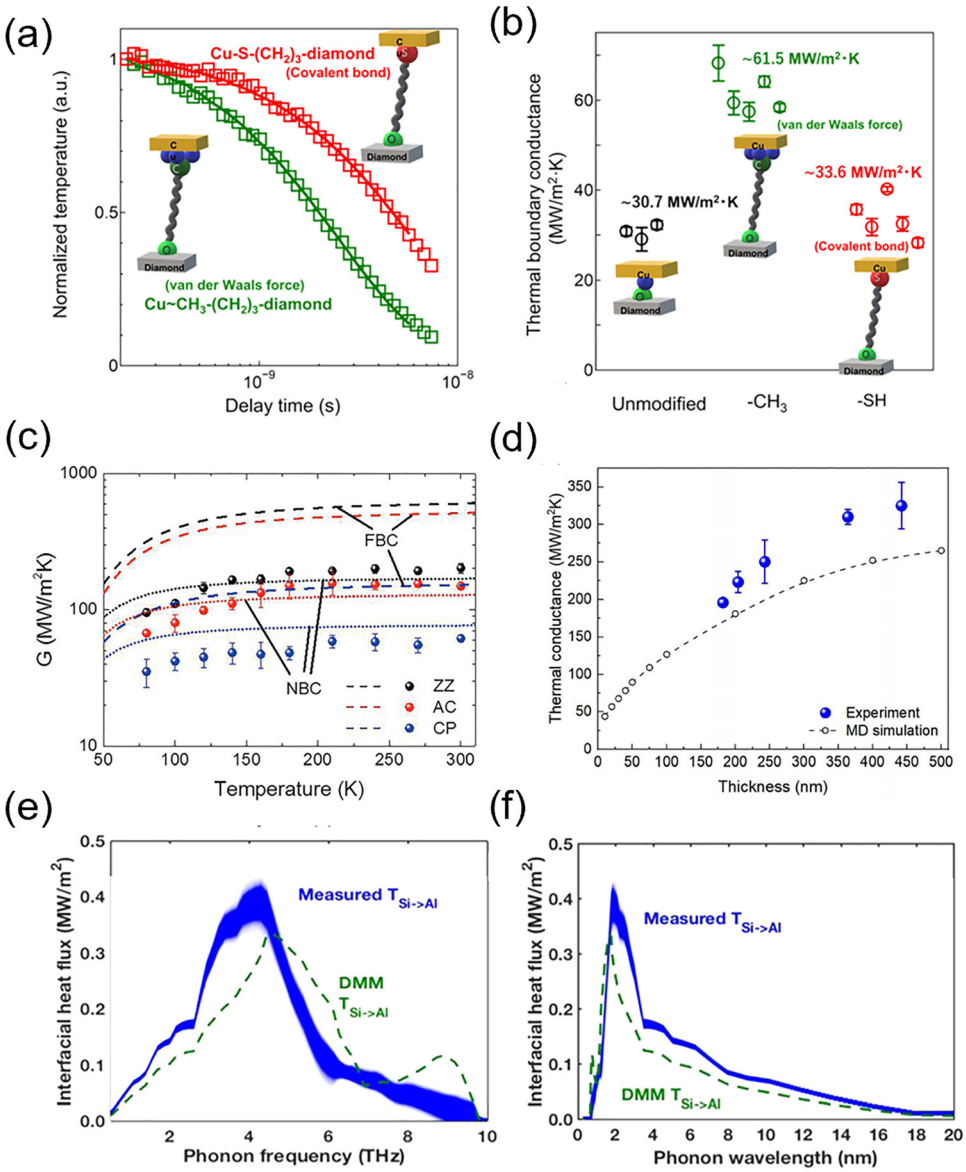


Fig. 8 (a) The representative TDTR measurement signal of functionalized copper/diamond interfaces and (b) the fitted ITC results from Xu *et al.*[272] Copyright@2021 American Association for the Advancement of Science. (c) Temperature-dependent interfacial thermal conductance of Al/BP interfaces with zigzag, armchair, and cross-plane orientations from Li *et al.*[285] Copyright@2019 Wiley. Dots represent experimental measurements, while lines denote diffuse mismatch model calculations under different phonon branch-conversion assumptions. FBC and NBC correspond to free branch conversion and no branch conversion, respectively. (d) GaN-thickness-dependent TBC obtained from TDTR measurements and compared with molecular dynamics simulation results from Li *et al.*[288] (e) and (f) Spectral heat flux measured at the interface (blue line) and from the DMM (green dashed line), respectively, *versus* (e) phonon frequency and (f) phonon wavelength. The panels (e) and (f) are from Hua *et al.*[43] Copyright@2017 American Physical Society.

In this case, the surface temperature change in Fourier space can be expressed as:

$$T(k_x, k_y) = \left(-\frac{D}{C}\right)\frac{A_0}{2\pi}\exp\left(-\frac{w_{0,x}^2 k_x^2 + w_{0,y}^2 k_y^2}{8}\right) \quad (33)$$

where k_x and k_y are the spatial-frequency variables in Fourier space, $w_{0,x}$ is the $1/e^2$ radius of the pump beam along the x direction, and $w_{0,y}$ is the $1/e^2$ radius of the pump beam along the y direction. A_0 is the power absorbed, and A_s is the reflected probe power. Since the photodetector receives the total reflected signal over the entire area covered by the probe beam, the frequency-domain response function of the whole system can be written as:

$$H(\omega) = \frac{A_0 A_s}{4\pi^2}\iint_{-\infty}^{\infty}\left(-\frac{D}{C}\right) \times \exp\left(-\frac{\left(w_{0,x}^2 + w_{s,x}^2\right)k_x^2 + \left(w_{0,y}^2 + w_{s,y}^2\right)k_y^2}{8}\right)\mathrm{d}k_x\mathrm{d}k_y \quad (34)$$

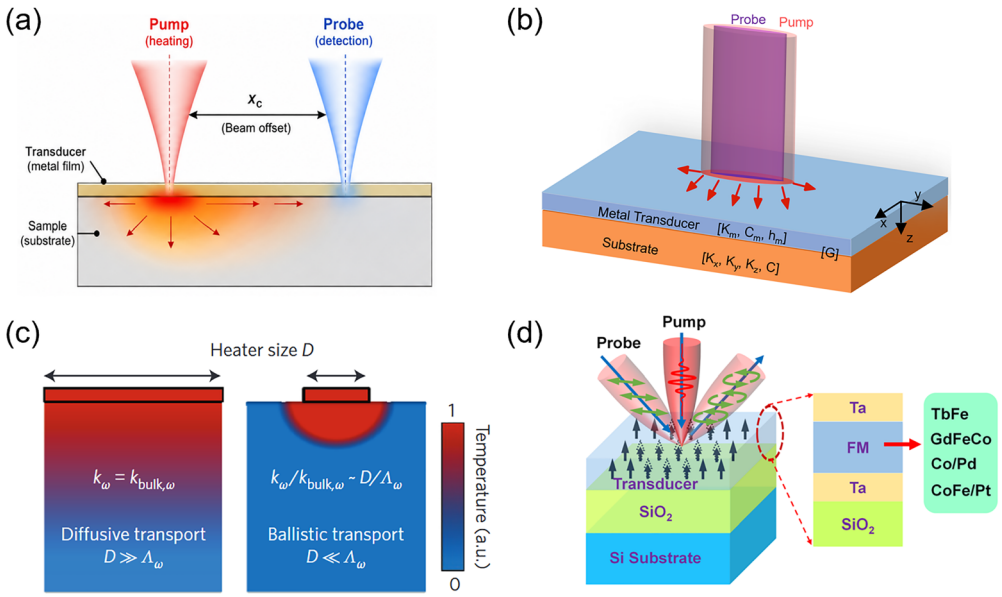


Fig. 9 (a) Beam-offset TDTR configuration, where the pump and probe beams are laterally separated by x_c. The pump beam generates localized heating, and the probe beam detects the temperature response at an offset position, allowing in-plane heat spreading to be evaluated. (b) AB-TDTR configuration for anisotropic thermal conductivity measurements, in which an elliptical beam generates an asymmetric temperature field to enhance directional sensitivity to heat transport. (c) Schematic of thermal transport governed by the heater size D and phonon mean free path Λ_ω from Hu *et al.*[286] Copyright@2015 Springer Nature. In the diffusive regime ($D \ll \Lambda_\omega$), phonons undergo sufficient scattering within the heated region and Fourier heat conduction is valid. In the ballistic regime ($D \ll \Lambda_\omega$), long-mean-free-path phonons are partially suppressed, leading to a reduction in the effective thermal conductivity of individual phonon modes. (d) TR-MOKE measurement mechanism and sample structures of four magnetic thin-film transducers from Chen *et al.*[293] Copyright@2016 American Chemical Society. Here, FM represents ferromagnetic or ferrimagnetic films, including multilayers denoted by "/" and alloy films.

With the full consideration of anisotropic heat conduction processes, TDTR can be used to accurately determine the thermal resistance across buried interfaces. It has been widely used to study how interfacial bonding, molecular layers, surface wettability, and vibrational coupling regulate interfacial thermal conductance. As shown in Fig. 8(c), Li *et al.*[285] revealed a strongly orientation-dependent thermal boundary resistance in Al/black phosphorus interfaces using TDTR, demonstrating that interfacial heat transport was closely linked to the anisotropic phonon band structure and mode-dependent phonon transmission.

Beyond the measurement of diffusive heat conduction processes, TDTR can also be used to study non-Fourier heat-transport behavior. When the heating size or thermal penetration depth becomes comparable to the phonon mean free path, long-mean-free-path phonons cannot undergo sufficient scattering within the local heating region to establish local thermal equilibrium. As a result, the apparent thermal conductivity measured by TDTR becomes dependent on the characteristic length scale. Based on this principle, Hu *et al.*[286] fabricated nanopatterned metallic heaters to reduce the heating size in conventional TDTR from the micrometer scale to the nanometer scale as shown in Fig. 9(c). By using the suppression of thermal conductivity caused by quasi-ballistic heat transport, they reconstructed the spectral contribution of phonon mean free paths to the thermal conductivity of different materials. Size-dependent TDTR measurements on high-quality single-crystal BAs[287] revealed a pronounced reduction in the effective thermal conductivity as the heating size decreases, reflecting the onset of quasi-ballistic phonon transport and the dominant contribution of long-mean-free-path phonons to its ultrahigh thermal conductivity. Similar length-scale effects can also appear in interfacial heat transport, *e.g.*, Li *et al.*[288] observed a strong size dependence of ITC across bonded GaN–AlN interfaces using TDTR measurements [Fig. 8(d)], revealing that the limited size of GaN can significantly suppress phonon transmissivity across the interface.

The lack of direct measurements of detailed spectral information in FDTR and TDTR methods limits the further exploration of interface thermal transport. Recently, Hua *et al.*[43] achieved the spectral information extraction of the interface thermal transport at Al/Si interface through the combination of BTE and TDTR method. In TDTR, the modulation frequency of the laser can be varied in addition to the time delay, enabling access to richer spectral information. The experimental data, which comprised phase and amplitude measured at modulation frequencies of 2.68, 5.51, and 9.79 MHz, were fitted with Boltzmann transport equation simulations to extract the phonon transmission coefficient. The obtained transmission coefficient was further used to determine the spectral interfacial heat flux as a function of phonon frequency and wavelength, enabling direct comparison with predictions from the DMM [Fig. 8(e) and (f)]. They found that low-frequency modes (below 4 THz) contribute more to interfacial thermal transport than predicted by the DMM.

 This journal is © the Owner Societies 2026

In addition to probing phonon-mediated heat transport, TDTR and related ultrafast optical techniques can provide not only thermal information but also carrier-transport and energy-relaxation information. Yue *et al.*[289] employed transient reflectivity microscopy to visualize the diffusion of photoexcited carriers in cubic BAs and extracted a high ambipolar mobility of approximately 1550 $cm^2\ V^{-1}\ s^{-1}$, demonstrating that BAs combines ultrahigh thermal conductivity with excellent carrier transport. Li *et al.*[290] further used ultrafast pump–probe spectroscopy to study hot-electron relaxation in metallic θ-TaN and found a relaxation time of about 15 ps, much longer than that in conventional metals such as Cu and Al. These results confirm weak electron–phonon coupling and support the phonon-dominated ultrahigh thermal conductivity of θ-TaN.[291] These examples illustrate that, with appropriate modifications in optical excitation and signal analysis, ultrafast optical techniques are promising for studying electron–phonon coupling at interfaces. A useful methodological precedent is the three-pulse photoacoustic spectroscopy developed by Liao *et al.*,[292] in which a three-pulse scheme was used to generate free carriers in silicon and directly measure carrier-induced damping of a coherent sub-terahertz phonon mode. Similar strategies could be extended to heterogeneous interfaces to elucidate how carriers, phonons, and their mutual coupling jointly govern interfacial energy transport.

Moreover, relying on the change in thermoreflectance, TDTR can also use the temperature-dependent transient polar Kerr rotation to detect the temperature response of a magnetic transducer under pump-laser heating. This technique is known as the time-resolved magneto-optic Kerr effect (TR-MOKE).[293–295] In TR-MOKE, the pump beam heats a magnetic transducer layer, and the resulting temperature-induced change in magnetization leads to a change in the Kerr rotation angle of the reflected probe beam. This small polarization rotation is converted into a differential electrical signal using a half-wave plate, a Wollaston prism, and a balanced photodetector, followed by lock-in detection. Since the TR-MOKE signal changes sign when the magnetization direction is reversed, whereas many parasitic signals arising from ordinary thermoreflectance, scattered light, or Brillouin oscillations are largely independent of the magnetization direction, subtracting the signals acquired under opposite magnetization states allows a cleaner MOKE-based temperature response to be isolated. This differential detection scheme improves the rejection of spurious optical signals and reduces sensitivity to surface-scattering artifacts. Fig. 9(d) shows the TR-MOKE measurement mechanism and the sample structures of four representative magnetic thin-film transducers.[293] Beyond serving as a temperature probe for magnetic transducers, TR-MOKE is particularly promising for studying interfacial spin-dependent heat transport. For example, Kimling *et al.*[294] used TR-MOKE to study the picosecond spin Seebeck effect in normal-metal/YIG bilayers, where an ultrafast interfacial temperature difference between metal electrons and YIG magnons drives a spin current across the interface. The resulting spin accumulation was detected through time-resolved Kerr rotation, enabling the interfacial spin Seebeck response to be isolated from bulk thermal-gradient effects.

C. Advanced spectroscopic methods

The advancement of electron energy loss spectroscopy (EELS) in scanning transmission electron microscopy (STEM) enables nanoscale vibrational measurements.[32,296–300] A comprehensive review of this technique, including the principles of STEM-EELS, was recently provided by Xu *et al.*[33] Here, we only briefly introduce representative examples of its application. In this technique, electron probes with high spatial, momentum, and energy resolution are used to scan across a thin sample, and spatially resolved EELS spectra can be acquired, enabling the detection and observation of local vibrational modes. Cheng *et al.*[48] combined both Raman spectroscopy and EELS in STEM to investigate heat transfer at the high-quality epitaxial Si–Ge interface [Fig. 10(a)]. The localized interfacial phonon modes were directly observed, which contribute to the interfacial heat transfer [Fig. 10(b) and (c)]. In addition, the recently developed four-dimensional EELS (4D EELS) technique provides the opportunity for local vibrational measurements with high spatial and momentum resolution, overcoming the challenge of achieving high momentum and spatial resolution simultaneously.[301,302] Qi *et al.*[299] used the 4D EELS technique to measure the interfacial vibrations of epitaxial cubic boron nitride/diamond heterointerface. The local vibrational spectra and the interfacial phonon dispersion relation were directly measured. Beyond the visualization of interface phonon modes, by analysing the electron energy loss/gain (EEL/EEG) signals in EELS-STEM technique, the nanoscale temperature can be measured, which can be directly compared with calculations. Liu *et al.*[227] generated a stable temperature gradient at the AlN/SiC system and obtained record-high-resolution spatial temperature distributions at the interface using the STEM-EELS technique [Fig. 10(d) and (e)]. The comparison with non-equilibrium molecular dynamics showed that interfacial phonon modes preferentially coupled with high-frequency bulk phonon modes during inelastic scattering.

In addition, besides the EELS-STEM method, a few works have demonstrated that X-ray diffuse scattering and ultrafast electron diffuse scattering can provide a time-, momentum- and mode-resolved phonon population variations after laser excitation.[303–305] These measurements directly reveal phonon energy changes involving phonon–phonon and phonon–electron scattering. However, most works are limited to bulk crystalline materials given the well-defined Brillouin zone and phonon population. Recently, in order to extend this technique to the frequency-resolved interfacial thermal transport regime, Chen *et al.*[306] coupled a machine learning method with BTE to reconstruct the measured data of ultrafast electron diffraction and extract the frequency-dependent relaxation time and transmission coefficients. After applying it to the Au/Si system with real experimental data, a large discrepancy from the diffuse mismatch model is observed around 3.26 THz, demonstrating the ability of this method and the limitations of the DMM.

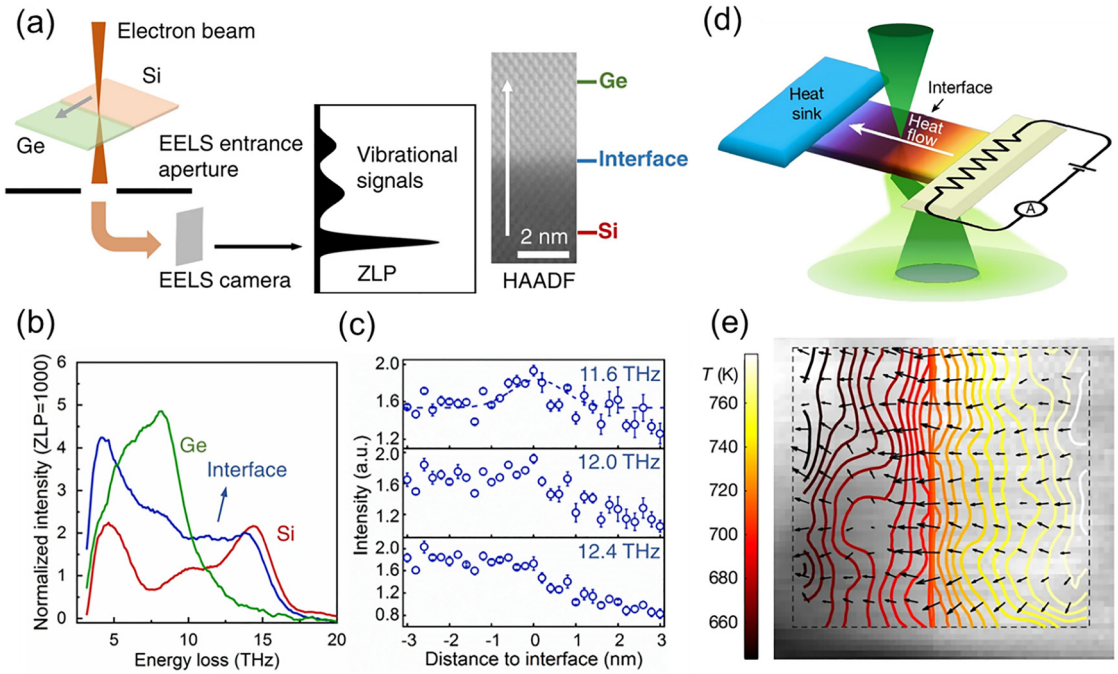


Fig. 10 (a) Schematic of STEM-EELS measurement at the Si/Ge interface. (b) The corresponding measured vibrational spectra of Si (red line), Ge (green line) and interface (blue line). (c) The spatial distribution of integrated vibrational signals at different frequencies (11.6, 12, and 12.4 THz)[48] Copyright @2021 Springer Nature. (d) Schematic diagram of the *in situ* heating STEM-EELS experimental setup for interface measurements. (e) The measured high-resolution nanoscale temperature distribution and the visualization of thermal transport directionality[227] Copyright @2025 Springer Nature.

V. Artificial intelligence for interfacial thermal transport

Artificial intelligence (AI) is emerging as the fourth paradigm of scientific research. It is primarily applied in two ways in the field of interfacial thermal transport. On the one hand, it can improve accuracy and efficiency compared to traditional numerical simulations (see Section III) through a data-driven implementation, such as using machine learning potentials in MD simulations. On the other hand, AI models trained on experimental data or first-principles calculations enable a rapid prediction of ITR. This further contributes to an efficient design of interfaces tailored to specific requirements. Here, we review the recent AI-driven developments on interfacial thermal transport from these two perspectives.

A. Machine learning potential based MD simulations

As discussed in Section III, numerous numerical methods have been developed to investigate thermal transport at interfaces. A key requirement for the accuracy of these methods is the determination of a precise descriptor, such as the interatomic interactions in MD or the potential energy surface for constructing the dynamical matrix in AGF. In classical MD simulations, interatomic interactions are typically described by empirical potentials, such as Tersoff[307] and Lennard-Jones[308] (LJ) potentials. These potentials are usually parameterized by fitting a fixed analytical functional form to the data from first-principles calculations or experimental measurements. While such explicit functional forms offer computational efficiency well suited to large-scale MD simulations, they often sacrifice accuracy.

Recently, machine learning potentials (MLPs) have emerged as a powerful tool for accurately capturing interatomic interactions, combining the accuracy of first-principles calculations with the computational efficiency of empirical potentials. Fig. 11 illustrates the procedure for constructing an MLP. The first step is to generate a concise and representative dataset. Many methods are employed to efficiently produce large ensembles of atomic-scale structures, including *ab initio* molecular dynamics (AIMD), empirical-potential-based molecular dynamics, random atomic displacements, strain application, and active learning schemes. Representative structures are then selected from these atomic configurations, either by comparing structural similarity through approaches such as latent space methods[309,310] and the regularized entropy match approach,[311] or by employing nonstandard neural network workflows such as random network distillation.[312] Using these selected structures, density functional theory (DFT) calculations are carried out to obtain accurate physical quantities, including the potential energy, atomic forces, and virial stress. The second step is to construct a high-quality MLP. To date, a variety of theoretical frameworks have been developed for this purpose,[313–332] all of which involve a set of specific hyperparameters. During training, these hyperparameters are tuned to enhance the accuracy and efficiency of the MLP to acceptable levels.[333,334] Once a reliable MLP has been obtained, it can be adopted in MLP-based molecular dynamics (ML–MD) simulations for further analysis.

 This journal is © the Owner Societies 2026

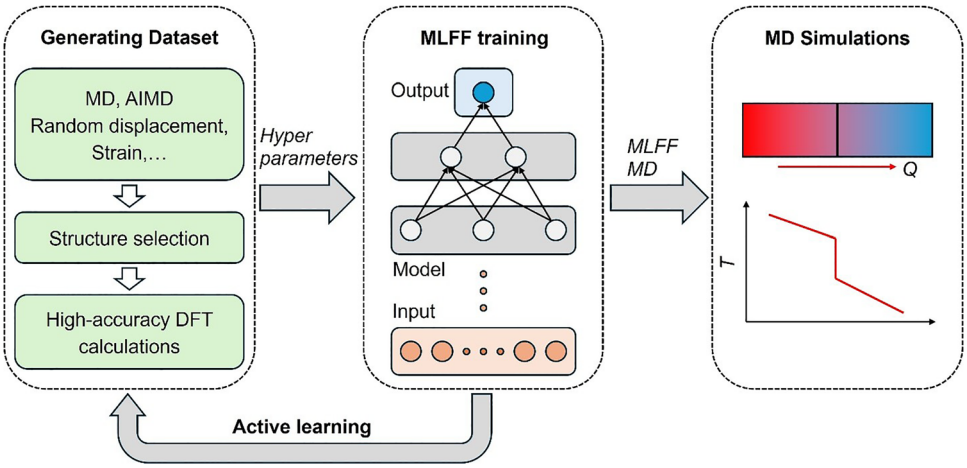


Fig. 11 The overview of ITC studies based on ML–MD.

ML–MD has demonstrated superior accuracy in studying interfacial thermal transport. For example, the ITC of the Si/diamond interface[335] and the AlN/Cu interface[336] calculated using ML–MD shows better agreement with measurements than those calculated by empirical-potential-based MD simulations. This indicates that the MLP captures a more reliable description of phonons at the interface. For instance, Cheng *et al.*[48] employed ML–MD to confirm the experimentally detected emergence of localized modes ($\sim$12 THz) at the high-quality epitaxial Si/Ge interface and demonstrated that these interfacial modes contribute approximately 5% to the ITC. Khot *et al.*[138] also identified interfacial modes at Al/Si interfaces and uncovered local phonon non-equilibrium in the phonon modes of Al and Si in the near-interface region. The resonance of interfacial modes is further found to increase the ITC at Si/Ge interfaces in nanowires[219] and GaN/diamond interfaces with carbon vacancies.[337] Using ML–MD, Yue *et al.*[338] revealed a transition in phonon transport from the ballistic to the diffusive regime at the graphene–silicon interface with increasing graphene thickness. Adnan *et al.*[339] further examined the thermal transport across metal (Al, Mo, Zr, Au)/diamond interfaces using the MLPs and found that the MLPs accurately captured both elastic and inelastic phonon transmission processes.

Furthermore, the MLP framework has also been extended to the exploration of thermal transport across more complex interfaces. By constructing an N–Ga–Al MLP, the ITC of GaN/AlN heterostructures was found to be dramatically affected by atomic interdiffusion and disorder[340] as well as elemental doping.[341] Sun *et al.* calculated the TBR of AlN/diamond[342] and β-Ga_2O_3/diamond[343] interfaces, revealing the influence of crystal orientations and bonded atom types at interfaces. They further investigated the effects of interlayer material, temperature, strain, and crystal orientation on the TBR of the Cu/diamond interface.[344]

In addition, the high fidelity of MLP-based MD makes it a natural bridge in multiscale thermal simulations. Mortazavi *et al.*[345] proposed a multiscale modeling framework combining DFT, MD, and FEM modeling without requiring prior thermal transport data. As shown in Fig. 12, they first performed AIMD simulations to generate data for training moment tensor potentials (MTP) of graphene/borophene systems. MD simulations were then carried out to calculate the thermal transport properties of the constituent materials and their interfaces. Using these properties as inputs, FEM was employed to compute the effective thermal conductivity of graphene/borophene heterostructures, with grain boundaries and composition considered. Wu *et al.*[346] adopted a similar procedure to investigate thermal transport in gallium nitride (GaN)-based devices, and found that the well-matched lattice vibrations between BAs and GaN led to an ultrahigh ITC of 260 MW m^{-2} K^{-1}. A competition between the grain size and the boundary resistance was also revealed. Sun *et al.*[347] simulated the thermal transport in β-Ga_2O_3-based heterointerfaces across multiple scales, and found that the TBR at the β-Ga_2O_3/diamond interface is higher than that at the β-Ga_2O_3/Si and β-Ga_2O_3/SiC interfaces. Nevertheless, multiscale simulations incorporating MLPs provide an effective bottom-up approach for the thermal management design of microelectronics.

Beyond studying the interfacial thermal transport at solid/solid interfaces, a few studies have investigated solid/liquid interfaces using MLP-based MD. Li *et al.*[348] constructed a Cu–water MLP and calculated the ITC of Cu/water interfaces. They obtained a value of $(2.505 \pm 0.335) \times 10^8$ W m^{-2} K^{-1}, which shows better agreement with experimental data than results based on empirical potentials. Liang *et al.*[349] modeled interfacial thermal transport at the SiO_2/molten LiCl–KCl interface based on MLP MD simulations, and investigated the influence of the near-surface microstructure of molten salt ions on the interfacial thermal transport.

B. Directly predicting ITC using AI tools

In addition to these AI-implemented atomistic simulations, AI models can be directly employed to predict the ITC at given interfaces by constructing descriptors related to interfacial properties. A proper descriptor determines the performance

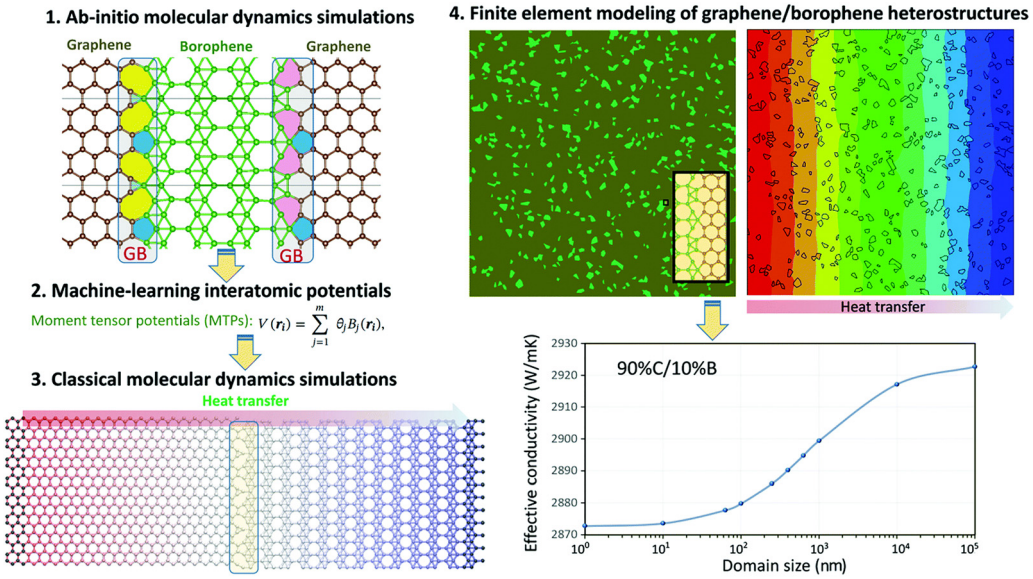


Fig. 12 Main steps of the proposed first-principles multiscale modeling framework to simulate the lattice thermal conductivity of graphene/borophene heterostructures from Mortazavi *et al.*[345] Copyright@2020 Royal Society of Chemistry.

of the corresponding AI model. Wang *et al.*[350] used the DMM to calculate the ITR and developed an AI-prediction model with crystal structure parameters and elemental properties as descriptors. Their results revealed that these descriptors associated with the energy, lattice constant, volume, and density of crystals should play a particularly important role in determining the ITR. Tian and Chen[351] applied machine learning methods, *e.g.*, decision trees and univariate testing, to select descriptors in the AI model for predicting ITR. They identified the five most important descriptors which were related to film thickness, specific heat capacities of the film and substrate, and the density of the substrate. Song *et al.*[352] further analysed the importance of 39 descriptors in the AI model for predicting ITR based on an experimental dataset[353,354] [Fig. 13(a)]. They demonstrated that the number of descriptors could be reduced to seven without compromising accuracy. Five of these seven descriptors are strongly correlated with the bonding strength, which is related to the vibrational properties of the two contacting parts.

With properly chosen descriptors, efficient AI models can be constructed and subsequently used to screen material datasets for pairs with a target ITR. For instance, Foss *et al.*[355] developed streamlined predictive models based on a dataset derived from 2D–3D Boltzmann mesoscale phonon simulations, enabling the optimal selection of 2D-substrate pairings to maximize the heat transfer. Al-Fahdi *et al.*[356] developed a reliable convolutional neural network (CNN) model [Fig. 13(b)] to identify promising substrates for cooling β-Ga_2O_3. Among the 32 716 candidate structures, YN and MgO ranked as the top two in terms of ITC when used as substrates for β-Ga_2O_3. Meanwhile, they further revealed a strong correlation between the ITC and the overlap of phonon VDOS [Fig. 13(c)]. Wu *et al.*[353,354,357] constructed ITR predictive models based on experimental data, focusing on high-ITR predictions. They identified Bi/Si as a promising heterostructure for thermoelectric applications, owing to the ultra-low thermal conductivity induced by its high ITR.

Furthermore, predictive models with interfacial features can be used to guide the design of interfaces between two materials. For example, Yang *et al.*[358] developed a prediction model for the ITR at the interface between graphene and hexagonal boron nitride (hBN), requiring knowledge of the system temperature, the coupling strength between the two layers, and the in-plane tensile strain. Rustam *et al.*[359] proposed a scalable Bayesian optimization framework that leverages the dynamic spawning of MD simulations to optimize the ITC at the Si/Al interface. As shown in Fig. 13(d) and (e), the introduction of a two-layer intermixed region rich in silicon yields a maximum ITC enhancement of 50%. Jin *et al.*[360] constructed prediction models based on MD data for Si/Ge heterostructures, offering distinct guidelines for ITC optimization through interfacial structural parameters (random nanostructuring/roughness density, height, and angle) and contact area. Ju *et al.*[85] developed a framework that combines the atomistic Green's function with Bayesian optimization to achieve the minimum ITC at the Si/Ge interface *via* nonintuitive interfacial structures. The resulting low ITC originates from a degree-of-freedom-induced balance between Fabry–Pérot wave interference and interfacial particle scattering in aperiodic structures. Guo *et al.*[361] implemented a novel deep learning (DL) encoder–decoder CNN coupled with MD simulations to investigate thermal transport across solid/liquid interfaces. Their approach maps the temperature distribution across the computational domain based on the solid–liquid interface geometry obtained from MD, offering a promising tool for designing the solid/liquid interfaces with targeted ITC.

While AI has significantly advanced research on interfacial thermal transport, numerous challenges remain. For ML–MD,

 This journal is © the Owner Societies 2026

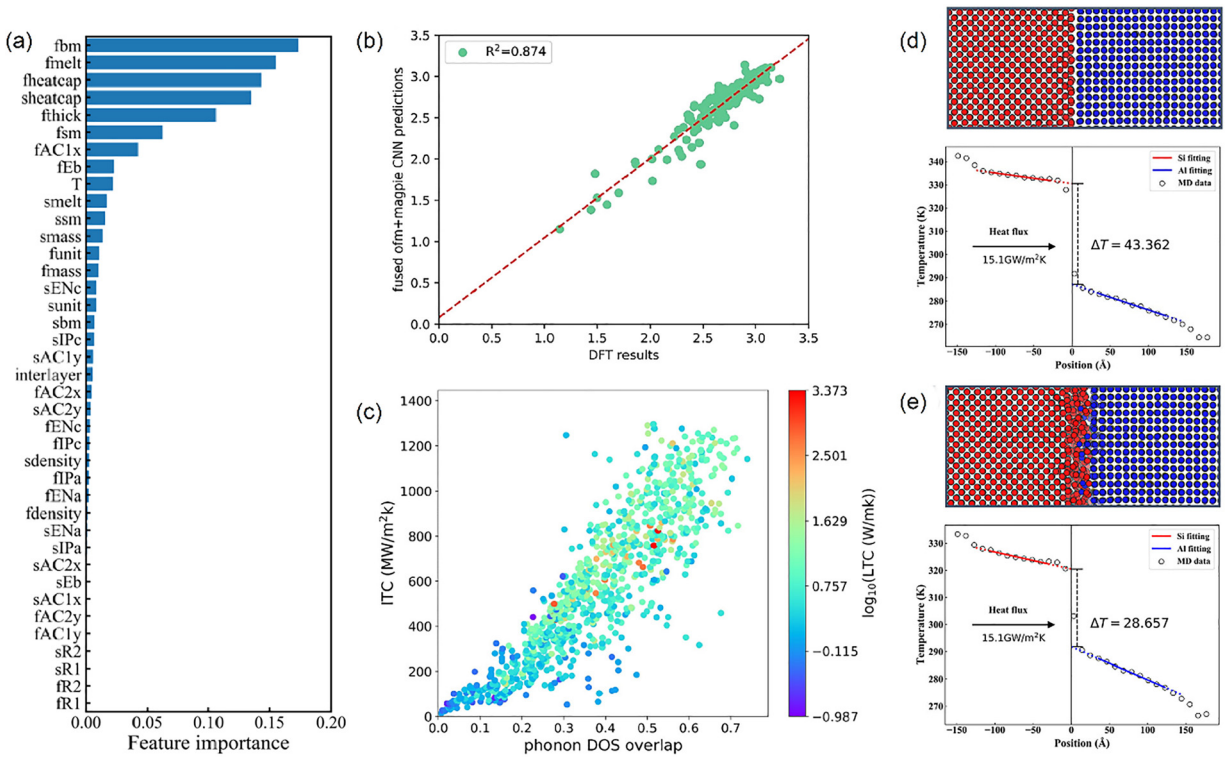


Fig. 13 (a) Feature importance ranking for 39 descriptors from Song *et al.*[352] Copyright@2025 American Institute of Physics. (b) Comparison of ITC between DFT-ITC results and the CNN predictions and (c) dependence of ITC on phonon DOS overlap from Al-Fahdi[356] Copyright@2024 American Institute of Physics. (d) Temperature profiles of perfect interface and (e) that of the mixed interface from Rustam *et al.*[359] Copyright@2022 American Chemical Society.

most efforts have focused on simple interfaces composed of structurally simple materials. However, many interfaces are much more complex in practical applications. For instance, surface modification with large organic molecules is a popular strategy for enhancing ITC at solid/liquid interfaces, resulting in a complex interface that combines a disordered liquid phase, large molecules, and ordered/disordered solids. Generating an accurate MLP for such an interface is both difficult and computationally expensive. It is therefore essential to develop strategies for efficiently training MLPs for complex systems. One potential solution lies in devising a coupling scheme that bridges two independent MLPs, each describing one part of the overall system. Such an approach would take advantage of the wide array of MLPs already trained on simple systems.

For AI-based predictions, one major challenge lies in acquiring large volumes of accurate data, which are typically generated through experiments, DFT-based empirical models, and MD simulations. However, experimental data depend heavily on sample quality, while DFT-based empirical models (*e.g.*, DMM and AGF) are constrained by their approximations. MD simulations are limited by the accuracy of interfacial potentials and become computationally prohibitive when MLPs must be trained for a vast range of materials. A possible solution is to develop AI models guided by the underlying physical principles of interfacial thermal transport, as incorporating such principles enables the construction of accurate models with substantially less data.

VI. Perspectives and future challenges

Recent computational and experimental advances have shifted the understanding of interfacial thermal transport from a scalar ITC or ITR picture to a mechanism-resolved picture, *e.g.*, spectral and modal level phonon transmission. On the one hand, analytical models such as AMM and DMM provide useful limiting cases for specular and diffuse phonon transmission, while AGF/NEGF and MD simulations reveal how specific interfacial features, including mass grading, roughness, interdiffusion, anharmonicity, localized interfacial modes, and solid/liquid molecular ordering, selectively modify different spectral heat-carrying channels. On the other hand, measurements such as TDTR and FDTR provide reliable integrated ITC values and identify trends associated with bonding strength, elastic mismatch, surface chemistry, and molecular adsorption, whereas advanced spectroscopic techniques such as STEM-EELS directly visualize localized interfacial vibrations and nanoscale temperature fields. These results collectively show that interfacial heat transfer is governed by the selective transmission, reflection, and conversion of phonons across frequency, mode, momentum, and spatial scales. Furthermore,

these understandings provide practical guidance for interface optimization. For instance, to enhance ITC, interfacial structures can be engineered to improve spectral matching, strengthen interfacial bonding, introduce graded transition layers, or use molecular bridges to activate otherwise weakly transmitting modes. Conversely, to suppress ITC, one can introduce vibrational mismatch, disorder, roughness, or interfacial architectures that block dominant heat-carrying channels. Although these strategies do not provide a universal recipe for modulating ITC in every system, they offer general principles and useful starting points for rational interface design.

A. Bridging the gap between simulation and experiment

Despite the remarkable progress that has been made in recent decades, a persistent gap remains between computational modelling and experimental characterization of interfacial thermal transport. On the simulation side, atomistic methods such as AGF and MD provide detailed spectral information, including mode-resolved transmission coefficients, inelastic scattering contributions, and the role of interfacial microstructure, while these results are inherently limited by their approximations. AGF relies on the accuracy of interatomic force constants, and the computational cost for a complex interface becomes extremely large. MD simulations depend critically on the fidelity of interatomic potentials, where empirical potentials often introduce quantitative inaccuracies, while machine learning potentials remain computationally expensive to train. Furthermore, MD simulations are restricted to nanoscale systems and follow classical statistics, leading to overestimated phonon populations at low temperatures. Mesoscale BTE solvers extend the accessible length scale but simplify the interface as a boundary condition described by analytical models such as the DMM, thereby neglecting interfacial microstructural details, localized modes, and wave-like phonon effects in the near-interface region.

On the experimental side, FDTR and TDTR provide highly accurate measurements of the overall ITC but yield limited spectral information without additional modelling. The extracted ITC represents a frequency-integrated quantity, making it difficult to directly validate the spectral predictions from simulations. Recent efforts have begun to connect this gap. For instance, Hua *et al.*[43] combined TDTR measurements at multiple modulation frequencies with BTE simulations to extract frequency-dependent phonon transmission coefficients at Al/Si interfaces, revealing discrepancies with DMM predictions at low frequencies. Similarly, Chen *et al.*[306] coupled machine learning with ultrafast electron diffraction to reconstruct frequency-resolved relaxation times and transmission coefficients at Au/Si interfaces, again demonstrating deviations from the predictions of DMM. Furthermore, machine learning potentials have significantly improved the agreement between MD-predicted ITC values and experimental measurements for systems such as Si/diamond[335] and the AlN/Cu[336] interfaces.

Nevertheless, systematic and quantitative benchmarking between simulation and experiment remains scarce. Experimental measurements are expected to provide spectral and mode-resolved information that can be directly compared with atomistic predictions, while simulations must incorporate realistic interfacial conditions including disorder, roughness, interdiffusion, and multi-carrier effects at length scales accessible to measurement. The multiscale simulation framework, in which machine learning potentials feed into mesoscale BTE solvers with physically informed boundary conditions derived from AGF or NEGF calculations, represents a promising pathway toward this goal. Meanwhile, it is important to develop a standardized benchmark system, *i.e.*, a well-characterized interface with known atomic structure, composition, and interfacial bonds. Such benchmark systems enable both high-fidelity simulations and precise experiments to be performed and directly compared. Only through such synergistic integration can the field move from qualitative understanding to truly predictive design of interfacial thermal transport.

B. Interfacial thermal transport under extreme conditions

Most studies of interfacial thermal transport, including both computational and experimental investigations, have been conducted under ambient or near-ambient conditions. However, many technologically important applications require interfaces to function under extreme environments where the thermal transport physics may differ substantially from the well-studied ambient regime.

At elevated temperatures, anharmonic phonon–phonon interactions become increasingly significant. As demonstrated by NEGF calculations at Si/Ge interfaces,[89] the contribution of inelastic scattering to ITC grows from approximately 10% at room temperature to 20% at 600 K, and MD simulations suggest even larger enhancements when full-order inelastic processes are considered.[124,135] At sufficiently high temperatures, higher-order scattering processes (*i.e.*, four-phonon and beyond), phonon renormalization, and structural instabilities at interfaces may qualitatively alter the transport picture. Yet computational tools that can capture these effects remain limited: AGF with four-phonon scattering is computationally prohibitive,[87,89] while MD simulations at high temperatures face challenges related to potential stability and the breakdown of the quasi-harmonic framework used for quantum corrections. Experimentally, TDTR and FDTR measurements at high temperatures are complicated by transducer degradation, interdiffusion at the interface, and thermal radiation backgrounds. Likewise, under high pressure conditions, the interfacial thermal transport can be profoundly modified. Li and Qiu[166] demonstrated a nonmonotonic pressure dependence of ITC at metal/water interfaces, where the interplay between molecular filling, vibrational overlap, and equilibrium bond-length compression produces competing effects. For solid/solid interfaces, pressure can modify the interfacial contact area, bonding strength, and phonon spectra of the constituent materials simultaneously. Systematic studies correlating pressure-dependent ITC with spectral phonon properties remain lacking.

In addition, interfaces exposed to radiation, which are relevant to nuclear energy systems, space electronics, and ion-beam-processed semiconductor devices, present another frontier.

 This journal is © the Owner Societies 2026

Radiation can introduce point defects, amorphous layers, and compositional mixing at interfaces, all of which modify the phonon transmission spectrum. While MD simulations can model radiation-damaged interfaces, the lack of validated interatomic potentials for defect-rich interfacial regions and the absence of systematic experimental measurements of ITC in irradiated systems limit current understanding.

In general, addressing interfacial thermal transport under extreme conditions requires advances on multiple fronts, including the development of interatomic potentials (particularly machine learning potentials) trained on high-temperature and high-pressure configurations, the extension of experimental platforms to operate reliably under extreme conditions, and the formulation of theoretical frameworks that can capture the interplay between anharmonicity, defects, and structural evolution at interfaces far from equilibrium.

C. Interfacial thermal transport in next-generation technologies

The fundamental understanding developed in the preceding sections must ultimately serve the practical imperative of thermal management. As device architectures evolve toward unprecedented power densities and heterogeneous material integration, interfacial thermal resistance is rapidly transitioning from a secondary concern to the dominant thermal bottleneck in next-generation technologies. For instance, GaN and Ga_2O_3-based power devices generate localized heat fluxes exceeding 1 kW cm^{-2}, making near-junction thermal management the primary performance limiter.[195] In GaN-on-diamond heterostructures, the ITC at the GaN/diamond boundary governs effective heat extraction. Spectral analyses reveal that mid-frequency phonons (2–8 THz) dominate the interfacial heat flux but are severely hindered by amorphous interlayers and lattice mismatch. Looking forward, rational interface engineering guided by spectral design principles and ML-accelerated screening of interlayer compositions will be essential for realizing diamond's thermal potential in next-generation RF and power devices.

At the package level, TIM performance is governed not only by fillers' conductivity but critically by thermal resistances at multiple filler–matrix and filler–substrate contacts. MD studies have shown that surface functionalization with SAMs can enhance solid/liquid ITC by nearly an order of magnitude through collaborative wettability and vibrational coupling effects, preferentially boosting low-frequency (0–4 THz) phonon transmission.[163,191] This spectral insight provides a design principle, *i.e.*, molecular bridges should be engineered to match the dominant spectral contributions at each specific contact, enabling spectrally tailored interlayers that bridge the vibrational mismatch between dissimilar materials.

Furthermore, direct liquid cooling for high-performance computing places renewed emphasis on solid/liquid interfacial transport. The sensitivity of ITC to molecular-level structure of the first adsorbed layer and its vibrational coupling to the substrate, including nonmonotonic pressure dependence observed at metal/water interfaces, highlights the delicate optimization required. In batteries, thermal resistance at electrode/electrolyte/collector interfaces governs temperature uniformity and safety margins. Unlike static semiconductor interfaces, battery interfaces evolve during cycling through degradation and interphase growth. Understanding how ITC co-evolves with electrochemical aging, potentially through MLP-based MD simulations on interfaces at various degradation states, represents an emerging frontier bridging thermal physics with electrochemistry.

Across all these domains, translating fundamental understanding into engineering practice requires confronting the gap between idealized simulated interfaces and the complex, imperfect interfaces in real devices, featuring roughness, residual stresses, oxide layers, and processing defects that are expected to modify ITC by factors of two to ten. The multiscale pipeline combining ML–MD, AGF, and mesoscale BTE solvers provides the computational infrastructure for this translation. When coupled with AI-driven optimization, this pipeline can transform interfacial thermal engineering from empirical art into predictive design, ultimately enabling thermal-aware device workflows where interfacial properties are predicted and optimized with the same confidence currently afforded to electrical performance.

VII. Summary

In this review, we provided an examination of thermal transport across material interfaces from the perspective of spectral phonon physics, bridging fundamental theory, computational methodology, experimental characterization, and data-driven approaches. The central thesis throughout is that interfacial thermal transport is inherently a spectral phenomenon, *i.e.*, the mismatch in vibrational density of states between dissimilar materials acts as a frequency-dependent filter that selectively transmits, reflects, or scatters phonons across the boundary. Understanding and manipulating this spectral selectivity is the key to engineering interfaces with targeted thermal properties.

We began by establishing the theoretical foundations through AMM and DMM, which provide complementary physical pictures of phonon transmission at idealized interfaces. While these analytical models capture essential physics, they neglect critical features of real interfaces, motivating the development of more sophisticated computational approaches. The AGF method offers rigorous, frequency-resolved transmission calculations within the harmonic and weakly anharmonic regimes, while MD simulations, equipped with spectral decomposition techniques such as FDDDM, SHC, and TDDDM, naturally incorporate full anharmonicity and enable the study of complex interfacial geometries including rough, nanostructured, and solid/liquid boundaries. The extension to mesoscale BTE solvers bridges the gap between atomistic physics and device-scale thermal predictions, though the treatment of interfaces within these frameworks remains simplified.

On the experimental front, FDTR and TDTR techniques have matured into powerful tools for measuring interfacial thermal conductance with high precision. Recent innovations,

including BOFDTR for probing ballistic-to-diffusive transitions, beam-offset and asymmetric-beam configurations for anisotropic transport, and coupling with BTE fitting for extracting spectral transmission, are beginning to provide the frequency-resolved experimental data needed to validate atomistic predictions. Meanwhile, STEM-EELS has enabled the direct visualization of interfacial phonon modes at the atomic scale, offering unprecedented spatial resolution of vibrational properties at buried interfaces.

At the same time, the emergence of artificial intelligence has introduced transformative capabilities to this field. Machine learning potentials combine near-first-principles accuracy with the computational efficiency required for large-scale MD simulations of realistic interfaces, yielding ITC values in significantly better agreement with experiments than those obtained from empirical potentials. Data-driven predictive models, trained on carefully selected descriptors derived from material properties, enable rapid screening of material combinations for targeted interfacial thermal resistance, accelerating the discovery and optimization cycle.

Despite this substantial progress, several critical challenges remain. The gap between idealized simulated interfaces and the complex, imperfect interfaces encountered in real devices continues to hinder quantitative prediction. Systematic benchmarking between simulations and experiments on well-characterized reference systems is urgently needed. In addition, the behavior of interfaces under extreme conditions of temperature, pressure, and radiation remains poorly understood. Furthermore, the translation of spectral design principles into practical thermal management solutions for next-generation electronics, power devices, and energy systems requires a truly multiscale framework that seamlessly connects atomistic physics to device-level performance.

Looking forward, the convergence of machine learning potentials, mesoscale solvers with physically informed boundary conditions, and advanced experimental techniques capable of extracting spectral information promises to transform interfacial thermal engineering from an empirical endeavor into a predictive science. By establishing the quantitative relationship between interfacial atomic structure and frequency-dependent phonon transmission, and by leveraging AI to navigate the vast design space of possible interfacial configurations, the community is poised to achieve rational design of interfaces with prescribed thermal functionalities, addressing one of the most pressing bottlenecks in modern thermal management.

Conflicts of interest

There are no conflicts to declare.

Data availability

Data sharing not applicable—no new data was generated or analysed in this study.

Acknowledgements

Y. Zhou acknowledges the startup fund (Grant No. REC20EGR14, a/c-R9246), the Frontier Technology Research for Joint Institutes with Industry Scheme (Grant No. FTRIS-002) and the Sustainable and Smart Campus as a Living Lab (Grant No. F2224) from Hong Kong University of Science and Technology (HKUST). Y. Zhou thanks the Research Grants Council of the Hong Kong Special Administrative Region under Grant C6020-22G, 16209526, 26206023, 16207124, C6002-25Y and C7002-22Y, the fund from the Guangdong Natural Science Foundation under Grant No. 2024A1515011407. Y. Zhou also thanks the Hong Kong SciTech Pioneers Award from the Y-LOT foundation. We thank HKUST Fok Ying Tung Research Institute and National Supercomputing Center in Guangzhou Nansha Sub-center for computational resources.

References

1 P. Ball, Computer engineering: Feeling the heat, *Nature*, 2012, **492**, 174–176.
2 A. L. Moore and L. Shi, Emerging challenges and materials for thermal management of electronics, *Mater. Today*, 2014, **17**, 163–174.
3 Z. Wu and Z. Wang, Cooling next-generation electronics: From emerging semiconductors to data centers, *Innov. Energy*, 2025, **2**, 100125.
4 G. E. Moore, Cramming More Components Onto Integrated Circuits, *Proc. IEEE*, 1998, **86**, 82–85.
5 S. Krishnan, S. V. Garimella, G. M. Chrysler and R. V. Mahajan, Towards a Thermal Moore's Law, *IEEE Trans. Adv. Packag.*, 2007, **30**, 462–474.
6 A. Bar-Cohen, *2009 IEEE International Conference on Microwaves, Communications, Antennas and Electronics Systems*, 2009, pp. 1–8.
7 S. Adera, D. Antao, R. Raj and E. N. Wang, *2016 15th IEEE Intersociety Conference on Thermal and Thermomechanical Phenomena in Electronic Systems (ITherm)*, 2016, pp. 364–371.
8 R. W. van Gils, D. Danilov, P. H. L. Notten, M. F. M. Speetjens and H. Nijmeijer, Battery thermal management by boiling heat-transfer, *Energy Convers. Manage.*, 2014, **79**, 9–17.
9 L. Li, J. Yang, R. Tan, W. Shu, C. J. Low, Z. Zhang, Y. Zhao, C. Li, Y. Zhang, X. Li, H. Zhang, X. Zhao, Z. Kou, Y. Xiao, F. Verpoort, H. Wang, L. Mai and D. He, Large-scale current collectors for regulating heat transfer and enhancing battery safety, *Nat. Chem. Eng.*, 2024, **1**, 542–551.
10 K. M. Razeeb, E. Dalton, G. L. W. Cross and A. J. Robinson, Present and future thermal interface materials for electronic devices, *Int. Mater. Rev.*, 2018, **63**, 1–21.
11 E. T. Swartz and R. O. Pohl, Thermal resistance at interfaces, *Appl. Phys. Lett.*, 1987, **51**, 2200–2202.
12 M. Grujicic, C. L. Zhao and E. C. Dusel, The effect of thermal contact resistance on heat management in the electronic packaging, *Appl. Surf. Sci.*, 2005, **246**, 290–302.

 This journal is © the Owner Societies 2026

13 Y. Xia, Y. Sheng, R. Jia, J. Xu and H. Bao, Non-Fourier thermal analysis of the self-heating effect in CMOS logic circuits, *APL Electron. Devices*, 2025, **1**, 036115.
14 G. Chen, Non-Fourier phonon heat conduction at the microscale and nanoscale, *Nat. Rev. Phys.*, 2021, **3**, 555–569.
15 P. L. Kapitza, Heat Transfer and Superfluidity of Helium II, *Phys. Rev.*, 1941, **60**, 354–355.
16 J. Chen, X. Xu, J. Zhou and B. Li, Interfacial thermal resistance: Past, present, and future, *Rev. Mod. Phys.*, 2022, **94**, 025002.
17 G. L. Pollack, Kapitza Resistance, *Rev. Mod. Phys.*, 1969, **41**, 48–81.
18 B. Chatterjee, K. Zeng, C. D. Nordquist, U. Singisetti and S. Choi, Device-Level Thermal Management of Gallium Oxide Field-Effect Transistors, *IEEE Trans. Compon., Packag., Manuf. Technol.*, 2019, **9**, 2352–2365.
19 J. H. Lau and T. G. Yue, *2009 59th Electronic Components and Technology Conference*, 2009, pp. 635–640.
20 J. Due and A. J. Robinson, Reliability of thermal interface materials: A review, *Appl. Therm. Eng.*, 2013, **50**, 455–463.
21 E. T. Swartz and R. O. Pohl, Thermal boundary resistance, *Rev. Mod. Phys.*, 1989, **61**, 605–668.
22 P. Reddy, K. Castelino and A. Majumdar, Diffuse mismatch model of thermal boundary conductance using exact phonon dispersion, *Appl. Phys. Lett.*, 2005, **87**, 211908.
23 S. Sadasivam, U. V. Waghmare and T. S. Fisher, Phonon-eigenspectrum-based formulation of the atomistic Green's function method, *Phys. Rev. B*, 2017, **96**, 174302.
24 Z. Zong, X. Chen, B. Yan, Y. Xie, J. Pang, G. Li, J. Hu, Z. Wu, B. Li, H. Fang and N. Yang, Theoretical Models on Interfacial Thermal Conductance of Nanoscale Solid Interfaces in Chips: A Mini Review, *Chin. Phys. Lett.*, 2024, **41**, 106301.
25 Y.-X. Xu, H.-Z. Fan and Y.-G. Zhou, Quantifying spectral thermal transport properties in framework of molecular dynamics simulations: a comprehensive review, *Rare Met.*, 2023, **42**, 3914–3944.
26 S. Mazumder, Boltzmann transport equation based modeling of phonon heat conduction: progress and challenges, *Annu. Rev. Heat Transfer*, 2021, **24**, 71–130.
27 H. Bao, J. Chen, X. Gu and B. Cao, A Review of Simulation Methods in Micro/Nanoscale Heat Conduction, *ES Energy Environ.*, 2018, **1**, 16–55.
28 D. G. Cahill, W. K. Ford, K. E. Goodson, G. D. Mahan, A. Majumdar, H. J. Maris, R. Merlin and S. R. Phillpot, Nanoscale thermal transport, *J. Appl. Phys.*, 2003, **93**, 793–818.
29 D. G. Cahill, P. V. Braun, G. Chen, D. R. Clarke, S. Fan, K. E. Goodson, P. Keblinski, W. P. King, G. D. Mahan, A. Majumdar, H. J. Maris, S. R. Phillpot, E. Pop and L. Shi, Nanoscale thermal transport. II. 2003–2012, *Appl. Phys. Rev.*, 2014, **1**, 011305.
30 A. Giri and P. E. Hopkins, A Review of Experimental and Computational Advances in Thermal Boundary Conductance and Nanoscale Thermal Transport across Solid Interfaces, *Adv. Funct. Mater.*, 2020, **30**, 1903857.
31 T. Feng, H. Zhou, Z. Cheng, L. S. Larkin and M. R. Neupane, A Critical Review of Thermal Boundary Conductance across Wide and Ultrawide Bandgap Semiconductor Interfaces, *ACS Appl. Mater. Interfaces*, 2023, **15**, 29655–29673.
32 R. Mao, P. He, F. Liu, R. Shi, J. Du and P. Gao, Electron Microscopy for Nanophononics: A Review, *ACS Nano*, 2025, **19**, 20269–20294.
33 Z. Xu, R. Mao and P. Gao, Atomic-Scale Interface Phonon Engineering for Thermal Management: An Electron Microscopy Review, *Adv. Funct. Mater.*, 2026, **36**, e26614.
34 J. B. J. Fourier and G. Darboux, *Théorie analytique de la chaleur*, Didot Paris, 1822, vol. 504.
35 S. D. Poisson, *Théorie mathématique de la chaleur*, Bachelier, 1835.
36 W. A. Little, The transport of heat between dissimilar solids at low temperatures, *Can. J. Phys.*, 1959, **37**, 334–349.
37 R. Prasher, Acoustic mismatch model for thermal contact resistance of van der Waals contacts, *Appl. Phys. Lett.*, 2009, **94**, 041905.
38 R. S. Prasher and P. E. Phelan, A Scattering-Mediated Acoustic Mismatch Model for the Prediction of Thermal Boundary Resistance, *J. Heat Transfer*, 2000, **123**, 105–112.
39 J. C. Duda, T. E. Beechem, J. L. Smoyer, P. M. Norris and P. E. Hopkins, Role of dispersion on phononic thermal boundary conductance, *J. Appl. Phys.*, 2010, **108**, 073515.
40 P. E. Hopkins and P. M. Norris, Relative Contributions of Inelastic and Elastic Diffuse Phonon Scattering to Thermal Boundary Conductance Across Solid Interfaces, *J. Heat Transfer*, 2009, **131**, 022402.
41 P. E. Hopkins, Multiple phonon processes contributing to inelastic scattering during thermal boundary conductance at solid interfaces, *J. Appl. Phys.*, 2009, **106**, 013528.
42 P. E. Hopkins, T. Beechem, J. C. Duda, K. Hattar, J. F. Ihlefeld, M. A. Rodriguez and E. S. Piekos, Influence of anisotropy on thermal boundary conductance at solid interfaces, *Phys. Rev. B: Condens. Matter Mater. Phys.*, 2011, **84**, 125408.
43 C. Hua, X. Chen, N. K. Ravichandran and A. J. Minnich, Experimental metrology to obtain thermal phonon transmission coefficients at solid interfaces, *Phys. Rev. B*, 2017, **95**, 205423.
44 Y. Zhang, D. Ma, Y. Zang, X. Wang and N. Yang, A Modified Theoretical Model to Accurately Account for Interfacial Roughness in Predicting the Interfacial Thermal Conductance, *Front. Energy Res.*, 2018, **6**, 48.
45 S. Wang, Z. Jiang, L. Ren, X. Zeng and R. Sun, Interface deciphering for highly interfacial adhesion and efficient heat energy transfer, *Appl. Phys. Lett.*, 2023, **123**, 153506.
46 X. Cheng, D. He, M. Zhou, P. Zhang, S. Wang, L. Ren, R. Sun and X. Zeng, Can Adhesion Energy Optimize Interface Thermal Resistance at a Soft/Hard Material Interface ?, *Nano Lett.*, 2023, **23**, 6673–6680.
47 B. K. Rao and P. Jena, Molecular view of the interfacial adhesion in aluminum-silicon carbide metal-matrix composites, *Appl. Phys. Lett.*, 1990, **57**, 2308–2310.

48 Z. Cheng, R. Li, X. Yan, G. Jernigan, J. Shi, M. E. Liao, N. J. Hines, C. A. Gadre, J. C. Idrobo, E. Lee, K. D. Hobart, M. S. Goorsky, X. Pan, T. Luo and S. Graham, Experimental observation of localized interfacial phonon modes, *Nat. Commun.*, 2021, **12**, 6901.

49 K. Gordiz and A. Henry, Phonon Transport at Crystalline Si/Ge Interfaces: The Role of Interfacial Modes of Vibration, *Sci. Rep.*, 2016, **6**, 23139.

50 S. Shan, Z. Zhang, S. Volz and J. Chen, Phonon mode at interface and its impact on interfacial thermal transport, *J. Phys.: Condens. Matter*, 2024, **36**, 423001.

51 S. Shan, Z. Zhang, S. Lu, S. Volz and J. Chen, Generation of interfacial phonon modes and their contribution to thermal transport across the GaN/ZnO interface, *Phys. Rev. B*, 2025, **112**, 155302.

52 G. T. Hohensee, R. B. Wilson and D. G. Cahill, Thermal conductance of metal–diamond interfaces at high pressure, *Nat. Commun.*, 2015, **6**, 6578.

53 Q. Li, F. Liu, S. Hu, H. Song, S. Yang, H. Jiang, T. Wang, Y. K. Koh, C. Zhao, F. Kang, J. Wu, X. Gu, B. Sun and X. Wang, Inelastic phonon transport across atomically sharp metal/semiconductor interfaces, *Nat. Commun.*, 2022, **13**, 4901.

54 K. Sääskilahti, J. Oksanen, J. Tulkki and S. Volz, Role of anharmonic phonon scattering in the spectrally decomposed thermal conductance at planar interfaces, *Phys. Rev. B: Condens. Matter Mater. Phys.*, 2014, **90**, 134312.

55 Z. Tian, K. Esfarjani and G. Chen, Enhancing phonon transmission across a Si/Ge interface by atomic roughness: First-principles study with the Green's function method, *Phys. Rev. B: Condens. Matter Mater. Phys.*, 2012, **86**, 235304.

56 S. Merabia and K. Termentzidis, Thermal boundary conductance across rough interfaces probed by molecular dynamics, *Phys. Rev. B: Condens. Matter Mater. Phys.*, 2014, **89**, 054309.

57 C. Shao, Q. Rong, M. Hu and H. Bao, Probing phonon–surface interaction by wave-packet simulation: Effect of roughness and morphology, *J. Appl. Phys.*, 2017, **122**, 155104.

58 P. E. Hopkins, L. M. Phinney, J. R. Serrano and T. E. Beechem, Effects of surface roughness and oxide layer on the thermal boundary conductance at aluminum/silicon interfaces, *Phys. Rev. B: Condens. Matter Mater. Phys.*, 2010, **82**, 085307.

59 E. Lee, T. Zhang, M. Hu and T. Luo, Thermal boundary conductance enhancement using experimentally achievable nanostructured interfaces – analytical study combined with molecular dynamics simulation, *Phys. Chem. Chem. Phys.*, 2016, **18**, 16794–16801.

60 E. Lee, T. Zhang, T. Yoo, Z. Guo and T. Luo, Nanostructures Significantly Enhance Thermal Transport across Solid Interfaces, *ACS Appl. Mater. Interfaces*, 2016, **8**, 35505–35512.

61 Y. Xu, G. Wang and Y. Zhou, Broadly manipulating the interfacial thermal energy transport across the Si/4H-SiC interfaces *via* nanopatterns, *Int. J. Heat Mass Transfer*, 2022, **187**, 122499.

62 J.-S. Wang, J. Wang and N. Zeng, Nonequilibrium Green's function approach to mesoscopic thermal transport, *Phys. Rev. B: Condens. Matter Mater. Phys.*, 2006, **74**, 033408.

63 W. Zhang, T. S. Fisher and N. Mingo, The Atomistic Green's Function Method: An Efficient Simulation Approach for Nanoscale Phonon Transport, *Numer. Heat Transfer, Part B*, 2007, **51**, 333–349.

64 N. Mingo, Anharmonic phonon flow through molecular-sized junctions, *Phys. Rev. B: Condens. Matter Mater. Phys.*, 2006, **74**, 125402.

65 N. Mingo and L. Yang, Phonon transport in nanowires coated with an amorphous material: An atomistic Green's function approach, *Phys. Rev. B: Condens. Matter Mater. Phys.*, 2003, **68**, 245406.

66 J.-S. Wang, J. Wang and J. T. Lü, Quantum thermal transport in nanostructures, *Eur. Phys. J. B*, 2008, **62**, 381–404.

67 R. E. Peierls, *Quantum Theory of Solids*, Clarendon Press, 1955.

68 G. P. Srivastava, *The Physics of Phonons*, CRC Press, 1990.

69 J. M. Ziman, *Electrons and Phonons: The Theory of Transport Phenomena in Solids*, Oxford University Press, Oxford, 2001.

70 G. Chen, Nanoscale Energy Transport and Conversion: A Parallel Treatment of Electrons, *Molecules, Phonons, and Photons*, Oxford University Press, 2005.

71 J.-S. Wang, B. K. Agarwalla, H. Li and J. Thingna, Nonequilibrium Green's function method for quantum thermal transport, *Front. Phys.*, 2014, **9**, 673–697.

72 R. Landauer, Electrical transport in open and closed systems, *Z. Phys. B: Condens. Matter*, 1987, **68**, 217–228.

73 B. Latour, N. Shulumba and A. J. Minnich, *Ab initio* study of mode-resolved phonon transmission at Si/Ge interfaces using atomistic Green's functions, *Phys. Rev. B*, 2017, **96**, 104310.

74 Z.-Y. Ong and G. Zhang, Efficient approach for modeling phonon transmission probability in nanoscale interfacial thermal transport, *Phys. Rev. B: Condens. Matter Mater. Phys.*, 2015, **91**, 174302.

75 Z.-Y. Ong, G. Zhang and Y.-W. Zhang, Controlling the thermal conductance of graphene/h-BN lateral interface with strain and structure engineering, *Phys. Rev. B*, 2016, **93**, 075406.

76 Z.-Y. Ong, Atomistic S-matrix method for numerical simulation of phonon reflection, transmission, and boundary scattering, *Phys. Rev. B*, 2018, **98**, 195301.

77 S. Sadasivam, N. Ye, J. P. Feser, J. Charles, K. Miao, T. Kubis and T. S. Fisher, Thermal transport across metal silicide-silicon interfaces: First-principles calculations and Green's function transport simulations, *Phys. Rev. B*, 2017, **95**, 085310.

78 L. Lindsay and D. A. Broido, Optimized Tersoff and Brenner empirical potential parameters for lattice dynamics and phonon thermal transport in carbon nanotubes and graphene, *Phys. Rev. B: Condens. Matter Mater. Phys.*, 2010, **81**, 205441.

79 H. Zhao and J. B. Freund, Phonon scattering at a rough interface between two fcc lattices, *J. Appl. Phys.*, 2009, **105**, 013515.

 This journal is © the Owner Societies 2026

80 X. Gu, X. Li and R. Yang, Phonon transmission across $Mg_2Si/Mg_2Si_{1-x}Sn_x$ interfaces: A first-principles-based atomistic Green's function study, *Phys. Rev. B: Condens. Matter Mater. Phys.*, 2015, **91**, 205313.

81 C. Li and Z. Tian, Phonon Transmission Across Silicon Grain Boundaries by Atomistic Green's Function Method, *Front. Phys.*, 2019, **7**, 3.

82 L. Yang, B. Yang and B. Li, Enhancing interfacial thermal conductance of an amorphous interface by optimizing the interfacial mass distribution, *Phys. Rev. B*, 2023, **108**, 165303.

83 L. Yang, B. Latour and A. J. Minnich, Phonon transmission at crystalline-amorphous interfaces studied using mode-resolved atomistic Green's functions, *Phys. Rev. B*, 2018, **97**, 205306.

84 L. Yang, X. Wan, D. Ma, Y. Jiang and N. Yang, Maximization and minimization of interfacial thermal conductance by modulating the mass distribution of the interlayer, *Phys. Rev. B*, 2021, **103**, 155305.

85 S. Ju, T. Shiga, L. Feng, Z. Hou, K. Tsuda and J. Shiomi, Designing Nanostructures for Phonon Transport *via* Bayesian Optimization, *Phys. Rev. X*, 2017, **7**, 021024.

86 S. Ju and X. Liang, Detecting the phonon interference effect in Si/Ge nanocomposite by wave packets, *Appl. Phys. Lett.*, 2015, **106**, 203107.

87 J. Dai and Z. Tian, Rigorous formalism of anharmonic atomistic Green's function for three-dimensional interfaces, *Phys. Rev. B*, 2020, **101**, 041301.

88 Y. Guo, M. Bescond, Z. Zhang, M. Luisier, M. Nomura and S. Volz, Quantum mechanical modeling of anharmonic phonon–phonon scattering in nanostructures, *Phys. Rev. B*, 2020, **102**, 195412.

89 Y. Guo, Z. Zhang, M. Bescond, S. Xiong, M. Nomura and S. Volz, Anharmonic phonon–phonon scattering at the interface between two solids by nonequilibrium Green's function formalism, *Phys. Rev. B*, 2021, **103**, 174306.

90 T. Feng, L. Lindsay and X. Ruan, Four-phonon scattering significantly reduces intrinsic thermal conductivity of solids, *Phys. Rev. B*, 2017, **96**, 161201.

91 T. Feng and X. Ruan, Four-phonon scattering reduces intrinsic thermal conductivity of graphene and the contributions from flexural phonons, *Phys. Rev. B*, 2018, **97**, 045202.

92 G. Wang, H. Fan, J. Li, Z. Li and Y. Zhou, Direct observation of tunable thermal conductance at solid/porous crystalline solid interfaces induced by water adsorbates, *Nat. Commun.*, 2024, **15**, 2304.

93 Y. Zhou, B. Huang and B.-Y. Cao, Vibrational modes with long mean free path and large volumetric heat capacity drive higher thermal conductivity in amorphous zeolitic imidazolate Framework-4, *Mater. Today Phys.*, 2021, **21**, 100516.

94 Y. Zhou, Y. Xu, Y. Gao and S. Volz, Origin of the weakly temperature-dependent thermal conductivity in ZIF-4 and ZIF-62, *Phys. Rev. Mater.*, 2022, **6**, 015403.

95 H. Babaei and C. E. Wilmer, Mechanisms of Heat Transfer in Porous Crystals Containing Adsorbed Gases: Applications to Metal-Organic Frameworks, *Phys. Rev. Lett.*, 2016, **116**, 025902.

96 H. Babaei, A. J. H. McGaughey and C. E. Wilmer, Effect of pore size and shape on the thermal conductivity of metal–organic frameworks, *Chem. Sci.*, 2017, **8**, 583–589.

97 H. Babaei, A. J. H. McGaughey and C. E. Wilmer, Transient Mass and Thermal Transport during Methane Adsorption into the Metal–Organic Framework HKUST-1, *ACS Appl. Mater. Interfaces*, 2018, **10**, 2400–2406.

98 H. Babaei, M. E. DeCoster, M. Jeong, Z. M. Hassan, T. Islamoglu, H. Baumgart, A. J. H. McGaughey, E. Redel, O. K. Farha, P. E. Hopkins, J. A. Malen and C. E. Wilmer, Observation of reduced thermal conductivity in a metal–organic framework due to the presence of adsorbates, *Nat. Commun.*, 2020, **11**, 4010.

99 H. Fan, C. Yang and Y. Zhou, Ultralong mean free path phonons in HKUST-1 and their scattering by water adsorbates, *Phys. Rev. B*, 2022, **106**, 085417.

100 H. Liu, X. Shi, F. Xu, L. Zhang, W. Zhang, L. Chen, Q. Li, C. Uher, T. Day and G. J. Snyder, Copper ion liquid-like thermoelectrics, *Nat. Mater.*, 2012, **11**, 422–425.

101 Y. Zhou, S. Xiong, X. Zhang, S. Volz and M. Hu, Thermal transport crossover from crystalline to partial-crystalline partial-liquid state, *Nat. Commun.*, 2018, **9**, 4712.

102 Y. Zhou and S. Volz, Thermal transfer in amorphous superionic Li_2S, *Phys. Rev. B*, 2021, **103**, 224204.

103 T. Ouyang, X. Zhang and M. Hu, Thermal conductivity of ordered-disordered material: a case study of superionic Ag_2Te, *Nanotechnology*, 2014, **26**, 025702.

104 W. Liu and Y. Zhou, Energy Transport in Superionic Crystals, *Phys. Rev. Lett.*, 2025, **134**, 146301.

105 X. Xu, J. Zhou and J. Chen, Thermal Transport in Conductive Polymer–Based Materials, *Adv. Funct. Mater.*, 2020, **30**, 1904704.

106 X. Qian, X. Gu and R. Yang, Thermal conductivity modeling of hybrid organic-inorganic crystals and superlattices, *Nano Energy*, 2017, **41**, 394–407.

107 W.-L. Ong and J. A. Malen, Thermal transport in nanostructured organic-inorganic hybrid materials, *Annu. Rev. Heat Transfer*, 2016, **19**, 67–126.

108 G. Wang, H. Fan, Z. Chen, Y. Gao, Z. Wang, Z. Li, H. Lu and Y. Zhou, Tuning Thermal Conductivity of Hybrid Perovskites through Halide Alloying, *Adv. Sci.*, 2024, **11**, 2401194.

109 G. Wang, J. Zheng, J. Xue, Y. Xu, Q. Zheng, G. Hautier, H. Lu and Y. Zhou, Observation of Extraordinary Vibration Scatterings Induced by Strong Anharmonicity in Lead-Free Halide Double Perovskites, *Adv. Sci.*, 2025, **12**, 2408149.

110 J. Zheng, C. Lin, C. Lin, G. Hautier, R. Guo and B. Huang, Unravelling ultralow thermal conductivity in perovskite Cs2AgBiBr6: dominant wave-like phonon tunnelling and strong anharmonicity, *npj Comput. Mater.*, 2024, **10**, 1–13.

111 J. Zheng, D. Shi, Y. Yang, C. Lin, H. Huang, R. Guo and B. Huang, Anharmonicity-induced phonon hardening and phonon transport enhancement in crystalline perovskite $BaZrO_3$, *Phys. Rev. B*, 2022, **105**, 224303.

112 Y. Zhou and M. Hu, Record Low Thermal Conductivity of Polycrystalline Si Nanowire: Breaking the Casimir Limit by Severe Suppression of Propagons, *Nano Lett.*, 2016, **16**, 6178–6187.

113 Y. Zhou, X. Zhang and M. Hu, An excellent candidate for largely reducing interfacial thermal resistance: a nano-confined mass graded interface, *Nanoscale*, 2016, **8**, 1994–2002.

114 M. N. Luckyanova, J. Garg, K. Esfarjani, A. Jandl, M. T. Bulsara, A. J. Schmidt, A. J. Minnich, S. Chen, M. S. Dresselhaus, Z. Ren, E. A. Fitzgerald and G. Chen, Coherent Phonon Heat Conduction in Superlattices, *Science*, 2012, **338**, 936–939.

115 M. Hu and D. Poulikakos, Si/Ge Superlattice Nanowires with Ultralow Thermal Conductivity, *Nano Lett.*, 2012, **12**, 5487–5494.

116 P. K. Schelling, S. R. Phillpot and P. Keblinski, Comparison of atomic-level simulation methods for computing thermal conductivity, *Phys. Rev. B: Condens. Matter Mater. Phys.*, 2002, **65**, 144306.

117 J.-L. Barrat and F. Chiaruttini, Kapitza resistance at the liquid—solid interface, *Mol. Phys.*, 2003, **101**, 1605–1610.

118 A. J. C. Ladd, B. Moran and W. G. Hoover, Lattice thermal conductivity: A comparison of molecular dynamics and anharmonic lattice dynamics, *Phys. Rev. B: Condens. Matter Mater. Phys.*, 1986, **34**, 5058–5064.

119 A. S. Henry and G. Chen, Spectral Phonon Transport Properties of Silicon Based on Molecular Dynamics Simulations and Lattice Dynamics, *J. Comput. Theor. Nanosci.*, 2008, **5**, 141–152.

120 H. R. Seyf, K. Gordiz, F. DeAngelis and A. Henry, Using Green-Kubo modal analysis (GKMA) and interface conductance modal analysis (ICMA) to study phonon transport with molecular dynamics, *J. Appl. Phys.*, 2019, **125**, 081101.

121 W. Lv and A. Henry, Direct calculation of modal contributions to thermal conductivity *via* Green–Kubo modal analysis, *New J. Phys.*, 2016, **18**, 013028.

122 Y. Zhou, X. Zhang and M. Hu, Quantitatively analyzing phonon spectral contribution of thermal conductivity based on nonequilibrium molecular dynamics simulations. I. From space Fourier transform, *Phys. Rev. B: Condens. Matter Mater. Phys.*, 2015, **92**, 195204.

123 Y. Zhou and M. Hu, Quantitatively analyzing phonon spectral contribution of thermal conductivity based on nonequilibrium molecular dynamics simulations. II. From time Fourier transform, *Phys. Rev. B: Condens. Matter Mater. Phys.*, 2015, **92**, 195205.

124 Y. Zhou and M. Hu, Full quantification of frequency-dependent interfacial thermal conductance contributed by two- and three-phonon scattering processes from nonequilibrium molecular dynamics simulations, *Phys. Rev. B*, 2017, **95**, 115313.

125 K. Sääskilahti, J. Oksanen, J. Tulkki and S. Volz, Spectral mapping of heat transfer mechanisms at liquid-solid interfaces, *Phys. Rev. E*, 2016, **93**, 052141.

126 Z. Lu, Y. Wang and X. Ruan, Metal/dielectric thermal interfacial transport considering cross-interface electron-phonon coupling: Theory, two-temperature molecular dynamics, and thermal circuit, *Phys. Rev. B*, 2016, **93**, 064302.

127 Z. Lu, A. Vallabhaneni, B. Cao and X. Ruan, Phonon branch-resolved electron-phonon coupling and the multi-temperature model, *Phys. Rev. B*, 2018, **98**, 134309.

128 Z. Lu, J. Shi and X. Ruan, Role of phonon coupling and non-equilibrium near the interface to interfacial thermal resistance: The multi-temperature model and thermal circuit, *J. Appl. Phys.*, 2019, **125**, 085107.

129 W. Liu, X. Xiang and Y. Zhou, Electron-phonon coupling in polycrystalline silicon, *Phys. Rev. B*, 2025, **112**, 155301.

130 R. Kubo, The fluctuation-dissipation theorem, *Rep. Prog. Phys.*, 1966, **29**, 255–284.

131 K. Gordiz and A. Henry, Phonon transport at interfaces: Determining the correct modes of vibration, *J. Appl. Phys.*, 2016, **119**, 015101.

132 K. Gordiz and A. Henry, A formalism for calculating the modal contributions to thermal interface conductance, *New J. Phys.*, 2015, **17**, 103002.

133 A. Rohskopf, R. Li, T. Luo and A. Henry, A Computational Framework for Modeling and Simulating Vibrational Mode Dynamics, *Modell. Simul. Mater. Sci. Eng.*, 2022, **30**, 045010.

134 K. Gordiz, M. G. Muraleedharan and A. Henry, Interface conductance modal analysis of a crystalline Si-amorphous SiO_2 interface, *J. Appl. Phys.*, 2019, **125**, 135102.

135 T. Feng, Y. Zhong, J. Shi and X. Ruan, Unexpected high inelastic phonon transport across solid-solid interface: Modal nonequilibrium molecular dynamics simulations and Landauer analysis, *Phys. Rev. B*, 2019, **99**, 045301.

136 Y. Xu, H. Fan, Z. Li and Y. Zhou, Signatures of anharmonic phonon transport in ultrahigh thermal conductance across atomically sharp metal/semiconductor interface, *Int. J. Heat Mass Transfer*, 2023, **201**, 123628.

137 T. Feng, W. Yao, Z. Wang, J. Shi, C. Li, B. Cao and X. Ruan, Spectral analysis of nonequilibrium molecular dynamics: Spectral phonon temperature and local nonequilibrium in thin films and across interfaces, *Phys. Rev. B*, 2017, **95**, 195202.

138 K. Khot, B. Xiao, Z. Han, Z. Guo, Z. Xiong and X. Ruan, Phonon local non-equilibrium at Al/Si interface from machine learning molecular dynamics, *J. Appl. Phys.*, 2025, **137**, 115301.

139 M. T. Dove, *Introduction to Lattice Dynamics*, Cambridge University Press, Cambridge, 1993.

140 K. Sääskilahti, J. Oksanen, S. Volz and J. Tulkki, Frequency-dependent phonon mean free path in carbon nanotubes from nonequilibrium molecular dynamics, *Phys. Rev. B: Condens. Matter Mater. Phys.*, 2015, **91**, 115426.

141 D. P. Sellan, E. S. Landry, J. E. Turney, A. J. H. McGaughey and C. H. Amon, Size effects in molecular dynamics thermal conductivity predictions, *Phys. Rev. B: Condens. Matter Mater. Phys.*, 2010, **81**, 214305.

142 S. Hu, C. Y. Zhao and X. Gu, Impact of thermostat on interfacial thermal conductance prediction from non-equilibrium molecular dynamics simulations, *Chin. Phys. B*, 2022, **31**, 056301.

 This journal is © the Owner Societies 2026

143 Z. Li, S. Xiong, C. Sievers, Y. Hu, Z. Fan, N. Wei, H. Bao, S. Chen, D. Donadio and T. Ala-Nissila, Influence of thermostatting on nonequilibrium molecular dynamics simulations of heat conduction in solids, *J. Chem. Phys.*, 2019, **151**, 234105.

144 Y. Hu, T. Feng, X. Gu, Z. Fan, X. Wang, M. Lundstrom, S. S. Shrestha and H. Bao, Unification of nonequilibrium molecular dynamics and the mode-resolved phonon Boltzmann equation for thermal transport simulations, *Phys. Rev. B*, 2020, **101**, 155308.

145 X. Gu, Z. Fan and H. Bao, Thermal conductivity prediction by atomistic simulation methods: Recent advances and detailed comparison, *J. Appl. Phys.*, 2021, **130**, 210902.

146 Z. Fan, H. Dong, A. Harju and T. Ala-Nissila, Homogeneous nonequilibrium molecular dynamics method for heat transport and spectral decomposition with many-body potentials, *Phys. Rev. B*, 2019, **99**, 064308.

147 S. Berber, Y.-K. Kwon and D. Tománek, Unusually High Thermal Conductivity of Carbon Nanotubes, *Phys. Rev. Lett.*, 2000, **84**, 4613–4616.

148 D. J. Evans, Homogeneous NEMD algorithm for thermal conductivity—Application of non-canonical linear response theory, *Phys. Lett. A*, 1982, **91**, 457–460.

149 J. Wang and J.-S. Wang, Carbon nanotube thermal transport: Ballistic to diffusive, *Appl. Phys. Lett.*, 2006, **88**, 111909.

150 T. Yamamoto, S. Konabe, J. Shiomi and S. Maruyama, Crossover from Ballistic to Diffusive Thermal Transport in Carbon Nanotubes, *Appl. Phys. Express*, 2009, **2**, 095003.

151 L. G. C. Rego and G. Kirczenow, Quantized Thermal Conductance of Dielectric Quantum Wires, *Phys. Rev. Lett.*, 1998, **81**, 232–235.

152 J. E. Turney, E. S. Landry, A. J. H. McGaughey and C. H. Amon, Predicting phonon properties and thermal conductivity from anharmonic lattice dynamics calculations and molecular dynamics simulations, *Phys. Rev. B: Condens. Matter Mater. Phys.*, 2009, **79**, 064301.

153 Y. Xu, L. Yang and Y. Zhou, The interfacial thermal conductance spectrum in nonequilibrium molecular dynamics simulations considering anharmonicity, asymmetry and quantum effects, *Phys. Chem. Chem. Phys.*, 2022, **24**, 24503–24513.

154 R. Landauer, Conductance from transmission: common sense points, *Phys. Scr.*, 1992, **T42**, 110–114.

155 J. Xu and Y. Guo, Uncovering the roughness effect on inelastic phonon scattering and thermal conductance at interface *via* spectral energy exchange, *Int. J. Heat Mass Transfer*, 2025, **250**, 127295.

156 Z. Wang, B. Linghui, D. Li, J. Zhu and D. Tang, Systematic investigation of interfacial heat transport at Metal/GaN interfaces: Experimental and simulation validation, *Int. J. Heat Mass Transfer*, 2026, **261**, 128564.

157 Q. Wang, X. Wang, X. Liu and J. Zhang, Interfacial engineering for the enhancement of interfacial thermal conductance in GaN/AlN heterostructure, *J. Appl. Phys.*, 2021, **129**, 235102.

158 H. Zhou, K. Z. Adnan, W. A. Jones and T. Feng, Thermal boundary conductance in standalone and nonstandalone GaN/AlN heterostructures predicted using machine-learning interatomic potentials, *Phys. Rev. B*, 2025, **112**, 235308.

159 W. Chen, Q. Zhou, Q. Han, C. Liu, X. Jiang, Y. Gu, G. Wu, Y. Zhang, Z. Wei and Y. Chen, Elastic and inelastic phonon scattering effects on thermal conductance across Au/graphene/Au interface, *J. Appl. Phys.*, 2024, **135**, 165107.

160 Y. Xu and Y. Zhou, Metric for quantifying elastic and inelastic thermal transport at interfaces, *Phys. Rev. B*, 2024, **110**, 115305.

161 Q. He, Y. Xu, H. Wang, Z. Li and Y. Zhou, Role of elastic phonon couplings in dictating the thermal transport across atomically sharp SiC/Si interfaces, *Int. J. Therm. Sci.*, 2024, **204**, 109182.

162 P. E. Hopkins, J. C. Duda, C. W. Petz and J. A. Floro, Controlling thermal conductance through quantum dot roughening at interfaces, *Phys. Rev. B: Condens. Matter Mater. Phys.*, 2011, **84**, 035438.

163 Y. Xu and Y. Zhou, Collaborative mechanisms boost the nanoscale boiling heat transfer at functionalized gold surfaces, *Int. J. Heat Mass Transfer*, 2023, **210**, 124179.

164 Y. Xu, F. Duan, Z. Li and Y. Zhou, Surface functionalization enabling highly effective phase-change heat transfer of R1234yf: A molecular dynamics study, *Appl. Therm. Eng.*, 2024, **240**, 122275.

165 A. El-Rifai, S. Perumanath, M. K. Borg and R. Pillai, Unraveling the Regimes of Interfacial Thermal Conductance at a Solid/Liquid Interface, *J. Phys. Chem. C*, 2024, **128**, 8408–8417.

166 S. Li and H. Qiu, Anomalous interfacial thermal conductance between metal and water under high pressures, *Int. J. Heat Mass Transfer*, 2026, **257**, 128258.

167 W. Liu, Y. Xu, Z. Li, F. Duan and Y. Zhou, Enhancing nanoscale phase-change heat transfer by collaborative roles of surface functionalization and external electric field, *Int. J. Heat Mass Transfer*, 2025, **236**, 126363.

168 C. T. Nguyen, G. Roy, C. Gauthier and N. Galanis, Heat transfer enhancement using Al2O3–water nanofluid for an electronic liquid cooling system, *Appl. Therm. Eng.*, 2007, **27**, 1501–1506.

169 N. Mei, X. Xu and R. Li, Heat Dissipation Analysis on the Liquid Cooling System Coupled with a Flat Heat Pipe of a Lithium-Ion Battery, *ACS Omega*, 2020, **5**, 17431–17441.

170 P. Birbarah, T. Gebrael, T. Foulkes, A. Stillwell, A. Moore, R. Pilawa-Podgurski and N. Miljkovic, Water immersion cooling of high power density electronics, *Int. J. Heat Mass Transfer*, 2020, **147**, 118918.

171 N. A. Pambudi, A. Sarifudin, R. A. Firdaus, D. K. Ulfa, I. M. Gandidi and R. Romadhon, The immersion cooling technology: Current and future development in energy saving, *Alexandria Eng. J.*, 2022, **61**, 9509–9527.

172 D. Attinger, C. Frankiewicz, A. R. Betz, T. M. Schutzius, R. Ganguly, A. Das, C.-J. Kim and C. M. Megaridis, Surface engineering for phase change heat transfer: A review, *MRS Energy & Sustainability*, 2014, **1**, E4.

173 H. J. Cho, D. J. Preston, Y. Zhu and E. N. Wang, Nanoengineered materials for liquid–vapour phase-change heat transfer, *Nat. Rev. Mater.*, 2016, **2**, 1–17.

174 R. Wen, X. Ma, Y.-C. Lee and R. Yang, Liquid-Vapor Phase-Change Heat Transfer on Functionalized Nanowired Surfaces and Beyond, *Joule*, 2018, **2**, 2307–2347.

175 X. Li, S. Wang, R. Wen, X. Ma and R. Yang, Liquid film boiling enabled ultra-high conductance and high flux heat spreaders, *Cell Rep. Phys. Sci.*, 2022, **3**, 100746.

176 H. Hu and Y. Sun, Effect of nanostructures on heat transfer coefficient of an evaporating meniscus, *Int. J. Heat Mass Transfer*, 2016, **101**, 878–885.

177 H. Hu and Y. Sun, Effect of nanopatterns on Kapitza resistance at a water-gold interface during boiling: A molecular dynamics study, *J. Appl. Phys.*, 2012, **112**, 053508.

178 Y. Wang and P. Keblinski, Role of wetting and nanoscale roughness on thermal conductance at liquid-solid interface, *Appl. Phys. Lett.*, 2011, **99**, 073112.

179 C. Zhang, Y. Chen and G. P. Peterson, Thermal slip for liquids at rough solid surfaces, *Phys. Rev. E: Stat., Nonlinear, Soft Matter Phys.*, 2014, **89**, 062407.

180 H. Sam Huang, J. L. Wohlwend, V. Varshney and A. K. Roy, Heat Transfer at Aluminum–Water Interfaces: Effect of Surface Roughness, *Proceedings of the ASME 2012 International Mechanical Engineering Congress and Exposition*, 2012, vol. 7, 1695–1702.

181 Y.-J. Chen, B. Yu, Y. Zou, B.-N. Chen and W.-Q. Tao, Molecular dynamics studies of bubble nucleation on a grooved substrate, *Int. J. Heat Mass Transfer*, 2020, **158**, 119850.

182 B. Ramos-Alvarado and S. Kumar, Spectral Analysis of the Heat Flow Across Crystalline and Amorphous Si–Water Interfaces, *J. Phys. Chem. C*, 2017, **121**, 11380–11389.

183 C. U. Gonzalez-Valle and B. Ramos-Alvarado, Spectral mapping of thermal transport across SiC-water interfaces, *Int. J. Heat Mass Transfer*, 2019, **131**, 645–653.

184 N. Shenogina, R. Godawat, P. Keblinski and S. Garde, How Wetting and Adhesion Affect Thermal Conductance of a Range of Hydrophobic to Hydrophilic Aqueous Interfaces, *Phys. Rev. Lett.*, 2009, **102**, 156101.

185 H. Harikrishna, W. A. Ducker and S. T. Huxtable, The influence of interface bonding on thermal transport through solid–liquid interfaces, *Appl. Phys. Lett.*, 2013, **102**, 251606.

186 Z. Ge, D. G. Cahill and P. V. Braun, Thermal Conductance of Hydrophilic and Hydrophobic Interfaces, *Phys. Rev. Lett.*, 2006, **96**, 186101.

187 T. P. Allred, J. A. Weibel and S. V. Garimella, Enabling Highly Effective Boiling from Superhydrophobic Surfaces, *Phys. Rev. Lett.*, 2018, **120**, 174501.

188 A. Giri and P. E. Hopkins, Spectral analysis of thermal boundary conductance across solid/classical liquid interfaces: A molecular dynamics study, *Appl. Phys. Lett.*, 2014, **105**, 033106.

189 A. Giri, J. L. Braun and P. E. Hopkins, Implications of Interfacial Bond Strength on the Spectral Contributions to Thermal Boundary Conductance across Solid, Liquid, and Gas Interfaces: A Molecular Dynamics Study, *J. Phys. Chem. C*, 2016, **120**, 24847–24856.

190 A. Dhar, Heat transport in low-dimensional systems, *Adv. Phys.*, 2008, **57**, 457–537.

191 F. Sun, T. Zhang, M. M. Jobbins, Z. Guo, X. Zhang, Z. Zheng, D. Tang, S. Ptasinska and T. Luo, Molecular Bridge Enables Anomalous Enhancement in Thermal Transport across Hard-Soft Material Interfaces, *Adv. Mater.*, 2014, **26**, 6093–6099.

192 T. Zhang, A. R. Gans-Forrest, E. Lee, X. Zhang, C. Qu, Y. Pang, F. Sun and T. Luo, Role of Hydrogen Bonds in Thermal Transport across Hard/Soft Material Interfaces, *ACS Appl. Mater. Interfaces*, 2016, **8**, 33326–33334.

193 H. Fan, C. Yang and X. Wang, Tuning Interfacial Thermal Conductance Across Metal–Organic Semiconductor Interfaces by Mixing Self-Assembled Monolayers, *ACS Appl. Electron. Mater.*, 2022, **4**, 718–728.

194 X. Ran and B. Cao, Roughness dependence of phonon-interface thermal transport: Theoretical model and Monte Carlo simulation, *Phys. Rev. B*, 2024, **110**, 024302.

195 Y. Shen, H.-A. Yang and B.-Y. Cao, Near-junction phonon thermal spreading in GaN HEMTs: A comparative study of simulation techniques by full-band phonon Monte Carlo method, *Int. J. Heat Mass Transfer*, 2023, **211**, 124284.

196 B.-D. Nie and B.-Y. Cao, Reflection and refraction of a thermal wave at an ideal interface, *Int. J. Heat Mass Transfer*, 2018, **116**, 314–328.

197 Y. Hu, R. Jia, J. Xu, Y. Sheng, M. Wen, J. Lin, Y. Shen and H. Bao, GiftBTE: an efficient deterministic solver for non-gray phonon Boltzmann transport equation, *J. Phys.: Condens. Matter*, 2023, **36**, 025901.

198 Y. Sheng, S. Wang, Y. Hu, J. Xu, Z. Ji and H. Bao, Integrating First-Principles-Based Non-Fourier Thermal Analysis Into Nanoscale Device Simulation, *IEEE Trans. Electron Devices*, 2024, **71**, 1769–1775.

199 Y. Sheng, Y. Xia, J. Xu, S. Wang, P. Ren, Z. Ji and H. Bao, Multiscale Thermal Simulation for GAAFET With First-Principles-Based Boltzmann Transport Equation, *IEEE Trans. Electron Devices*, 2025, **72**, 4700–4707.

200 R. Jia, X. Zhang, Y. Sheng, J. Xu, Y. Xia and H. Bao, Thermal transport near hotspots in cryogenic devices *via* the phonon Boltzmann transport equation, *J. Appl. Phys.*, 2026, **139**, 015705.

201 B. Cao, Thermal design automation (TDA) for multiscale thermal management of electronics, *J. Appl. Phys.*, 2025, **138**, 180901.

202 X. Qian, G. Quan, T.-H. Liu and R. Yang, API phonons: Python interfaces for phonon transport modeling, *Mater. Today Phys.*, 2025, **50**, 101630.

203 X. Qian, C. Zhang, T.-H. Liu and R. Yang, Analytical Green's function of the multidimensional Boltzmann transport equation for modeling hydrodynamic second sound, *Phys. Rev. B*, 2025, **111**, 035406.

204 Y. Guo and M. Wang, Lattice Boltzmann modeling of phonon transport, *J. Comput. Phys.*, 2016, **315**, 1–15.

 This journal is © the Owner Societies 2026

205 C. Zhang and Z. Guo, Discrete unified gas kinetic scheme for multiscale heat transfer with arbitrary temperature difference, *Int. J. Heat Mass Transfer*, 2019, **134**, 1127–1136.

206 A. Nabovati, D. P. Sellan and C. H. Amon, On the lattice Boltzmann method for phonon transport, *J. Comput. Phys.*, 2011, **230**, 5864–5876.

207 J. Liu, X. Xiang, Y. Zhou and W. Su, General synthetic iterative scheme for fast solving coupled electron–phonon Boltzmann equations, *Int. J. Heat Mass Transfer*, 2026, **260**, 128510.

208 D. Shen and W. Su, Accurate-geometry-embodied finite element method for phonon Boltzmann transport equation, *Comput. Phys. Commun.*, 2025, **313**, 109623.

209 X.-P. Luo, Y.-Y. Guo, M.-R. Wang and H.-L. Yi, Direct simulation of second sound in graphene by solving the phonon Boltzmann equation *via* a multiscale scheme, *Phys. Rev. B*, 2019, **100**, 155401.

210 D. Singh, J. Y. Murthy and T. S. Fisher, Effect of Phonon Dispersion on Thermal Conduction Across Si/Ge Interfaces, *J. Heat Transfer*, 2011, **133**, 122401.

211 Y. Hu, Y. Shen and H. Bao, Ultra-efficient and parameter-free computation of submicron thermal transport with phonon Boltzmann transport equation, *Fundam. Res.*, 2024, **4**, 907–915.

212 J. Xu, Y. Sheng, Z. Wang and H. Bao, Isovalent Doping Reduces Channel Temperature Within Nanoscale Devices, *IEEE Trans. Electron Devices*, 2025, **72**, 4333–4339.

213 W. Shang, J. Zhou, J. P. Panda, Z. Xu, Y. Liu, P. Du, J.-X. Wang and T. Luo, JAX-BTE: a GPU-accelerated differentiable solver for phonon Boltzmann transport equations, *npj Comput. Mater.*, 2025, **11**, 129.

214 J. P. Panda, W. Shang, Y. Liu, J. Zhou, J. Liang, J.-X. Wang and T. Luo, Scalable non-diffusive thermal analysis of field-effect transistors using neural operators, *APL Electron. Devices*, 2026, **2**, 016118.

215 J. Zhou, R. Li, W. Shang, Y. Liu, J. P. Panda, P. Du, X.-Y. Liu, J. Liang, B.-C. Ma, J.-X. Wang and T. Luo, Physics-informed neural networks with hard-encoded angle-dependent boundary conditions for phonon Boltzmann transport equation, *Mater. Today Phys.*, 2025, **59**, 101922.

216 Y. Xu, B.-Y. Cao and Y. Zhou, Near-interface effects on interfacial phonon transport: Competition between phonon–phonon interference and phonon–phonon scattering, *Int. J. Heat Mass Transfer*, 2024, **232**, 125943.

217 K. Z. Adnan and T. Feng, Thermal boundary conductance and thermal conductivity strongly depend on nearby environment, *Phys. Rev. B*, 2024, **109**, 245302.

218 S. Lu, Z. Zhang, S. Shan, Y. Li, P. Hänggi and J. Chen, Effect of spatial coherence on phonon transmission at interfaces, *Phys. Rev. B*, 2026, **113**, 165302.

219 Y. Liu, Y. Liu, J. Yue, L. Xiong, L.-L. Nian and S. Hu, Modulation of interface modes for resonance-induced enhancement of the interfacial thermal conductance in pillar-based Si/Ge nanowires, *Phys. Rev. B*, 2023, **108**, 235426.

220 P. Kim, L. Shi, A. Majumdar and P. L. McEuen, Thermal Transport Measurements of Individual Multiwalled Nanotubes, *Phys. Rev. Lett.*, 2001, **87**, 215502.

221 J. Yang, S. Waltermire, Y. Chen, A. A. Zinn, T. T. Xu and D. Li, Contact thermal resistance between individual multiwall carbon nanotubes, *Appl. Phys. Lett.*, 2010, **96**, 023109.

222 Z. Wang, R. Xie, C. T. Bui, D. Liu, X. Ni, B. Li and J. T. L. Thong, Thermal Transport in Suspended and Supported Few-Layer Graphene, *Nano Lett.*, 2011, **11**, 113–118.

223 D. Liu, R. Xie, N. Yang, B. Li and J. T. L. Thong, Profiling Nanowire Thermal Resistance with a Spatial Resolution of Nanometers, *Nano Lett.*, 2014, **14**, 806–812.

224 Y. Yue, X. Chen and X. Wang, Noncontact Sub-10 nm Temperature Measurement in Near-Field Laser Heating, *ACS Nano*, 2011, **5**, 4466–4475.

225 A. A. Balandin, S. Ghosh, W. Bao, I. Calizo, D. Teweldebrhan, F. Miao and C. N. Lau, Superior Thermal Conductivity of Single-Layer Graphene, *Nano Lett.*, 2008, **8**, 902–907.

226 Q. Meng, J. Zhang, Y. Zhang, W. Chu, W. Mao, Y. Zhang, J. Yang, Y. Luo, Z. Dong and J. G. Hou, Local heating and Raman thermometry in a single molecule, *Sci. Adv.*, 2024, **10**, eadl1015.

227 F. Liu, R. Mao, Z. Liu, J. Du and P. Gao, Probing phonon transport dynamics across an interface by electron microscopy, *Nature*, 2025, **642**, 941–946.

228 D. G. Cahill, Thermal conductivity measurement from 30 to 750 K: the 3ω method, *Rev. Sci. Instrum.*, 1990, **61**, 802–808.

229 S.-M. Lee and D. G. Cahill, Heat transport in thin dielectric films, *J. Appl. Phys.*, 1997, **81**, 2590–2595.

230 A. J. Schmidt, R. Cheaito and M. Chiesa, A frequency-domain thermoreflectance method for the characterization of thermal properties, *Rev. Sci. Instrum.*, 2009, **80**, 094901.

231 D. J. Kirsch, J. Martin, R. Warzoha, M. McLean, D. Windover and I. Takeuchi, An instrumentation guide to measuring thermal conductivity using frequency domain thermoreflectance (FDTR), *Rev. Sci. Instrum.*, 2024, **95**, 103006.

232 D. G. Cahill, Analysis of heat flow in layered structures for time-domain thermoreflectance, *Rev. Sci. Instrum.*, 2004, **75**, 5119–5122.

233 P. Jiang, X. Qian and R. Yang, Tutorial: Time-domain thermoreflectance (TDTR) for thermal property characterization of bulk and thin film materials, *J. Appl. Phys.*, 2018, **124**, 161103.

234 K. Kang, Y. K. Koh, C. Chiritescu, X. Zheng and D. G. Cahill, Two-tint pump–probe measurements using a femtosecond laser oscillator and sharp-edged optical filters, *Rev. Sci. Instrum.*, 2008, **79**, 114901.

235 S. Xu, T. Wang, D. Hurley, Y. Yue and X. Wang, Development of time-domain differential Raman for transient thermal probing of materials, *Opt. Express*, 2015, **23**, 10040–10056.

236 Q.-Y. Li, X. Zhang and Y.-D. Hu, Laser flash Raman spectroscopy method for thermophysical characterization of 2D nanomaterials, *Thermochim. Acta*, 2014, **592**, 67–72.

237 H. D. Nguyen, I. Yamada, T. Nishimura, H. Pang, H. Cho, D.-M. Tang, J. Kikkawa, M. Mitome, D. Golberg, K. Kimoto,

T. Mori and N. Kawamoto, STEM in situ thermal wave observations for investigating thermal diffusivity in nanoscale materials and devices, *Sci. Adv.*, 2024, **10**, eadj3825.
238 J. Zhu, D. Tang, W. Wang, J. Liu, K. W. Holub and R. Yang, Ultrafast thermoreflectance techniques for measuring thermal conductivity and interface thermal conductance of thin films, *J. Appl. Phys.*, 2010, **108**, 094315.
239 J. Lu, Z. Xie, R. Chen, Z. Lin, T. Lai, Z. Wang and K. Chen, Characterization of thermal boundary conductance of 2D–3D van der Waals interface using wideband transducerless frequency-domain thermoreflectance, *J. Appl. Phys.*, 2025, **138**, 105102.
240 K. T. Regner, S. Majumdar and J. A. Malen, Instrumentation of broadband frequency domain thermoreflectance for measuring thermal conductivity accumulation functions, *Rev. Sci. Instrum.*, 2013, **84**, 064901.
241 L. Wang, R. Cheaito, J. L. Braun, A. Giri and P. E. Hopkins, Thermal conductivity measurements of non-metals *via* combined time- and frequency-domain thermoreflectance without a metal film transducer, *Rev. Sci. Instrum.*, 2016, **87**, 094902.
242 J. Yang, C. Maragliano and A. J. Schmidt, Thermal property microscopy with frequency domain thermoreflectance, *Rev. Sci. Instrum.*, 2013, **84**, 104904.
243 T. Favaloro, J.-H. Bahk and A. Shakouri, Characterization of the temperature dependence of the thermoreflectance coefficient for conductive thin films, *Rev. Sci. Instrum.*, 2015, **86**, 024903.
244 R. J. Warzoha, A. A. Wilson, B. F. Donovan, A. Clark, X. Cheng, L. An and G. Feng, Measurements of Thermal Resistance Across Buried Interfaces with Frequency-Domain Thermoreflectance and Microscale Confinement, *ACS Appl. Mater. Interfaces*, 2024, **16**, 41633–41641.
245 D. Fournier, M. Marangolo and C. Fretigny, Measurement of thermal properties of bulk materials and thin films by modulated thermoreflectance (MTR), *J. Appl. Phys.*, 2020, **128**, 241101.
246 Z. Qian, G. Zhang, Z. Lai, A. Hanai, Y. Xu, G. Wang, Y. Lu, J. Gu, Y. Zhou, T. Yanagitani, J. Jia and Q. Zheng, Tailoring thermal transport in (Sc,Yb)AlN thin films to the glassy limit, *Acta Mater.*, 2026, **304**, 121767.
247 Y. Akura, Y. Ikeda, Y. Matsunaga, M. Shimofuri, A. Banerjee, T. Tsuchiya and J. Hirotani, Frequency-domain thermoreflectance with beam offset without the spot distortion for accurate thermal conductivity measurement of anisotropic materials, *Rev. Sci. Instrum.*, 2025, **96**, 014902.
248 A. Camacho de la Rosa, R. Esquivel-Sirvent and D. Becerril, Relaxation times of non-Fourier materials using frequency-domain thermoreflectance, *J. Appl. Phys.*, 2025, **137**, 155103.
249 Y. Liang, K. A. Treaster, A. Majumder, M. Settipalli, K. Panda, S. Godse, R. Roy, R. Mali, Z. Wang, Y. Luan, P. Hu, K. Searles, D. C. McLeod, K. A. Page, D. Bhagwandin, E. Meyhofer, P. Reddy, A. J. H. McGaughey, A. M. Evans and J. A. Malen, Anisotropic Thermal Conductivity in Imine-Linked Two-Dimensional Polymer Films Produced by Interfacial Polymerization, *ACS Nano*, 2025, **19**, 19009–19017.
250 S. Saurav and S. Mazumder, Extraction of thermal conductivity using phonon Boltzmann Transport Equation based simulation of frequency domain thermo-reflectance experiments, *Int. J. Heat Mass Transfer*, 2023, **204**, 123871.
251 R. Muthaiah, R. S. Annam, F. Tarannum, A. K. Gupta, J. Garg and S. Arafin, Length dependence thermal conductivity of zinc selenide (ZnSe) and zinc telluride (ZnTe) – a combined first principles and frequency domain thermoreflectance (FDTR) study, *Phys. Chem. Chem. Phys.*, 2022, **24**, 28814–28824.
252 E. Ziade, J. Yang, G. Brummer, D. Nothern, T. Moustakas and A. J. Schmidt, Thermal transport through GaN–SiC interfaces from 300 to 600 K, *Appl. Phys. Lett.*, 2015, **107**, 091605.
253 Z. Wang, X. Tian, J. Liang, J. Zhu, D. Tang and K. Xu, Prediction and measurement of thermal transport across interfaces between semiconductor and adjacent layers, *Int. J. Therm. Sci.*, 2014, **79**, 266–275.
254 J. Wang, Z. Wang, K. Yang, N. Chen, J. Ni, J. Song, Q. Li, F. Sun, Y. Liu and T. Fan, Enhanced Heat Transport Capability across Boron Nitride/Copper Interface through Inelastic Phonon Scattering, *Adv. Funct. Mater.*, 2022, **32**, 2206545.
255 D. Saha, X. Yu, M. Jeong, M. Darwish, J. Weldon, A. J. Gellman and J. A. Malen, Impact of metal adhesion layer diffusion on thermal interface conductance, *Phys. Rev. B*, 2019, **99**, 115418.
256 J. P. Freedman, X. Yu, R. F. Davis, A. J. Gellman and J. A. Malen, Thermal interface conductance across metal alloy–dielectric interfaces, *Phys. Rev. B*, 2016, **93**, 035309.
257 K. Yu, R. Enright and D. McCloskey, *2022 21st IEEE Intersociety Conference on Thermal and Thermomechanical Phenomena in Electronic Systems (iTherm)*, 2022, pp. 1–6.
258 A. Schmidt, M. Chiesa, X. Chen and G. Chen, An optical pump–probe technique for measuring the thermal conductivity of liquids, *Rev. Sci. Instrum.*, 2008, **79**, 064902.
259 G. Meng, J. Chen, W. Bao and Z. Wang, Characterization of thermal boundary resistance at solid–liquid interface based on continuous wave frequency domain thermal reflection method, *Heat Mass Transfer*, 2023, **59**, 203–213.
260 Y. Jiao, K. Miyazaki and T. Yabuki, Measurement of thermal boundary resistance between water and super-hydrophobic surfaces by the bi-directional differential 3ω method, *Int. Commun. Heat Mass Transfer*, 2021, **126**, 105404.
261 H. S. Huang, A. K. Roy, V. Varshney, J. L. Wohlwend and S. A. Putnam, Temperature dependence of thermal conductance between aluminum and water, *Int. J. Therm. Sci.*, 2012, **59**, 17–20.
262 P. A. E. Schoen, B. Michel, A. Curioni and D. Poulikakos, Hydrogen-bond enhanced thermal energy transport at functionalized, hydrophobic and hydrophilic silica–water interfaces, *Chem. Phys. Lett.*, 2009, **476**, 271–276.
263 W. Chen and G. Nagayama, Kapitza Length at Solid–Liquid Interface: From Nanoscale to Microscale, *Small Sci.*, 2025, **5**, 2400626.

 This journal is © the Owner Societies 2026

264 T. Chen and P. Jiang, Universal thermometry of solid–liquid interfacial thermal conductance, *Appl. Phys. Lett.*, 2025, **127**, 191608.

265 T. Chen and P. Jiang, An optical method for measuring local convective heat transfer coefficients over 100 W/(m^2 K) with sub-millimeter resolution, *Measurement*, 2025, **249**, 117001.

266 T. Chen and P. Jiang, Simultaneous, Non-Contact Measurement of Liquid and Interfacial Thermal Properties *via* a Differential Square-Pulsed Source Method, *Langmuir*, 2025, **41**, 26496–26504.

267 K. T. Regner, D. P. Sellan, Z. Su, C. H. Amon, A. J. H. McGaughey and J. A. Malen, Broadband phonon mean free path contributions to thermal conductivity measured using frequency domain thermoreflectance, *Nat. Commun.*, 2013, **4**, 1640.

268 J. P. Freedman, J. H. Leach, E. A. Preble, Z. Sitar, R. F. Davis and J. A. Malen, Universal phonon mean free path spectra in crystalline semiconductors at high temperature, *Sci. Rep.*, 2013, **3**, 2963.

269 P. Jiang, X. Qian and R. Yang, Time-domain thermoreflectance (TDTR) measurements of anisotropic thermal conductivity using a variable spot size approach, *Rev. Sci. Instrum.*, 2017, **88**, 074901.

270 P. Jiang, B. Huang and Y. K. Koh, Accurate measurements of cross-plane thermal conductivity of thin films by dual-frequency time-domain thermoreflectance (TDTR), *Rev. Sci. Instrum.*, 2016, **87**, 075101.

271 A. J. Schmidt, X. Chen and G. Chen, Pulse accumulation, radial heat conduction, and anisotropic thermal conductivity in pump–probe transient thermoreflectance, *Rev. Sci. Instrum.*, 2008, **79**, 114902.

272 B. Xu, S. Hu, S.-W. Hung, C. Shao, H. Chandra, F.-R. Chen, T. Kodama and J. Shiomi, Weaker bonding can give larger thermal conductance at highly mismatched interfaces, *Sci. Adv.*, 2021, **7**, eabf8197.

273 S. Semal, C. Bauthier, M. Voué, J. J. Vanden Eynde, R. Gouttebaron and J. De Coninck, Spontaneous Spreading of Liquid Droplets on Mixed Alkanethiol Monolayers: Dynamics of Wetting and Wetting Transition, *J. Phys. Chem. B*, 2000, **104**, 6225–6232.

274 H. Fukushima, S. Seki, T. Nishikawa, H. Takiguchi, K. Tamada, K. Abe, R. Colorado, M. Graupe, O. E. Shmakova and T. R. Lee, Microstructure, Wettability, and Thermal Stability of Semifluorinated Self-Assembled Monolayers (SAMs) on Gold, *J. Phys. Chem. B*, 2000, **104**, 7417–7423.

275 P. S. Noonan, A. Shavit, B. R. Acharya and D. K. Schwartz, Mixed Alkylsilane Functionalized Surfaces for Simultaneous Wetting and Homeotropic Anchoring of Liquid Crystals, *ACS Appl. Mater. Interfaces*, 2011, **3**, 4374–4380.

276 Z. Ma, Z. Guo and D. Wang, Wet and Wild: Adventurous Wetting Expeditions on Tailored Surfaces of Self-Assembled Monolayers, *ACS Nano*, 2025, **19**, 33667–33680.

277 Z. Tian, A. Marconnet and G. Chen, Enhancing solid–liquid interface thermal transport using self-assembled monolayers, *Appl. Phys. Lett.*, 2015, **106**, 211602.

278 D. Huang, R. Ma, T. Zhang and T. Luo, Origin of Hydrophilic Surface Functionalization-Induced Thermal Conductance Enhancement across Solid–Water Interfaces, *ACS Appl. Mater. Interfaces*, 2018, **10**, 28159–28165.

279 H. Fan, M. Wang, D. Han, J. Zhang, J. Zhang and X. Wang, Enhancement of Interfacial Thermal Transport between Metal and Organic Semiconductor Using Self-Assembled Monolayers with Different Terminal Groups, *J. Phys. Chem. C*, 2020, **124**, 16748–16757.

280 X. Wei, T. Zhang and T. Luo, Thermal Energy Transport across Hard–Soft Interfaces, *ACS Energy Lett.*, 2017, **2**, 2283–2292.

281 M. Li, H. Wu, E. M. Avery, Z. Qin, D. P. Goronzy, H. D. Nguyen, T. Liu, P. S. Weiss and Y. Hu, Electrically gated molecular thermal switch, *Science*, 2023, **382**, 585–589.

282 J. P. Feser and D. G. Cahill, Probing anisotropic heat transport using time-domain thermoreflectance with offset laser spots, *Rev. Sci. Instrum.*, 2012, **83**, 104901.

283 J. P. Feser, J. Liu and D. G. Cahill, Pump-probe measurements of the thermal conductivity tensor for materials lacking in-plane symmetry, *Rev. Sci. Instrum.*, 2014, **85**, 104903.

284 M. Li, J. S. Kang and Y. Hu, Anisotropic thermal conductivity measurement using a new Asymmetric-Beam Time-Domain Thermoreflectance (AB-TDTR) method, *Rev. Sci. Instrum.*, 2018, **89**, 084901.

285 M. Li, J. S. Kang, H. D. Nguyen, H. Wu, T. Aoki and Y. Hu, Anisotropic Thermal Boundary Resistance across 2D Black Phosphorus: Experiment and Atomistic Modeling of Interfacial Energy Transport, *Adv. Mater.*, 2019, **31**, 1901021.

286 Y. Hu, L. Zeng, A. J. Minnich, M. S. Dresselhaus and G. Chen, Spectral mapping of thermal conductivity through nanoscale ballistic transport, *Nat. Nanotechnol.*, 2015, **10**, 701–706.

287 J. S. Kang, M. Li, H. Wu, H. Nguyen and Y. Hu, Experimental observation of high thermal conductivity in boron arsenide, *Science*, 2018, **361**, 575–578.

288 M. Li, K. Pan, Y. Ge, K. Huynh, M. S. Goorsky, T. S. Fisher and Y. Hu, Wafer-scale bonded GaN–AlN with high interface thermal conductance, *Appl. Phys. Lett.*, 2024, **125**, 032104.

289 S. Yue, F. Tian, X. Sui, M. Mohebinia, X. Wu, T. Tong, Z. Wang, B. Wu, Q. Zhang, Z. Ren, J. Bao and X. Liu, High ambipolar mobility in cubic boron arsenide revealed by transient reflectivity microscopy, *Science*, 2022, **377**, 433–436.

290 S. Li, C. Su, Z. Qin, A. Alatas, M. Kunz, T. Yamada, S. D. Kelly, M. H. Upton, A. Gironda, J. Zhao, B. Kalkan, W. Yang, T. Aoki and Y. Hu, Metallic θ-phase tantalum nitride has a thermal conductivity triple that of copper, *Science*, 2026, **391**, 707–711.

291 A. Kundu, X. Yang, J. Ma, T. Feng, J. Carrete, X. Ruan, G. K. H. Madsen and W. Li, Ultrahigh Thermal Conductivity of theta-Phase Tantalum Nitride, *Phys. Rev. Lett.*, 2021, **126**, 115901.

292 B. Liao, A. A. Maznev, K. A. Nelson and G. Chen, Photo-excited charge carriers suppress sub-terahertz phonon mode in silicon at room temperature, *Nat. Commun.*, 2016, **7**, 13174.

293 J.-Y. Chen, J. Zhu, D. Zhang, D. M. Lattery, M. Li, J.-P. Wang and X. Wang, Time-Resolved Magneto-Optical Kerr Effect of Magnetic Thin Films for Ultrafast Thermal Characterization, *J. Phys. Chem. Lett.*, 2016, **7**, 2328–2332.

294 J. Kimling, A. Philippi-Kobs, J. Jacobsohn, H. P. Oepen and D. G. Cahill, Thermal conductance of interfaces with amorphous SiO_2 measured by time-resolved magneto-optic Kerr-effect thermometry, *Phys. Rev. B*, 2017, **95**, 184305.

295 J. Liu, G.-M. Choi and D. G. Cahill, Measurement of the anisotropic thermal conductivity of molybdenum disulfide by the time-resolved magneto-optic Kerr effect, *J. Appl. Phys.*, 2014, **116**, 233107.

296 C. A. Gadre, X. Yan, Q. Song, J. Li, L. Gu, H. Huyan, T. Aoki, S.-W. Lee, G. Chen, R. Wu and X. Pan, Nanoscale imaging of phonon dynamics by electron microscopy, *Nature*, 2022, **606**, 292–297.

297 N. Li, R. Shi, Y. Li, R. Qi, F. Liu, X. Zhang, Z. Liu, Y. Li, X. Guo, K. Liu, Y. Jiang, X.-Z. Li, J. Chen, L. Liu, E.-G. Wang and P. Gao, Phonon transition across an isotopic interface, *Nat. Commun.*, 2023, **14**, 2382.

298 H. Yang, Y. Zhou, G. Miao, J. Rusz, X. Yan, F. Guzman, X. Xu, X. Xu, T. Aoki, P. Zeiger, X. Zhu, W. Wang, J. Guo, R. Wu and X. Pan, Phonon modes and electron–phonon coupling at the FeSe/SrTiO3 interface, *Nature*, 2024, **635**, 332–336.

299 R. Qi, R. Shi, Y. Li, Y. Sun, M. Wu, N. Li, J. Du, K. Liu, C. Chen, J. Chen, F. Wang, D. Yu, E.-G. Wang and P. Gao, Measuring phonon dispersion at an interface, *Nature*, 2021, **599**, 399–403.

300 R. Egoavil, N. Gauquelin, G. T. Martinez, S. Van Aert, G. Van Tendeloo and J. Verbeeck, Atomic resolution mapping of phonon excitations in STEM-EELS experiments, *Ultramicroscopy*, 2014, **147**, 1–7.

301 M. Wu, R. Shi, R. Qi, Y. Li, J. Du and P. Gao, Four-dimensional electron energy-loss spectroscopy, *Ultramicroscopy*, 2023, **253**, 113818.

302 R. Qi, N. Li, J. Du, R. Shi, Y. Huang, X. Yang, L. Liu, Z. Xu, Q. Dai, D. Yu and P. Gao, Four-dimensional vibrational spectroscopy for nanoscale mapping of phonon dispersion in BN nanotubes, *Nat. Commun.*, 2021, **12**, 1179.

303 L. P. René de Cotret, J.-H. Pöhls, M. J. Stern, M. R. Otto, M. Sutton and B. J. Siwick, Time- and momentum-resolved phonon population dynamics with ultrafast electron diffuse scattering, *Phys. Rev. B*, 2019, **100**, 214115.

304 M. Trigo, J. Chen, V. H. Vishwanath, Y. M. Sheu, T. Graber, R. Henning and D. A. Reis, Imaging nonequilibrium atomic vibrations with x-ray diffuse scattering, *Phys. Rev. B: Condens. Matter Mater. Phys.*, 2010, **82**, 235205.

305 D. Zhu, A. Robert, T. Henighan, H. T. Lemke, M. Chollet, J. M. Glownia, D. A. Reis and M. Trigo, Phonon spectroscopy with sub-meV resolution by femtosecond x-ray diffuse scattering, *Phys. Rev. B: Condens. Matter Mater. Phys.*, 2015, **92**, 054303.

306 Z. Chen, X. Shen, N. Andrejevic, T. Liu, D. Luo, T. Nguyen, N. C. Drucker, M. E. Kozina, Q. Song, C. Hua, G. Chen, X. Wang, J. Kong and M. Li, Panoramic Mapping of Phonon Transport from Ultrafast Electron Diffraction and Scientific Machine Learning, *Adv. Mater.*, 2023, **35**, 2206997.

307 J. Tersoff, Modeling solid-state chemistry: Interatomic potentials for multicomponent systems, *Phys. Rev. B: Condens. Matter Mater. Phys.*, 1989, **39**, 5566–5568.

308 A. K. Rappe, C. J. Casewit, K. S. Colwell, W. A. Goddard and W. M. Skiff, UFF, a full periodic table force field for molecular mechanics and molecular dynamics simulations, *J. Am. Chem. Soc.*, 1992, **114**, 10024–10035.

309 J. P. Janet, C. Duan, T. Yang, A. Nandy and H. J. Kulik, A quantitative uncertainty metric controls error in neural network-driven chemical discovery, *Chem. Sci.*, 2019, **10**, 7913–7922.

310 Z. Fan, Y. Wang, P. Ying, K. Song, J. Wang, Y. Wang, Z. Zeng, K. Xu, E. Lindgren, J. M. Rahm, A. J. Gabourie, J. Liu, H. Dong, J. Wu, Y. Chen, Z. Zhong, J. Sun, P. Erhart, Y. Su and T. Ala-Nissila, GPUMD: A package for constructing accurate machine-learned potentials and performing highly efficient atomistic simulations, *J. Chem. Phys.*, 2022, **157**, 114801.

311 S. De, A. P. Bartók, G. Csányi and M. Ceriotti, Comparing molecules and solids across structural and alchemical space, *Phys. Chem. Chem. Phys.*, 2016, **18**, 13754–13769.

312 J. Finkbeiner, S. Tovey and C. Holm, Generating minimal training sets for machine learned potentials, *Phys. Rev. Lett.*, 2024, **132**, 167301.

313 A. P. Bartók, M. C. Payne, R. Kondor and G. Csányi, Gaussian approximation potentials: the accuracy of quantum mechanics, without the electrons, *Phys. Rev. Lett.*, 2010, **104**, 136403.

314 L. Zhang, J. Han, H. Wang, R. Car and W. E, Deep potential molecular dynamics: a scalable model with the accuracy of quantum mechanics, *Phys. Rev. Lett.*, 2018, **120**, 143001.

315 J. López-Zorrilla, X. M. Aretxabaleta, I. W. Yeu, I. Etxebarria, H. Manzano and N. Artrith, ænet-PyTorch: a GPU-supported implementation for machine learning atomic potentials training, *J. Chem. Phys.*, 2023, **158**, 164105.

316 H. Li, M. Zhou, J. Sebastian, J. Wu and M. Gu, Efficient force field and energy emulation through partition of permutationally equivalent atoms, *J. Chem. Phys.*, 2022, **156**, 184304.

317 J. S. Smith, O. Isayev and A. E. Roitberg, ANI-1: an extensible neural network potential with DFT accuracy at force field computational cost, *Chem. Sci.*, 2017, **8**, 3192–3203.

318 I. Batatia, S. Batzner, D. P. Kovács, A. Musaelian, G. N. C. Simm, R. Drautz, C. Ortner, B. Kozinsky and G. Csányi, The design space of E(3)-equivariant atom-centered interatomic potentials, *arXiv*, 2022, preprint, arXiv:2205.06643, DOI: 10.48550/arXiv.2205.06643.

 This journal is © the Owner Societies 2026

319 B. Deng, P. Zhong, K. Jun, J. Riebesell, K. Han, C. J. Bartel and G. Ceder, CHGNet as a pretrained universal neural network potential for charge-informed atomistic modelling, *Nat. Mach. Intell.*, 2023, **5**, 1031–1041.

320 J. Gasteiger, J. Groß and S. Günnemann, Directional message passing for molecular graphs, *arXiv*, 2022, preprint, arXiv:2003.03123, DOI: 10.48550/arXiv.2003.03123.

321 S. Chmiela, A. Tkatchenko, H. E. Sauceda, I. Poltavsky, K. T. Schütt and K.-R. Müller, Machine learning of accurate energy-conserving molecular force fields, *Sci. Adv.*, 2017, **3**, e1603015.

322 A. V. Shapeev, Moment tensor potentials: a class of systematically improvable interatomic potentials, *Multiscale Model. Simul.*, 2016, **14**, 1153–1173.

323 C. Chen and S. P. Ong, A universal graph deep learning interatomic potential for the periodic table, *Nat. Comput. Sci.*, 2022, **2**, 718–728.

324 M. Haghighatlari, J. Li, X. Guan, O. Zhang, A. Das, C. J. Stein, F. Heidar-Zadeh, M. Liu, M. Head-Gordon, L. Bertels, H. Hao, I. Leven and T. Head-Gordon, NewtonNet: a newtonian message passing network for deep learning of interatomic potentials and forces, *Digital Discovery*, 2022, **1**, 333–343.

325 S. Batzner, A. Musaelian, L. Sun, M. Geiger, J. P. Mailoa, M. Kornbluth, N. Molinari, T. E. Smidt and B. Kozinsky, E(3)-equivariant graph neural networks for data-efficient and accurate interatomic potentials, *Nat. Commun.*, 2022, **13**, 2453.

326 O. T. Unke and M. Meuwly, PhysNet: a neural network for predicting energies, forces, dipole moments, and partial charges, *J. Chem. Theory Comput.*, 2019, **15**, 3678–3693.

327 S. Chmiela, H. E. Sauceda, I. Poltavsky, K.-R. Müller and A. Tkatchenko, sGDML: constructing accurate and data efficient molecular force fields using machine learning, *Comput. Phys. Commun.*, 2019, **240**, 38–45.

328 J. Brandstetter, R. Hesselink, E. van der Pol, E. J. Bekkers and M. Welling, Geometric and physical quantities improve E(3) equivariant message passing, *arXiv*, 2022, preprint, arXiv: 2110.02905, DOI: 10.48550/arXiv.2110.02905.

329 A. P. Thompson, L. P. Swiler, C. R. Trott, S. M. Foiles and G. J. Tucker, Spectral neighbor analysis method for automated generation of quantum-accurate interatomic potentials, *J. Comput. Phys.*, 2015, **285**, 316–330.

330 K. T. Schütt, H. E. Sauceda, P.-J. Kindermans, A. Tkatchenko and K.-R. Müller, SchNet – a deep learning architecture for molecules and materials, *J. Chem. Phys.*, 2018, **148**, 241722.

331 S. Takamoto, S. Izumi and J. Li, TeaNet: universal neural network interatomic potential inspired by iterative electronic relaxations, *Comput. Mater. Sci.*, 2022, **207**, 111280.

332 Z. Fan, Z. Zeng, C. Zhang, Y. Wang, K. Song, H. Dong, Y. Chen and T. Ala-Nissila, Neuroevolution machine learning potentials: Combining high accuracy and low cost in atomistic simulations and application to heat transport, *Phys. Rev. B*, 2021, **104**, 104309.

333 D. F. Thomas du Toit, Y. Zhou and V. L. Deringer, Hyperparameter optimization for atomic cluster expansion potentials, *J. Chem. Theory Comput.*, 2024, **20**, 10103–10113.

334 D. F. Thomas Du Toit and V. L. Deringer, Cross-platform hyperparameter optimization for machine learning interatomic potentials, *J. Chem. Phys.*, 2023, **159**, 024803.

335 A. Rajabpour, B. Mortazavi, P. Mirchi, J. El Hajj, Y. Guo, X. Zhuang and S. Merabia, Accurate estimation of interfacial thermal conductance between silicon and diamond enabled by a machine learning interatomic potential, *Int. J. Therm. Sci.*, 2025, **214**, 109876.

336 W. Wang, X. Wu, Y. Wu, S. Volz, T. Takagi and M. Nomura, Interfacial thermal transport analysis using machine learning potential at AlN/Cu van der Waals interface, *Mater. Today Phys.*, 2026, **62**, 102057.

337 K. Wu and M. Liao, Mapping phonon dynamics to thermal transport *via* deep-learning NEMD: AlN/diamond interface engineering for GaN heat dissipation, *Funct. Diamond*, 2025, **5**, 2561987.

338 J. Yue, S. Hu, B. Xu, R. Chen, L. Xiong, R. Guo, Y. Li, L.-L. Nian, J. Shiomi and B. Zheng, Unraveling the mechanisms of thermal boundary conductance at the graphene-silicon interface: insights from ballistic, diffusive, and localized phonon transport regimes, *Phys. Rev. B*, 2024, **109**, 115302.

339 K. Z. Adnan, M. R. Neupane and T. Feng, Thermal boundary conductance of metal–diamond interfaces predicted by machine learning interatomic potentials, *Int. J. Heat Mass Transfer*, 2024, **235**, 126227.

340 Z. Huang, Q. Wang, X. Liu and X. Liu, First-principles based deep neural network force field for molecular dynamics simulation of N–Ga–Al semiconductors, *Phys. Chem. Chem. Phys.*, 2023, **25**, 2349–2358.

341 W. Luo, E. Yin, L. Wang, W. Lian, N. Wang and Q. Li, Heat transfer enhancement of N-Ga-Al semiconductors heterogeneous interfaces, *Int. J. Heat Mass Transfer*, 2025, **244**, 126902.

342 Z. Sun, X. Sun, Z. Qi, Q. Wang, R. Li, L. Li, G. Wu, W. Shen and S. Liu, Investigating thermal transport across the AlN/diamond interface *via* the machine learning potential, *Diamond Relat. Mater.*, 2024, **147**, 111303.

343 Z. Sun, D. Zhang, Z. Qi, Q. Wang, X. Sun, K. Liang, F. Dong, Y. Zhao, D. Zou, L. Li, G. Wu, W. Shen and S. Liu, Insight into interfacial heat transfer of β-Ga_2O_3 /diamond heterostructures *via* the machine learning potential, *ACS Appl. Mater. Interfaces*, 2024, **16**, 31666–31676.

344 Z. Sun, H. Shi, Y. Zhu, R. Li, X. Sun, Q. Wang, Z. Qi, L. Li, S. Liu, W. Shen and G. Wu, A comprehensive exploration of thermal transport at Cu/diamond interfaces *via* machine learning potentials, *npj Comput. Mater.*, 2025, **11**, 359.

345 B. Mortazavi, E. V. Podryabinkin, S. Roche, T. Rabczuk, X. Zhuang and A. V. Shapeev, Machine-learning interatomic potentials enable first-principles multiscale modeling of lattice thermal conductivity in graphene/borophene heterostructures, *Mater. Horiz.*, 2020, **7**, 2359–2367.

346 J. Wu, E. Zhou, A. Huang, H. Zhang, M. Hu and G. Qin, Deep-potential enabled multiscale simulation of gallium nitride devices on boron arsenide cooling substrates, *Nat. Commun.*, 2024, **15**, 2540.

347 Z. Sun, Z. Qi, Y. Song, L. Li, S. Liu, W. Shen and G. Wu, Multiscale investigation of thermal transport in β-Ga2O3-based heterointerfaces enabled by machine learning potential: cross-scale parameter, *npj Comput. Mater.*, 2026, **12**, 130.
348 Z. Li, X. Tan, Z. Fu, L. Liu and J.-Y. Yang, Thermal transport across copper–water interfaces according to deep potential molecular dynamics, *Phys. Chem. Chem. Phys.*, 2023, **25**, 6746–6756.
349 F. Liang, J. Ding, X. Wei, G. Pan and S. Liu, Interfacial heat and mass transfer at silica/binary molten salt interface from deep potential molecular dynamics, *Int. J. Heat Mass Transfer*, 2023, **217**, 124705.
350 N. Wang, J. Jieensi, Z. Zhen, Y. Zhou and S. Ju, *2022 23rd International Conference on Electronic Packaging Technology (ICEPT)*, 2022, pp. 1–4.
351 X. Tian and M. Chen, Descriptor selection for predicting interfacial thermal resistance by machine learning methods, *Sci. Rep.*, 2021, **11**, 739.
352 X. Song, W. Zheng, H. Ai, H. Zhou, L. Feng, Z. Cui and R. Guo, Key physical descriptors for predicting interfacial thermal resistance by machine learning, *J. Appl. Phys.*, 2025, **137**, 245302.
353 Y.-J. Wu, T. Zhan, Z. Hou, L. Fang and Y. Xu, Physical and chemical descriptors for predicting interfacial thermal resistance, *Sci. Data*, 2020, **7**, 36.
354 Y.-J. Wu, L. Fang and Y. Xu, Predicting interfacial thermal resistance by machine learning, *npj Comput. Mater.*, 2019, **5**, 56.
355 C. Foss and Z. Aksamija, Machine learning enables robust prediction of thermal boundary conductance of 2D substrate interfaces, *Appl. Phys. Lett.*, 2023, **122**, 62201.
356 M. Al-Fahdi and M. Hu, High throughput substrate screening for interfacial thermal management of β-Ga2O3 by deep convolutional neural network, *J. Appl. Phys.*, 2024, **135**, 205101.
357 Y.-J. Wu, M. Sasaki, M. Goto, L. Fang and Y. Xu, Electrically conductive thermally insulating Bi–Si nanocomposites by interface design for thermal management, *ACS Appl. Nano Mater.*, 2018, **1**, 3355–3363.
358 H. Yang, Z. Zhang, J. Zhang and X. Cheng Zeng, Machine learning and artificial neural network prediction of interfacial thermal resistance between graphene and hexagonal boron nitride, *Nanoscale*, 2018, **10**, 19092–19099.
359 S. Rustam, M. Schram, Z. Lu, A. M. Chaka, W. S. Rosenthal and J. Pfaendtner, Optimization of thermal conductance at interfaces using machine learning algorithms, *ACS Appl. Mater. Interfaces*, 2022, **14**, 32590–32597.
360 S. Jin, Z. Zhang, Y. Guo, J. Chen, M. Nomura and S. Volz, Optimization of interfacial thermal transport in Si/Ge heterostructure driven by machine learning, *Int. J. Heat Mass Transfer*, 2022, **182**, 122014.
361 Y. Guo, G. Li, T. Mabuchi, D. Surblys, T. Ohara and T. Tokumasu, Prediction of nanoscale thermal transport and adsorption of liquid containing surfactant at solid–liquid interface *via* deep learning, *J. Colloid Interface Sci.*, 2022, **613**, 587–596.

 This journal is © the Owner Societies 2026